Controlled absorption of heralded single photons by a single atom: Towards entanglement distribution in quantum networks

Nicolas Piro

Thesis supervisor: Prof. Jürgen Eschner

Doctoral Program in Applied Physics and Simulations in Science
Universitat Politècnica de Catalunya

Abstract

The interaction of single photons with single atoms is a fundamental process in quantum optics which manifests the quantum mechanical nature of light and matter. As an experimentally controlled process it enables the implementation of quantum technological applications, such as quantum information processing and quantum metrology. In the last decades, substantial progress has been attained to experimentally control and manipulate single atoms. For example, single or multiple ions can be stored in an ion trap and their quantum states can be controlled with great precision. At the same time, experimental techniques to generate and control single photons and entangled photon pairs have been widely developed. However, only modest progress has been attained in controlling the interaction of single atoms with single photons.

The aim of this thesis project was to experimentally study the absorption of single photons and pairs of entangled photons by single trapped $^{40}Ca^{+}$ ions. To this end, a source of polarization-entangled photon pairs based on the process of spontaneous parametric down-conversion (SPDC) was developed and constructed. Generating photon pairs whose interaction with an atom can be controlled imposed stringent requirements on the bandwidth, tunability, stability and brightness of the source, making its setup much more complex than usual SPDC sources. In a parallel project, a set of two separate ion traps were built, capable of storing a single or a set of a few $^{40}Ca^{+}$ ions.

The first part of the thesis documents the design, construction, operation and characterization of the entangled photon pair source. The characterization proves all the necessary requirements for the photons to interact with either of two transitions, $D_{3/2} \leftrightarrow P_{3/2}$ and $D_{5/2} \leftrightarrow P_{3/2}$ at 850 and 854 nm respectively, in $^{40}Ca^{+}$. One of the crucial requirements was to make the source bandwidth match the bandwidth of these transitions (22 MHz). This was not straightforward since the typical emission bandwidths of the SPDC process is several orders of magnitude higher (10^5 MHz). The ion trap setup is also briefly described. One of its crucial features is the inclusion of two high numerical-aperture objectives very close to the ion trap, allowing to enhance the interaction efficiency of the down-conversion photons with the ion, and to efficiently collect the fluorescence light they emit.

In a second part of the thesis, a concise description of the schemes and techniques used to detect the absorption of single photons by a single trapped ion is given. This includes a theoretical treatment of the methods used to analyze the data.

The core part of the thesis describes the methods used to couple the entangled photon source to one of the ion traps, and explains the results obtained with the combined setup. First it shows how the source is configured to produce heralded single photons. It then presents experiments in which the absorption by a single ion

of photons produced by the source is detected, and how these absorption events are time-correlated with the detection of the heralding photon. These experiments are performed under several conditions, with a growing level of control over the interaction process. Finally, two proof-of-principle experiments are presented. In the first one, the ion is pumped to polarization-sensitive Zeeman substates and the polarization dependence of the correlated absorption rate is observed. This is a first step toward more advanced experiments in which the polarization entanglement of the photon pairs is transferred to the entanglement of one photon with one atom or to two distant atoms. A second experiment performs heralded single photon spectroscopy on a single ion, showing the expected frequency dependence of the absorption process.

Finally, methods to extend these experiments to implement entanglement transfer from photons to atoms are outlined. In particular, it is shown how the efficiency of the source can be improved to make these experiments feasible.

Resumen

La interacción de fotones individuales con átomos individuales es un proceso fundamental de la óptica cuántica que pone de manifiesto la naturaleza mecano-cuántica de la luz y materia. Controlado experimentalmente, este proceso permite la implementación de aplicaciones de tecnologías cuánticas tales como el procesado de información cuántica y metrología cuántica. En las últimas déecadas, ha tenido lugar un progreso sustancial en el control y manipulación experimental de átomos individuales. Por ejemplo, se ha conseguido almacenar uno o varios átomos en una trampa de iones y controlar sus estados cuánticos con gran precisión. Asimismo, se han desarrollado ampliamente las técnicas experimentales para generar y controlar fotones individuales y pares de fotones entrelazados. Por el contrario, sin embargo, el progreso de las técnicas para controlar la interacción de dichos fotones individuales con tales átomos individuales ha sido solo modesto.

El objetivo de esta tesis ha sido el estudio experimental de la absorción de fotones individuales y pares de fotones entrelazados por parte de iones de $^{40}Ca^{+}$ individuales atrapados. Con este fin, desarrollamos y construimos una fuente de pares de fotones entrelazados en polarización basada en el proceso de *spontaneous parametric down-conversion* (SPDC). La generación de pares de fotones con las propiedades adecuadas para hacer posible el control de su interacción con átomos individuales impuso requerimientos estrictos sobre las especificaciones de la fuente en cuanto a su ancho de banda, su sintonizabilidad, su estabilidad y su luminosidad, lo que implica que el montaje experimental haya sido sustancialmente más complejo que el de fuentes típicas de SPDC. En un proyecto paralelo se construyeron dos trampas de iones separadas, con capacided de atrapar un ion individual de $^{40}Ca^{+}$ o un pequeño grupo de estos.

La primera parte de esta tesis documenta el diseño, construcción, operación y caracterización de la fuente de pares de fotones entrelazados. La caracterización demuestra que todos los requisitos necesarios para que los fotones sean capaces de interaccionar con el $^{40}Ca^{+}$ a través de dos transiciones, la $D_{3/2} \leftrightarrow P_{3/2}$ a 850 nm y la $D_{5/2} \leftrightarrow P_{3/2}$ a 854 nm, se cumplen. Uno de los requisitos imprescindibles era que el ancho de banda de la fuente coincidiera con el ancho de banda de la transición atómica (22 MHz). Satisfacer esta condición no fue trivial, ya que el ancho de banda típico de emisión en el proceso de SPDC es varios órdenes de magnitud superior (10^5 MHz), de modo que la estrategia adoptada se describe con detalle en esta parte de la tesis. También se da una breve descripción del dispositivo experimental de la trampa de iones. Una de las características cruciales de este dispositivo es la inclusión de dos objetivos de alta apertura numérica muy cerca de la trampa de iones, la cual permitió optimizar la eficiencia de interacción de los fotones con el ion y la eficiencia de recolección de fotones de fluorescencia emitidos por el átomo.

En la segunda parte de la tesis se da una descripción concisa de los esquemas y técnicas usadas para detectar la absorción de fotones individuales por un átomo individual atrapado. Esto incluye un tratamiento teórico de los métodos usados para analizar los datos experimentales.

El núcleo de la tesis describe los métodos usados para acoplar la fuente a una de las trampas de iones y explica los resultados obtenidos con la combinación de ambos dispositivos. Primero se muestra cómo se configuró la fuente para producir fotones individuales anunciados (*heralded single photons*). En esta configuración, la detección de uno de los fotones de cada par augura la presencia del fotón hermano. A continuación se presentan experimentos en los que se detecta la absorción, por parte de un ion individual atrapado, de uno de los fotones de los pares producidos con la fuente, y la correlación temporal de estos eventos con la detección del fotón gemelo. Estos experimentos se realizaron en distintas condiciones, con un creciente grado de control sobre el proceso de interacción. Finalmente, se presentan dos experimentos de constatación. En el primero, el estado inicial del átomo se prepara, mediante bombeo óptico, en estados Zeeman de $D_{5/2}$ sensibles a la polarización, y se mide la dependencia del proceso de absorción de fotones individuales con la polarización del fotón incidente. En un segundo experimento se realiza espectroscopía con fotones individuales sobre un átomo individual atrapado, mostrando la dependencia esperada del proceso de absorción con la frecuencia de los fotones incidentes.

Finalmente se presentan métodos para extender estos experimentos e implementar esquemas en los que se transfiere el entrelazamiento en polarización de los pares de fotones a un entrelazamiento entre estados internos de átomos individuales atrapados. En particular, se sugiere cómo se puede mejorar la eficiencia de la fuente para hacer estos experimentos viables.

Acknowledgements

Here I'd like to thank all the people who helped me in some way to conclude this thesis by either directly contributing to the work, supporting me or just being there in the good and bad moments during this long process.

First of all, I'd like to thank Jürgen Eschner for giving me the opportunity to work in such a fascinating and challenging project. I especially appreciate your great physical background and the intuitive explainations of the physics and engineering involved.

I'd also like to thank Albrecht Haase, for getting me started into the world of experimental quantum optics, and for sharing with me nice moments (in and out of the lab) during the entertaining phase of building the experiment and taking the first measurements.

I thank all the members of the ion trapping experiment. In particular, I thank Marc Almendros for being a nice office and lab companion, for teaching me a lot of engineering and for forming part with me of the small non-German subteam in the group. I also thank Felix Rohde, Carsten Schuck, Markus Hennrich and also Marc for their great effort in starting up the ion trap experiment, for our joint measurements in the first ion-photon interaction experiments and for the nice moments we had together.

Thanks to Jan Huwer and Joyee Ghosh, who jumped into the project later on, for bringing some fresh air, and for the nice moments we had in the lab together (e.g. making the process of counting quantum jumps a bit less boring!) The same goes to Francois Dubin, from whom I learned a lot and who supported me in uncountable ways.

Finally, I'd like to thank the other members of the group not involved in this experiment, Matteo, Tristan and Hannes, with whom we shared the lab, had useful discussions and great moments for four years.

I wouldn't like to forget the big effort provided by the teams in the electronic and mechanical workshops. I especially thank Jose Carlos for helping us develop all those cavity lockers and the rest of electronics.

Special thanks to Gabriel Molina for all the useful discussions on parametric down-conversion and the few weeks of intense lab work we shared, not to forget the great moments in the karaoke! Thanks to many other friends with whom I had the pleasure to share great moments during these four years.

And finally, special thanks to my parents for supporting me and always being there during these difficult years. Thanks dad for transmitting me your passion for physics!

Contents

1. Introduction

This thesis studies the interaction of light and matter at the fundamental limit of single particles. In such a regime, a quantum mechanical description of light is necessary, and the field of *quantum optics* emerges. Research in quantum optics is partly aimed at exploring the foundations of quantum mechanics, allowing to study striking features which do not appear in classical physics. In addition, the experimental control of these quantum phenomena can serve as useful tools for quantum technologies, in particular *quantum information processing* by which certain computation and communication tasks can be performed in a more efficient and more secure way than with classical systems.

This chapter offers a brief historical introduction to these fields, putting special emphasis on the techniques used to perform the experiments documented in this manuscript, namely ion trapping and generation of entangled photon pairs. This will allow us to introduce our experiment and the motivation behind it. This chapter also serves as a compendium of references to the most important works of the field.

1.1. Quantum optics

The nature of light has historically been a matter of dispute in the scientific community. The controversial question was whether light is formed by particles or waves. The debate dates back to the seventeenth century and was led by two scientific figures of those days. Huygens suggested a wave theory for light with which he could explain phenomena such as interference and diffraction. This theory was soon overshadowed by Isaac Newton's corpuscular description. The wave-like description was recovered as soon as Maxwell formulated his successful theory of electromagnetism, and was highly consolidated at the end of the nineteenth century.

The situation changed dramatically when Max Planck postulated the existence of light quanta (photons) to successfully model the measured spectrum of blackbody radiation. It was then when the field of quantum optics was born. Soon after, Bohr postulated the quantization of the atomic transition energies, and Einstein explained the photo-electric effect also making use of the concept of photons.

The theory of quantum optics was thoroughly developed by George Sudarshan, Roy J. Glauber, and Leonard Mandel in the 1960s. They applied quantum mechanics to the electromagnetic field and its interaction with atoms to describe the photodetection process and statistical properties of detected photons [1, 2, 3]. The properties and types of quantum states of light were investigated introducing several concepts. The coherent state was defined and shown to be a good approxima-

tion for the statistics of light emitted by a laser far above threshold. States of light with non-classical statistics were introduced, such as the single photon state, the squeezed state, photon bunching and antibunching, and sub-poissonian photon statistics.

In 1956 Hanbury, Brown and Twiss observed for the first time the bunching effect between two photons from a thermal source. They performed an experiment in which two photomultiplier tubes placed around 6 meters apart were aimed at a distant star and the correlation between the photo-detections in the two detectors were studied. The results revealed a constructive interference for short time delays (bunching) even though there was no phase relation in the light between the two detectors. The techniques used in this experiment to measure the intensity correlation function are nowadays used extensively in experimental quantum optics.

Fast progress in quantum optics was triggered by the invention of the laser in the late sixties. This allowed the realization of several milestone experiments. The first source of antibunched photons, emitted in resonance fluorescence of atoms, was implemented by Kimble et al. in 1977 [4]. Laser cooling of trapped atoms was first shown by Wineland et al. [5] and Neuhauser et al [6] in 1978. Aspect and coworkers produced the first source of entangled photon pairs by radiative cascade of a single atom [7]. Later on, they used a similar setup as a heralded single photon source to show the anticorrelation effect on a beam-splitter and single photon interference [8].

The high intensity available in laser sources also enabled the development of nonlinear optics. This had a strong impact in quantum optics, as it allowed to discover the process of spontaneous parametric down-conversion (SPDC), which is nowadays widely used in many quantum optics experiments. The effect, initially termed parametric luminescence, was predicted theoretically by Klyshko in 1966 [9] and was observed shortly thereafter [10].

The time correlations between the emitted photon pairs in an SPDC source was observed a few years later [11], marking the starting point for the production of quantum states of light with SPDC. For example, the process was used to generate the first source of heralded single photons by Hong et al. in 1986 [12]. An individual photon beam cannot be considered to have non-classical statistics. However, the detection of one photon predicts the presence of its partner, so adding a gating mechanism on one beam conditioned on the detection of the photon in the second beam produces a source with sub-Poissonian and anti-bunched statistics. An SPDC source was also used by Hong et al. to study the interference of two identical photons impinging onto the two ports of a 50:50 beam-splitter, showing that both photons always emerge from the same output port [13]. This photon coalescence effect is nowadays well known as Hong-Ou-Mandel interference. Polarization entanglement in SPDC sources was soon observed by several experiments [14, 15, 16, 17].

Another technique that revolutionized experiments in quantum optics is ion trapping. The Penning trap, developed by Hans Dehmelt in 1953, uses static magnetic and electric fields to trap the charged particle. In the same year, Wolfgang Paul developed a trap that uses only static and oscillating electric fields. The first type is widely used in high precision spectroscopy and mass spectrometry. The latter type

is widely used in the quantum optics and quantum information community and in particular in our experiment.

The ability to trap and laser cool single ions allowed to perform several outstanding quantum optics experiments. The striking observation of a single ion undergoing quantum jumps, was performed in 1986 separately by Dehmelt et al, Sauter et al. and Bergquist et al. [18, 19, 20]. One year later, Diedrich and co-workers studied the non-classical statistics (anti-bunching, sub-poissonian) of resonance fluorescence photons emitted by a single trapped ion [21]. Soon after, laser cooling to the motional ground state was achieved [22]. This enabled the possibility of implementing quantum logic gates and therefore opened the way towards quantum information processing with single trapped ions.

The experiments presented so far were mostly motivated by fundamental issues regarding the quantum mechanical nature of the processes involved. But in the last decades, the control over the experimental systems has reached a level that enables their application for quantum information processing purposes.

1.2. Quantum information

Quantum information science is essentially divided in two categories: quantum computation and quantum communication. Quantum computation is based on the idea of exploiting the features of quantum mechanics for performing computation in a more efficient way than with classical systems. Quantum communication tries to exploit these features to perform secure and maybe more efficient communication.

The basic principle of quantum computation is the parallelism provided by the superposition principle. In a classical computer, the basic unit of information, the *bit*, can be in either of two states, 0 or 1. In a quantum computer, this unit is formed by the *qubit*, which can be in either the 0 or 1 states, but also in a superposition. In general, n qubits can be in a superposition of 2^n states, meaning that 2^n complex numbers are necessary to represent the state of the system. Conversely, in a classical computer n bits are represented by just n values. By performing a single operation on the set of n qubits the whole set of 2^n complex numbers evolve, while a classical computer operation only modifies n different numbers. This is the essence of the exponential increase in computation efficiency of quantum computers with respect to classical ones.

Still, effective algorithms to perform useful tasks exploiting this principle must be conceived. The first such algorithm was devised in 1992 by Deutsch and Jozsa. Their routine can be used to determine if a binary function of n bits is constant or balanced (for example, if a set of coins have their faces equal or different) in an exponentially faster time than with any classical algorithm [23]. Soon after, Peter Shor proposed a quantum algorithm to factor prime number requiring a number of steps which increases polynomially with the size of the input [24], as opposed to any known classical algorithm which takes an exponentially growing time to perform the task. Since the most widely used public-key cryptographic scheme,

known as RSA [25], relies on the factorization of large numbers, a quantum computer would highly threaten its security. Shor's algorithm was first realized experimentally in 2001 using a nuclear magnetic resonance (NMR) implementation of a quantum computer with 7 qubits to factor the number 15 [26]. Despite this, it would only become of practical use if the number of qubits is scaled up by one or two orders of magnitude. The Deutsch-Jozsa algorithm was first realized also with a NMR system [27] and later in an ion trap quantum computer [28].

Quantum computers can in principle be implemented with different physical systems. It is well established that for a given system to be adequate, the so-called Di-Vincenzo criteria must be fulfilled [29]. Namely, one needs

- 1) a scalable physical system with well characterized qubits,
- 2) the ability to initialize the state of the qubits to a simple fiducial state, such as $|000...\rangle$,
- 3) long relevant decoherence times, much longer than the gate operation time,
- 4) a "universal" set of quantum gates,
- 5) a qubit-specific measurement capability.

A choice must be made on how to encode the qubit in an effective two-level system such that it can be controlled and kept free of decoherence. At present, research is focusing on very diverse types of systems. Some of them are 1) *Nuclear magnetic resonance* for which the qubit is encoded in the nuclear spin of an ensemble of atoms. 2) *Superconducting systems* in which the qubits are encoded in the charge, flux or phase of some superconducting device, 3) linear optics quantum computation, for which the qubits are encoded in one of the degrees of freedom of photons, such as polarization or the presence or absence of a photon in certain mode. 4) trapped neutral atoms or ions, with qubits encoded in two of the internal electronic levels of the atom.

It is worth mentioning that trapped ions are particularly suited for quantum computation, since in general criteria 1-5 have been proven, perhaps with the problem of limited scalability. A short list of examples of experimental achievements in this respect include the implementation of the Deutsch-Jozsa algorithm [28], implementation of the C-NOT gate [30], entangling up to eight ions in a single trap [31] and entangling two trapped ions at a distance of about 1 m [32].

In order to introduce quantum communication capabilities into the system, Di-Vincenzo adds two extra requirements:

- 6) the ability to interconvert stationary and flying qubits,
- 7) the ability to faithfully transmit flying qubits between specified locations

Note that quantum computation itself might need quantum communication capabilities. For example, one might think of a quantum network, composed of distributed quantum computational nodes connected by quantum communication channels. We will assume, hereafter, that the nodes of the network are composed of ion traps, capable of storing several ions, and the quantum channels are implemented by photons traveling through single-mode optical fibers. Such networks represent a possible strategy to solve the problem of scalability of an ion trap based quantum computer, distributing the computation in several distant nodes (another

strategy, which is receiving much attention lately, is the implementation of segmented microtraps capable of storing and controlling several thousands of ions). In order for such a quantum network to be feasible, criteria 6 and 7 have to be fulfilled.

1.3. Motivation

The motivation of this thesis is two-fold: as an experimental study of fundamental physics and as an experiment with applications in quantum information processing.

As a fundamental quantum optics experiment, studying the interaction of single photons with single atoms may give insight on the degree of control that can be achieved in the process. In this respect, current research in other groups is dedicated to studying how efficiently a laser beam can interact with a single atom by strongly focusing it with a high numerical aperture lens [33], and how to shape the optical mode and temporal shape of the impinging photons to achieve close to unity absorption efficiency [34, 35].

Our studies are also motivated by their applications in quantum information processing. In particular, we study the experimental implementations of quantum networks. The principle components of our network are two separate ion traps. Guided by the DiVincenzo criteria 6 and 7, we aim at controlling the transfer of qubits from one trap to the other. One strategy for this would be to map an atomic qubit in one trap into a photonic qubit, send the photon to the second trap in an efficient way, and map the photonic qubit back to an atomic qubit of the second trap [36]. However, the efficiency of this scheme would be extremely low in our case. A better strategy would be to establish entanglement between two atoms, each stored in a separate ion trap, and perform quantum teleportation of the state of a third ion in one trap to the state of the ion in the second trap. A crucial step for this is to entangle two distant atomic qubits. The first experimental realization of this has been achieved in 2007 [32], following the proposal of Simon et al., which makes use of the quantum interference of two photons emitted by the two ions and of the entanglement between each atom and the photon they emit [37]. Another scheme, which is on the line of the work of this thesis, is to prepare entangled photon pairs by an SPDC source and map the state of each photon into a pair to two distant trapped ions [38]. This technique will be presented in Chapter 8.

Our experiment also represents the unification of two different extensively developed research fields. On one side, ion trapping provides the best control over atomic quantum systems to store and manipulate stationary qubits. On the other side, SPDC based photon sources are corrently the best known way to generate entanglement and travelling quantum states.

From the technological side, one extra motivation that makes these experiments attractive is the technical difficulty they imply, and in particular the requirement of mixing techniques from several fields: ion trapping, laser cooling and generation of entangled photon pairs or heralded single photons by the process of SPDC.

Such highly demanding techniques require developing state-of-the-art equipment which represent significant contributions to the technology available in the field. One example is the pulse sequencer device (Hydra) developed by another PhD student in the group [39]. This device provides programmable sequences of parallel radio-frequency pulses with nanosecond time resolution, to drive the accousto-optic modulators driving the different lasers to excite the ion.

1.4. The experiment

Our generic experimental setup is intended to implement the basic building blocks of a quantum network. It consists of two separate ion traps, placed at a distance of about 1 meter, capable of trapping single or a string of a few $^{40}Ca^{+}$ ions. The system is equipped with a set of stabilized and tunable laser systems to address the different atomic transitions. There are several reasons for choosing this ion and not others, including the availability of laser sources at the necessary wavelengths, the simplicity of its level structure and, what's important for the goal of this thesis, the availability of allowed transitions, namely $D_{3/2} \leftrightarrow P_{3/2}$ and $D_{5/2} \leftrightarrow P_{3/2}$, at wavelengths for which the generation of entangled photon pairs with SPDC is feasible.

As a complementary tool to the set of ion traps, we built a source of entangled photon pairs with the necessary features to be able to interact efficiently with the mentioned transitions in $^{40}Ca^{+}$, namely frequency stability, tunability and narrow bandwidth of the photon pairs. These features are usually not available in standard SPDC sources and hence required significant technical development.

This thesis documents the construction and characterization of the entangled photon pairs source, the techniques used to couple it to the ion trap setup and the experiments performed with the combined setup. Regarding the characterization of the source, we study the different requirements necessary for its interaction with single $^{40}Ca^{+}$ ions, such as bandwidth, tunability, brightness and polarization entanglement. A second part of the thesis is dedicated to describing the experimental and data analysis techniques used to detect the absorption of a single photon by a single trapped ion. The final part describes the main result of the project, namely the observation of time correlations between the absorption of a single photon from the source and the detection of the partner photon on a single photon detector. This can be interpreted as the observation of absorption of heralded single photons by a single trapped ion. The experiment was first performed in a continuous scheme, and later on under a more controlled pulsed sequence. Some interesting proof of principle experiments were performed. The ion was initialized in a state which was sensitive to the polarization of the excited photon, and the dependence of the correlations with the polarization of the photons was studied. In a second experiment, correlated absorption spectroscopy on the addressed transition was performed with the source of heralded single photons. The results of these experiments are partly published in references [40, 41, 42, 43].

The ion trap system is quite flexible and allowed to perform several additional quantum optics experiments, in which I participated, but are not documented in

this thesis (just as other team members participated in the experiments I describe, while not documenting them in their thesis reports). In a first experiment, the two ion traps were used as two independent bandwidth-tunable single-photon sources and two-photon-interference on a 50:50 beam-splitter was observed, from which we could derive the coherence properties of the photons. In a second experiment, the polarization correlations between successive fluorescence photons emitted by a single ion were experimentally studied and modeled. For detailed descriptions of these experiments, see the relevant publications [44, 45], and the PhD theses by Marc Almendros [39] and Felix Rohde [46].

2. The entangled photon pair source: theoretical considerations

2.1. Theory of spontaneous parametric down-conversion

In this section we first give a brief introduction to nonlinear optics and to the process of spontaneous parametric down-conversion, used in the source to produce entangled photon pairs. We will then derive an expression for the quantum state of the bi-photon produced in our experimental setup, considering the process of type-II degenerate collinear spontaneous parametric down-conversion (SPDC) with each arm coupled to a single-mode fiber and a narrow bandwidth filter placed in one arm.

2.1.1. Introduction

Spontaneous parametric down-conversion is a nonlinear optical process in which a photon from a beam incident on a nonlinear crystal, called the pump, is split into two outgoing photons, termed signal and idler. In very general terms, if the process is time independent it must conserve the energy and thus

$$\omega_p = \omega_s + \omega_i, \tag{2.1.1}$$

where $\omega_{p,s,i}$ are the frequencies of the pump, signal and idler, respectively. Additionally, if the process is position invariant, i.e. the interaction region or the crystal extends all space, then the momentum must also be conserved. In practice, the nonlinear crystal has a length L, and the process is not completely position invariant, so a small momentum mismatch $\mathbf{\Delta k} \propto (1/L)\,\mathbf{e}_z$ in the propagation direction is allowed:

$$\mathbf{k}_p = \mathbf{k}_s + \mathbf{k}_i + \mathbf{\Delta k}. \tag{2.1.2}$$

Equations 2.1.1 and 2.1.2 are the so-called phase-matching conditions.

The optical response of a material is described in terms of the relation $P_i(E_j)$ between the induced polarization (the total dipole moment per unit volume) and the applied electric field. In general, this dependence is nonlinear and admits an expansion of the form [47]

$$P_i = \chi^{(1)}_{i,j} E_j + \chi^{(2)}_{i,j,k} E_j E_k + \chi^{(3)}_{i,j,k,l} E_j E_k E_l + ... \tag{2.1.3}$$

where $\chi^{(n)}$ is the nonlinear susceptibility of order n. The linear susceptibility tensor $\chi^{(1)}$ describes linear optical processes such as refraction and dispersion. The second order susceptibility tensor $\chi^{(2)}$ describes three photon nonlinear interactions, such

as sum frequency generation, difference frequency generation, parametric amplification and in particular spontaneous parametric down-conversion. In the following we will neglect higher order terms.

The origin of the term *parametric* seems to come from the jargon of dynamical systems. If $E_j = E_P$ is the pump field, the product $\chi^{(2)}_{i,j,k} E_j$ can be regarded as an oscillating first order susceptibility. From this perspective, second order nonlinear processes can be regarded as a linear optical interaction of a field with a material which has an oscillating susceptibility. In this sense, the system is driven by the oscillation of one of its parameters, and the corresponding process is termed *parametric*. In general, the oscillation of a parameter in a physical system can induce amplification of the dynamics at a different frequency. Well known examples are a child on a swing, where the periodic change in the center of mass of the child causes the swing to oscillate at half the driving frequency, the ripples which develop in the surface of a liquid tank when the latter is shaken vertically, thus varying the effective gravity, or the oscillation of a string when its tension is varied periodically. The processes of parametric amplification, parametric oscillation and spontaneous parametric down-conversion are examples in optics. In itself, SPDC can be regarded as the parametric amplification of the vacuum field induced by the pump field. Since one of the input field is vacuum, it requires a quantum mechanical treatment.

In our experiment, the crystal with the $\chi^{(2)}$ nonlinearity is $KTiOPO_4$ (KTP). KTP obeys full permutation symmetry, which implies that $\chi^{(2)}_{i,j,k}$ does not vary under the permutation of any of its indices if the frequencies of the corresponding fields are permuted accordingly [47]. In particular, indices j, k are symmetric and an alternative notation is used to reduce the number of independent components, defining $d_{i,l} = \chi^{(2)}_{i,j,k}/2$ with $l = 1, ..., 6$ for $ij = 11, 22, 33, 23(32), 13(31), 12(21)$. In addition, the spatial symmetries of the crystal structure of KTP imply that the only non zero components are ijk = 131, 113, 223, 232, 311, 322 and 333[1]. The non-vanishing nonlinear coefficients of KTP are $d_{31} = 2.4, d_{32} = 4.4, d_{33} = 16.9, d_{15} = 6.1, d_{24} = 7.6$ pm/V. We want to generate photon pairs of orthogonal polarization, so only coefficient d_{i4}, d_{i5}, d_{i6} can be used. The strongest of these is d_{24} so the crystal must be configured such that the pump is polarized along the axis 2, and signal and idler along axes 2 and 3. Hence, the propagation direction is the crystal axis 1. If the phase matching conditions are achieved for this configuration, the rest of possible processes will not be phase-matched, so they can be neglected.

2.1.2. Photon pair state calculation

To calculate the quantum state of the photon pairs generated with our configuration, we use time dependent perturbation theory. To first order in the perturbation,

[1] KTP has an mm2 orthorhombic crystal structure in space group $Pna2_1$. It has two mirror planes, a 1-fold and a 2-fold symmetry axis.

the output state in the interaction picture is

$$|\Psi\rangle = |0\rangle + \frac{i}{\hbar}\int_{-\infty}^{\infty} dt \hat{H}_{int}(t)\,|0\rangle\,. \tag{2.1.4}$$

The interaction hamiltonian $\hat{H}_{int}(t)$ for SPDC is obtained by quantizing Maxwell equations in a nonlinear dielectric medium using an expansion for the induced polarization in terms of the electric field as in expression 2.1.3 [48, 49]. In our experimental conditions (type-II collinear quasi-phasematching configuration with the pump, signal and idler fields polarized along the 2, 2, 3 crystallographic axes ($x \equiv 2$, $y \equiv 3$), $z \equiv 1$ being the propagation axis) it can be written

$$\hat{H}_{int}(t) = \int_V d^3\mathbf{r} d_{24}(\mathbf{r}) \hat{E}_p^\dagger(\mathbf{r},t)\hat{E}_s^\dagger(\mathbf{r},t)\hat{E}_i(\mathbf{r},t) + \text{h.c.} \tag{2.1.5}$$

$\hat{E}_{p,s,i}$ are the electric field operators for the pump, signal and idler and V is the interaction region, taken to be the crystal volume. In our setup the crystal domains are periodically flipped to enhance the interaction process, a technique known as periodic poling. The nonlinear coefficient $d_{24}(\mathbf{r})$ is then taken to be position dependent. For an ideal poling in which the nonlinearity is reversed periodically with a period Λ, $d_{24}(\mathbf{r}) = d_{\text{eff}}\text{sign}[\sin(2\pi z/\Lambda)]$ can be expanded in a Fourier series:

$$\begin{aligned} d_{24}(\mathbf{r}) &= \sum_{n=-\infty}^{\infty} \frac{2d_{\text{eff}}}{\pi(2n+1)}\left[\exp\left(i\frac{2(2n+1)\pi z}{\Lambda}\right)\right] \\ &= \frac{2d_{\text{eff}}}{\pi}\left[\exp\left(i\frac{2\pi z}{\Lambda}\right) - \exp\left(-i\frac{2\pi z}{\Lambda}\right)\right] + \mathcal{O}(\exp(2\pi z/\Lambda)^3), \end{aligned} \tag{2.1.6}$$

where in the second line we have neglected higher harmonic terms.

The powerful pump electric field $\hat{\mathbf{E}}_\mathbf{p}$ can be taken to be a classical complex function and its depletion can be neglected if the interaction length is sufficiently small. Signal and idler fields $\hat{\mathbf{E}}_{\mathbf{s,i}}$ must be quantized. It is convenient to expand all the fields in a superposition of three dimensional plane waves, setting $\mathbf{k} = (k_x, k_y, k_z)$ and $\mathbf{q} = (k_x, k_y)$. It is also advantageous to perform a change of variable $k_z \to \omega$ in the propagation direction, such that

$$\mathbf{q} + k_z^2 = |\mathbf{k}|^2 \Rightarrow k_z(\mathbf{q},\omega) = \pm\sqrt{\left(\frac{\omega n(\omega)}{c}\right)^2 - \mathbf{q}^2}. \tag{2.1.7}$$

With these prescriptions, the pump field reads

$$\mathbf{E}_P(\mathbf{r},t) = \int \frac{d^2\mathbf{q}d\omega}{\sqrt{(2\pi)^3}}\tilde{\mathbf{E}}_P(\mathbf{q})e^{i[k_z(\mathbf{q},\omega)z + \mathbf{q}\cdot\mathbf{s} - \omega t]}. \tag{2.1.8}$$

Here, $\mathbf{q} = (k_x, k_y)$ is the transverse wavevector and $\mathbf{s} = (x, y)$. Similarly, the quantized signal and idler fields are written

$$\hat{\mathbf{E}}_{s,i} = \int \frac{d^2\mathbf{q}d\omega}{\sqrt{(2\pi)^3}}\sqrt{\frac{\hbar\omega}{2\epsilon_0 n_{s,i}(\mathbf{q},\omega)c}}e^{i[k_z(\mathbf{q},\omega)z + \mathbf{q}\cdot\mathbf{s} - \omega t]}\hat{a}_{s,i}(\mathbf{q},\omega). \tag{2.1.9}$$

The signal and idler photon creation and annihilation operators satisfy the commutation relations of the form

$$[\hat{a}_m(\mathbf{q}_m,\omega_m),\hat{a}_n^\dagger(\mathbf{q}_n',\omega_n')] = \delta(\mathbf{q}_m-\mathbf{q}_n')\delta(\omega_m-\omega_n')\delta_{m,n} \tag{2.1.10}$$
$$\tag{2.1.11}$$

Substituting 2.1.5, 2.1.6, 2.1.8 and 2.1.9 in 2.1.4 we have

$$\begin{aligned}\left|\Psi'\right\rangle &= |0\rangle + \frac{i}{(\sqrt{2\pi})^9\hbar}\int_{-\infty}^{\infty}dtdxdy\int_{-L/2}^{L/2}dz\int d^2\mathbf{q}_s d^2\mathbf{q}_i\int d\omega_s\int d\omega_i \\ &\quad\times\sqrt{\frac{\hbar^2\omega_s\omega_i}{4\epsilon_0^2 n(\mathbf{q}_s,\omega_s)n(\mathbf{q}_i,\omega_i)c^2}}\tilde{E}_p(\mathbf{q}_p) \\ &\quad\times e^{i\left(k_{z,s}+k_{z,i}-k_{z,p}+\frac{2\pi}{\Lambda}\right)z}e^{i(\mathbf{q}_s+\mathbf{q}_i-\mathbf{q}_p)\cdot\mathbf{s}}e^{i(\omega_s+\omega_i-\omega_p)t}\hat{a}_s^\dagger(\mathbf{q}_s,\omega_s)\hat{a}_i^\dagger(\mathbf{q}_i,\omega_i)\,|0,0\rangle \\ &= |0\rangle + \int d^2\mathbf{q}_s d^2\mathbf{q}_i d\omega_s d\omega_i\phi(\mathbf{q}_s,\mathbf{q}_i,\omega_s,\omega_i)\hat{a}_s^\dagger(\mathbf{q}_s,\omega_s)\hat{a}_i^\dagger(\mathbf{q}_i,\omega_i)\,|0,0\rangle\,. \end{aligned}\tag{2.1.12}$$

Note that the volume integral has been extended over the crystal length in the propagation direction z and over all space in the transverse directions x and y, which is valid if the transverse size of the pump beam is significantly smaller than the crystal width. We have also assumed that the dependence on frequency of the square-root term can be neglected in the down-conversion bandwidth and takes a constant value evaluated at the central down-conversion frequency. The expression

$$\phi(\mathbf{q}_s,\mathbf{q}_i,\omega_s,\omega_i) = CL\tilde{E}_p(\mathbf{q}_s+\mathbf{q}_i)\mathrm{sinc}\left(\frac{\Delta kL}{2}\right)\delta(\omega_s+\omega_i-\omega_p) \tag{2.1.13}$$

is called the mode function and completely describes the biphoton state. It is interpreted as the probability amplitude for signal and idler photon emission with frequencies ω_s and ω_i in the directions given by $\mathbf{q}_s$ and $\mathbf{q}_i$. The constant C is given by

$$C = i\sqrt{\frac{2\omega_{s,0}\omega_{i,0}}{\pi^3\epsilon_0^2c^2n_s(\omega_{s,0})n_i(\omega_{i,0})}}. \tag{2.1.14}$$

Δk is the wavevector or momentum mismatch along the propagation direction, given by

$$\Delta k = k_{z,s}+k_{z,i}-k_{z,p}+\frac{2\pi}{\Lambda}. \tag{2.1.15}$$

Note that quasi-phasematching with period Λ adds an extra term $2\pi/\Lambda$ in the momentum mismatch. This allows to engineer the poling period

$$\Lambda^{-1} = \frac{n_p(\lambda_p)}{\lambda_p} - \frac{n_s(\lambda_s)}{\lambda_s} - \frac{n_i(\lambda_i)}{\lambda_i} \tag{2.1.16}$$

such that phase-matching is achieved at the desired pump, signal and idler vacuum wavelengths $\lambda_{p,s,i}$.

To make these expressions tractable analytically, one must perform some approximations. A simple one is to expand the function $k_z(\mathbf{q},\omega)$ in expression 2.1.7 to first

nonvanishing order in $\mathbf{q}$ and ω. Note that $\nabla_{\mathbf{q}} k|_{\mathbf{q}=0} = 0$, so the expansion in transverse wavevector is done to second order.

$$\begin{aligned} k_z(\mathbf{q},\omega) &= k_z(0,\omega_0) + \frac{\partial k_z}{\partial \omega}|_{\omega=\omega_0,\mathbf{q}=0}\Omega + \frac{\partial}{\partial_{q_i,q_j}} k(\mathbf{q},\omega) q_i q_j + \mathcal{O}(q^3) \\ &= k_0 + \frac{1}{v_g(\omega_0)}\Omega - \frac{1}{2k_0}|\mathbf{q}|^2, \end{aligned} \tag{2.1.17}$$

where repeated indices imply summation. $v_g(\omega_0)$ is the group velocity at the central operating frequency ω_0 and Ω is the deviation from the central frequency, while $k_0 = \omega_0 n(\omega_0)/c$. Applying this expansion to pump, signal and idler and using them in expression 2.1.13 reads

$$\phi(\mathbf{q}_s,\mathbf{q}_i,\Omega_s,\Omega_i) = CL\tilde{E}_p(\mathbf{q}_s{+}\mathbf{q}_i)\mathrm{sinc}\left[\frac{L}{2}\left(\frac{\mathbf{q}_s^2}{2k_{0,s}} + \frac{\mathbf{q}_i^2}{2k_{0,i}} - \frac{(\mathbf{q}_s+\mathbf{q}_i)^2}{2k_{0,p}} + D\Omega_s\right)\right]\delta(\Omega_s{+}\Omega_i) \tag{2.1.18}$$

where $D \equiv \frac{1}{v_{g,s}(\omega_s)} - \frac{1}{v_{g,i}(\omega_i)}$.

Another approximation which can be performed is to replace the sinc function by a gaussian of the same width, leading to an expression for the mode function which can be integrated analytically. This calculation is out of the scope of this thesis and will not be pursued here.

To obtain numerical values of these expression, one needs values for the refractive index variation as a function of the crystal temperature, the wavelength of light in use and the orientation. We found that the Sellmeier and thermo-optic dispersion formulas for KTP measured by Kato et al. [50] reproduce perfectly our phase-matching temperature and bandwidth, so we will use them for all calculations. The expressions are given in Appendix C.

We now consider the effect on the biphoton state of the coupling into single mode fibers and the presence of frequency filters. To simplify the problem, we consider the case in which the back-propagated fiber modes are focused onto the center of the crystal by means of a system of lenses. The resulting modes, as seen at the crystal position, are the collection modes and are very well approximated by gaussian beams. At the focal point the electric field of the gaussian beam can be expanded as a superposition of plane waves, using the fourier transform:

$$\begin{aligned} E(x,y,0) &= E_0 e^{-\frac{x^2+y^2}{w_0^2}} \\ &= \int_{-\infty}^{\infty} dk_x dk_y \tilde{E}(k_x,k_y) e^{i(k_x x + k_y y)}, \end{aligned} \tag{2.1.19}$$

where

$$\begin{aligned} \tilde{E}(k_x,k_y) &= \frac{1}{(2\pi)^2}\int_{-\infty}^{\infty} dx dy E_0 e^{i\frac{x^2+y^2}{w_0^2}} e^{i(k_x x + k_y y)} \\ &= \frac{1}{4\pi} E_0 w_0^2 e^{-\frac{w_0^2}{4}\mathbf{q}^2}. \end{aligned} \tag{2.1.20}$$

The fiber collection modes can be regarded as spatial filters which project the biphoton state 2.1.12 into the state

$$|\phi_s, \phi_i\rangle = \int d^2\mathbf{q}_s d^2\mathbf{q}_i \exp\left(-\frac{W_{0,s}^2\mathbf{q}_s^2}{4}\right) \exp\left(-\frac{W_{0,i}^2\mathbf{q}_i^2}{4}\right) \hat{a}_s^\dagger(\mathbf{q}_s)\, \hat{a}_i^\dagger(\mathbf{q}_i)\, |0,0\rangle\,. \tag{2.1.21}$$

$W_{0,s}$ and $W_{0,i}$ are the waists of the backpropagated signal and idler fiber collection modes. We will assume that these waists are located at the center of the crystal. The fiber coupled biphoton state can then be written as

$$|\Psi_f\rangle = \int d\Omega \phi_f(\Omega)\, \hat{a}_{f,s}^\dagger(\Omega)\, \hat{a}_{f,i}^\dagger(-\Omega)\, |0,0\rangle \tag{2.1.22}$$

where $\hat{a}_{f,[s,i]}^\dagger(\Omega)$ create a signal or idler photon in the corresponding fiber mode with a frequency Ω displaced from the central frequency, and

$$\phi_f(\Omega) = \int d^2\mathbf{q}_s d^2\mathbf{q}_i \phi(\mathbf{q}_s, \mathbf{q}_i, \Omega) e^{-\frac{W_{0,s}^2\mathbf{q}_s^2}{4}} e^{-\frac{W_{0,i}^2\mathbf{q}_i^2}{4}}. \tag{2.1.23}$$

2.1.3. Second order correlation functions of narrowband photon pairs

We now assume that the signal and idler arms pass through frequency filters and are each sent to a single photon detector. The frequency filters have transmission functions $f_m(\omega)$, with $m = \{s, i\}$. The detectors are placed at distances z_s and z_i from the crystal back face. We want to calculate the probability of detecting a signal photon at time t correlated with the subsequent detection of an idler photon at time $t + \tau$. This probability, according to Glauber's photon detection theory, is proportional to the second order correlation function

$$\begin{aligned} G^{(2)}(z_s, t; z_i, t+\tau) &= \langle\Psi_f|\, E_s^\dagger(z_s,t) E_i^\dagger(z_i, t+\tau) E_i(z_i, t+\tau) E_s(z_s,t)\, |\Psi_f\rangle \\ &= |\langle 0,0|\, E_i(z_i, t+\tau) E_s(z_s,t)\, |\Psi_f\rangle|^2\,. \end{aligned} \tag{2.1.24}$$

To obtain the second line, we inserted the completeness relation between the two idler field operators and noted that the field operators only connect the state $|\Psi_f\rangle$ to vacuum. This allows to define a two photon wavefunction, as

$$\Psi_f(z_s, t; z_i, t+\tau) = \langle 0,0|\, E_i(z_i, t+\tau) E_s(z_s,t)\, |\Psi_f\rangle \tag{2.1.25}$$

whose square modulus gives the desired detection probability. To calculate it, we need to write down the signal and idler field operators seen by the detectors. We will assume that the frequency filters and detectors collect the entire spatial modes of the fibers, so we will only have to worry about the frequency part of the field distribution. We then write the signal and idler field operator as

$$\begin{aligned} \hat{E}_m(z_m, t) &= \int d\omega_m f_m(\omega_m) e^{i(k_z(\omega_m) z_m - \omega_m t)} \hat{a}_{f,m}(\omega_m) \\ &= \int d\omega_m f_m(\omega_m) e^{i\omega_m\left(\frac{z_m}{c} - t\right)} \hat{a}_{f,m}(\omega_m) \end{aligned} \tag{2.1.26}$$

with $m = \{s, i\}$. Replacing these in expression 2.1.25 reads

$$\begin{aligned}
&\Psi_f\left(z_s, t; z_i, t+\tau\right) \\
&\quad= \int d\omega_s d\omega_i d\Omega e^{i\omega_i\left(\frac{z_i}{c}-t-\tau\right)} e^{i\omega_s\left(\frac{z_s}{c}-t\right)} \phi_f(\Omega) f_s(\omega_s) f_i(\omega_i) \\
&\qquad\quad \times \langle 0,0|\, \hat{a}_{f,i}(\omega_i)\hat{a}_{f,s}(\omega_s)\hat{a}^\dagger_{f,s}(\omega_{s,0}+\Omega)\hat{a}^\dagger_{f,i}(\omega_{i,0}-\Omega)\,|0,0\rangle \\
&\quad= \int d\Omega e^{i(\omega_{s,0}+\Omega)\left(\frac{z_s}{c}-t\right)} e^{i(\omega_{i,0}-\Omega)\left(\frac{z_i}{c}-t-\tau\right)} \phi_f(\Omega) f_s(\omega_{s,0}+\Omega) f_i(\omega_{i,0}-\Omega) \\
&\quad= e^{-i(\omega_{s,0}+\omega_{i,0})t - i(\omega_{i,0}\tau) + i\frac{\omega_{s,0}z_s+\omega_{i,0}z_i}{c}} \int d\Omega e^{i\Omega\left(\frac{z_s-z_i}{c}\right)} e^{i\Omega\tau} \phi_f(\Omega) f_s(\Omega) f_i(-\Omega).
\end{aligned} \tag{2.1.27}$$

In the second line, the commutation relations $[\hat{a}_{f,m}(\omega_m), \hat{a}^\dagger_{f,n}(\omega_n)] = \delta(\omega_m - \omega_n)\delta_{m,n}$ have been used to take the annihilation operators to the right, giving terms which cancel. In the third line, we replaced $f_m(\omega_m + \Omega) \rightarrow f_m(\Omega)$. We can now drop the global phase factor and assume that the two detectors are placed at the same distance from the crystal $z_s = z_i$, to obtain

$$\Psi_f\left(t, t+\tau\right)) \propto \int d\Omega e^{i\Omega\tau} \phi_f(\Omega) f_s(\Omega) f_i(-\Omega). \tag{2.1.28}$$

Note that this is the Fourier transform of a product of three functions $\phi_f(\Omega)$, $f_s(\Omega)$ and $f_i(-\Omega)$ which can be calculated as the convolution of the three corresponding transformed functions $\tilde{\phi}_f(\tau), \tilde{f}_s(\tau), \tilde{f}_i(-\tau)$:

$$\Psi_f\left(t, t+\tau\right)) \propto \tilde{\phi}_f(\tau) \otimes \tilde{f}_s(\tau) \otimes \tilde{f}_i(-\tau). \tag{2.1.29}$$

In this convolution product, the factors with a bigger time spread (a smaller width of the corresponding spectral function) prevail, and the others can be approximated as delta functions. We will now analyze the width of the different functions in our experimental conditions.

The Fourier transform of the fiber coupled mode function $\tilde{\phi}_f(\tau)$ is in general hard to calculate. However, if the collection mode waists $W_{0,s}$ and $W_{0,i}$ are sufficiently big, the transverse wavevector distribution in 2.1.20 is very narrow so only terms with transverse wavevectors $\mathbf{q_s}$ and $\mathbf{q_i}$ close to zero in $\phi(\mathbf{q}_s, \mathbf{q}_i, \Omega_s, \Omega_i)$ contribute to $\phi_f(\Omega)$ in expression 2.1.23. If the approximate expression 2.1.18 for the mode function $\phi(\mathbf{q}_s, \mathbf{q}_i, \Omega_s, \Omega_i)$ is used with $\mathbf{q_s} = \mathbf{q_i} = 0$, its fourier transform is

$$\begin{aligned}
\tilde{\phi}_f(\tau) &= \mathfrak{F}\left\{\operatorname{sinc}\left(\frac{LD}{2}\Omega\right)\right\} \\
&= \frac{\sqrt{2\pi}}{DL}\Pi\left(\frac{\tau}{DL}\right),
\end{aligned} \tag{2.1.30}$$

where $\Pi(x)$ is the rectangle function, which is equal to 1 for $|x| < 1/2$ and 0 otherwise. The time spread of the transformed mode function is then $\delta t = DL$, where $D = v_{g,s}^{-1} - v_{g,i}^{-1}$, which is the difference in time of exiting the crystal for signal and idler photons created at opposite ends. For our case, in which the signal is polarized along the crystal axis 3 and idler along axis 2, at a temperature of 25° the group

velocities are $v_{g,s} = 1.579 \times 10^8$m/s and $v_{g,i} = 1.669 \times 10^8$m/s. For a crystal length of $L = 2$cm the resulting time spread is 6.84ps. This corresponds to a bandwidth (FWHM of $sinc^2$) of 130GHz. In the general case in which the collection modes are focused, these values are not exact but still a good approximation.

The transform of the filtering functions $\tilde{f}_m(\tau)$ can be easily obtained in our case, since we will be using cavity filters. We use expression A.0.13 derived in appendix A, which has a Fourier transform

$$\begin{aligned}\tilde{f}(\tau) &= \mathfrak{F}\left\{\frac{1}{1 - i\frac{2\Omega}{\delta\omega}}\right\} \\ &= e^{\frac{\delta\omega}{2}\tau}\Theta(-\tau),\end{aligned} \tag{2.1.31}$$

where $\Theta(\tau)$ is the heaviside step function. This function has a time spread of $2/\delta\omega$. In our case, we use a filter with a linewidth of $\delta\omega_{filter} = 2\pi \times 22$ MHz, so the time spread is 14.4ns, at least three orders of magnitude higher than the mode function spread.

The second order correlation function $G^{(2)}(t, t+\tau)$ can now be easily calculated for different cases of interest. For the situation of the measurements we performed to characterize the photon bandwidth, explained in section 6.1, the signal photon is not filtered, thus $f_s = 1$, and is sent to the start detector. The idler photon is filtered with a two cavity setup resulting in the aforementioned effective filtering linewidth of 22 MHz. Hence $f_i(-\Omega) = 1/(1 + i2\Omega/\delta\omega_i)$. The resulting $G^{(2)}(t, t+\tau)$ correlation function is

$$G^{(2)}(t, t+\tau) \propto e^{-\delta\omega_{filter}\tau}\Theta(\tau), \tag{2.1.32}$$

which is a decreasing exponential with the time constant given by the inverse of the cavity linewidth, i.e. the cavity decay time.

In the second case of interest, the signal photon is filtered and sent to a detector, serving as a trigger for the presence of the idler photon, hence $f_s(\Omega) = 1/(1 - i2\Omega/\delta\omega)$. The idler photon is not filtered and sent directly to a single ion, thus $f_i(\Omega) = 1$. The resulting second order correlation function is

$$G^{(2)}(t, t+\tau) \propto e^{\delta\omega_{filter}\tau}\Theta(-\tau), \tag{2.1.33}$$

an increasing exponential with the same time constant as the last case. This $G^{(2)}(t, t+\tau)$ can be interpreted as the waveform envelope of idler photon going to the ion conditioned on the detection of a trigger photon. We note that it is a time reversed waveform of a spontaneously emitted photon by an ion decaying in a transition with a linewidth of 22 MHz, which turns out to be the ideal waveform shape for optimum absorption efficiency.

2.2. Design of the frequency filter: optimum bandwidth considerations

When designing the source, we were faced with the question of what the ideal frequency bandwidth of the filter should be, given the linewidth of the atomic tran-

sition we would like to address with it. We are concerned with the case in which one of the output channels of the source is not filtered, and directed to the ion, while the second arm is filtered and monitored by a single photon detector. As will be shown later, we have available a scheme to detect the absorption of the photon by the ion. Since this photon can only be absorbed if its spectrum lies within the atomic absorption spectrum, we can consider the ion as a spectral filter in itself, with a fixed bandwidth of $\delta\Omega_i$. The question is what the ideal value for the bandwidth of the source filter, $\delta\Omega_s$, should be. To answer this, we must first decide what mathematical merit function we would like to optimize.

Since the goal of the experiment is to observe the correlations between the absorption of one photon by the ion and the detection of the partner photon, we have to optimize the signal to noise ratio (SNR) in the resulting correlation function. Two key properties of the $g^{(2)}(\tau)$ correlation function between the two events determine the SNR. The first is the number of correlations at zero time delay, which determines the signal, $C = g^{(2)}(0)$. The second is the average level of the background of the $g^{(2)}(\tau)$ at all time delays τ, $BG = \overline{g^{(2)}(\tau)}$, which is produced by accidental correlations between randomly distributed events. The background level BG will contribute noise to the measurement of the real correlations C. Assuming that the background counts follow poissonian statistics, we can estimate the noise level in an individual point, and in particular in $\tau = 0$, as $N = \sqrt{BG}$. The SNR is therefore given by,

$$SNR = \frac{g^{(2)}(0)}{\sqrt{\overline{g^{(2)}(\tau)}}} \tag{2.2.1}$$

To understand the problem in question, let's consider the limiting cases. If $\delta\Omega_s \gg \delta\Omega_i$, most of the cases when the ion absorbs a photon will find a corresponding detection of the partner photon. The number of real time correlations C between the two events will increase. However, many trigger photons will be detected which fall in a frequency outside of the atomic transition bandwidth, and therefore will have a partner photon which can not possibly be absorbed by the ion. This will result in an increase in the accidental correlations, and therefore in the background BG and in the noise N. The situation is exactly reversed in the opposite case, $\delta\Omega_s \ll \delta\Omega_i$. Very few real correlations will be observed, and at the same time a lower rate of accidental correlations will happen. Therefore, there must be an optimum situation between these two cases. The SNR in Equation 2.2.1 is the merit function that must be optimized in the design of the filtering bandwidth.

We shall now proceed to obtain an expression for the SNR in terms of the ion absorption bandwidth $\delta\Omega_i$ and the source filtering bandwidth $\delta\Omega_s$. The filter transmission f_s and the ion absorption spectrum f_i are modeled with a lorentzian function,

$$f_{i/s}(\Omega) = \frac{1}{1 + \left(\frac{2\Omega}{\delta\Omega_{i/s}}\right)^2}. \tag{2.2.2}$$

The rate of events in each individual channel will be proportional to the integral of

these spectra,

$$R_{i/s} \propto \int_{-\infty}^{\infty} f_{i/s}\left(\Omega\right)\, d\Omega = \frac{\pi}{2}\delta\Omega_{i/s}. \tag{2.2.3}$$

Since the background rate of the correlation function is proportional to the product of the single channel count rates,

$$BG \propto \frac{1}{4}\pi^2\delta\Omega_i\delta\Omega_s. \tag{2.2.4}$$

Now we write an expression for the correlation rate. For simplicity, we assume that we are in the perfect collinear case, so the bi-photon mode function $\Phi(\Omega_s, \Omega_i)$ does not depend on the transverse momenta of the two photons. In this case, the mode function from equation 2.1.18 is written as

$$\Phi(\Omega_s, \Omega_i) = \mathrm{sinc}\left(\frac{DL\Omega_s}{2}\right)\delta(\Omega_s + \Omega_i) \tag{2.2.5}$$

The correlation rate will then be given by

$$C \propto \int\int_{-\infty}^{\infty} \Phi(\Omega_s, \Omega_i) f_i(\Omega_i) f_s(\Omega_s)\, d\Omega_i d\Omega_s. \tag{2.2.6}$$

Since the filtering bandwidths are much smaller than the biphoton bandwidth, the sinc factor can be assumed to be constant. Therefore, the correlation rate is proportional to

$$C \propto \int_{-\infty}^{\infty} f_i(\Omega) f_s(\Omega)\, d\Omega = \frac{\pi}{2}\frac{\delta\Omega_i\delta\Omega_s}{\delta\Omega_i + \delta\Omega_s}, \tag{2.2.7}$$

where we have used the fact that $f_{i/s}(\Omega)$ are symmetric functions.

Finally, the signal-to-noise ratio is given by

$$SNR(\delta\Omega_i, \delta\Omega_s) = \frac{\sqrt{\delta\Omega_i\delta\Omega_s}}{\delta\Omega_i + \delta\Omega_s}. \tag{2.2.8}$$

Given $\delta\Omega_i$, this function has a maximum at $\delta\Omega_s = \delta\Omega_i$. Therefore, the source bandwidth must be identical to the atomic transition linewidth in order to optimize the signal-to-noise ratio. There are two interesting issues concerning this problem. First, note that the correlation rate itself only reaches half its maximum value when the two filters are identical and the maximum rate is given for a filter of infinite bandwidth. Second, note that the single-to-background ratio (SBR), which is given by $SBR \propto 1/(\delta\Omega_i + \delta\Omega_s)$, has its maximum at zero bandwidth, where the correlation rate vanishes. Therefore, the SBR can never be a good merit function for the filter design.

This result formalizes the somewhat intuitive idea that the filtering bandwidth must be the same as the atomic absorption bandwidth. This was one of the design goals of the source.

3. The entangled photon pair source: experimental setup

A schematic overview of the setup is presented in Figure 3.1. A tunable and frequency stabilized laser source, tuned and locked to the atomic transition, is amplified and frequency-doubled. This light then pumps the down-converter, where entangled photon pairs around half the pump frequency are generated. The two photons are split by a beam-splitter and coupled into single-mode optical fibers. One of them is coupled into a spectral filter assembly with a transmission bandwidth designed to match that of the atomic transition, after which it is sent to a single-photon detector. The other one is either directly coupled to another single-photon detector or sent to a single-ion experiment.

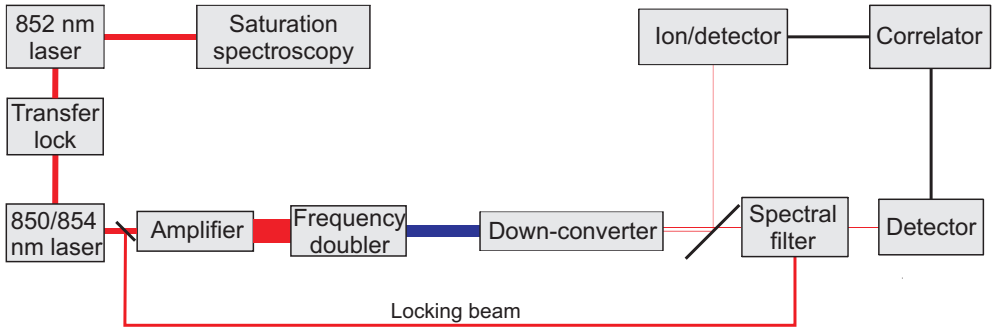

Figure 3.1.: Scheme of the experimental setup: The master 850/854 nm laser is stabilized, by means of a transfer lock, using a second auxiliary 852 nm laser stabilized to a Cesium atomic line (saturation spectroscopy). After an amplification and doubling stage, it is down-converted in a degenerate collinear configuration (down-converter). The generated photon pairs are split. One is coupled into a spectral filter and sent to a single photon detector, and the second one is either used to interact with a single ion, or detected. A time correlator (PicoHarp) detects the coincident pairs.

A picture of the setup is shown in Figure 3.2. The source is mounted on an optical breadboard placed on top of an optical table. This was decided to be able to transport it to the neighboring lab where the ion setup is, if necessary. In the end, the photons from the source were sent to the ion lab through an optical fiber so the breadboard wasn't really necessary, although it is still convenient to transport the

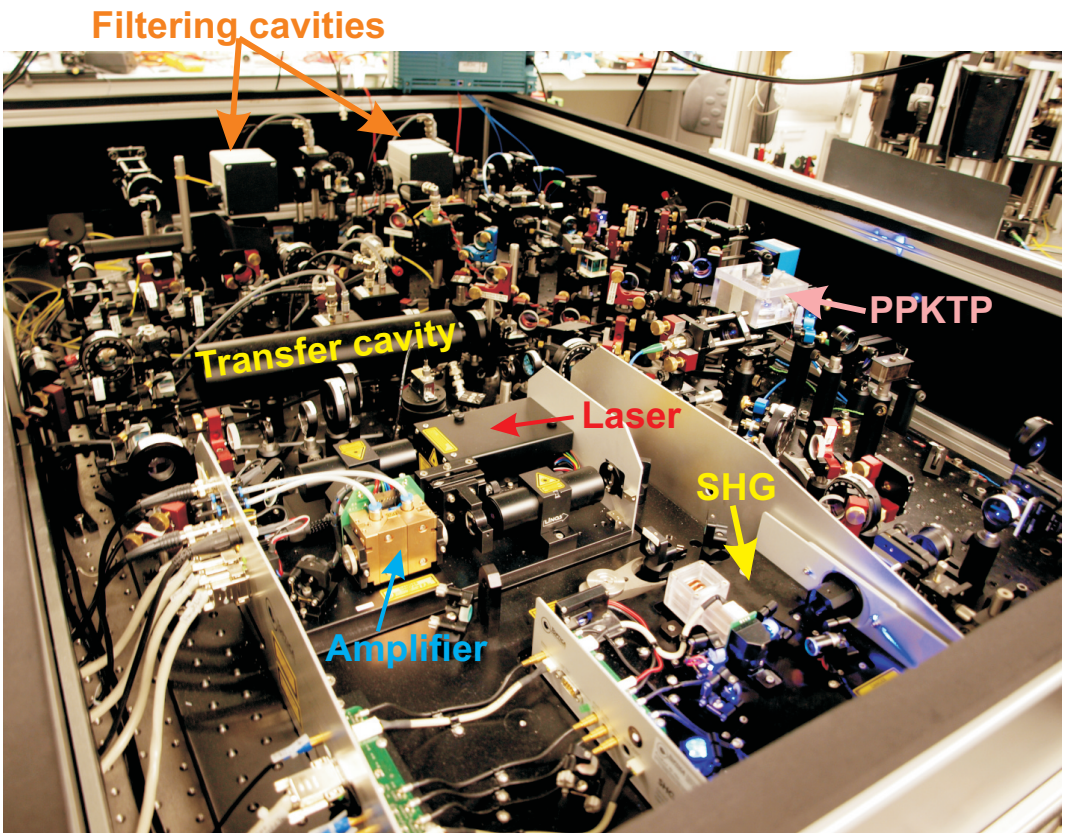

Figure 3.2.: Photo of the experimental setup of the source.

experiment.

The setup is surrounded by a box with covers which allows to isolate it from environmental light and noise. This turns out to be extremely useful to minimize the background in the single-photon detectors due to stray light without having to turn off the lab lights.

The main parts of the experiment are shown in the figure, namely the laser-amplifier-doubler system, the nonlinear crystal mount (PPKTP) and the filtering cavity mounts. A detailed description and characterization of each element in the setup will be given in the following sections.

3.1. Laser source and stabilization

In this section, the laser source for the down-conversion pump and the frequency stabilization technique is presented. Figure 3.3 shows a detailed scheme of the setup.

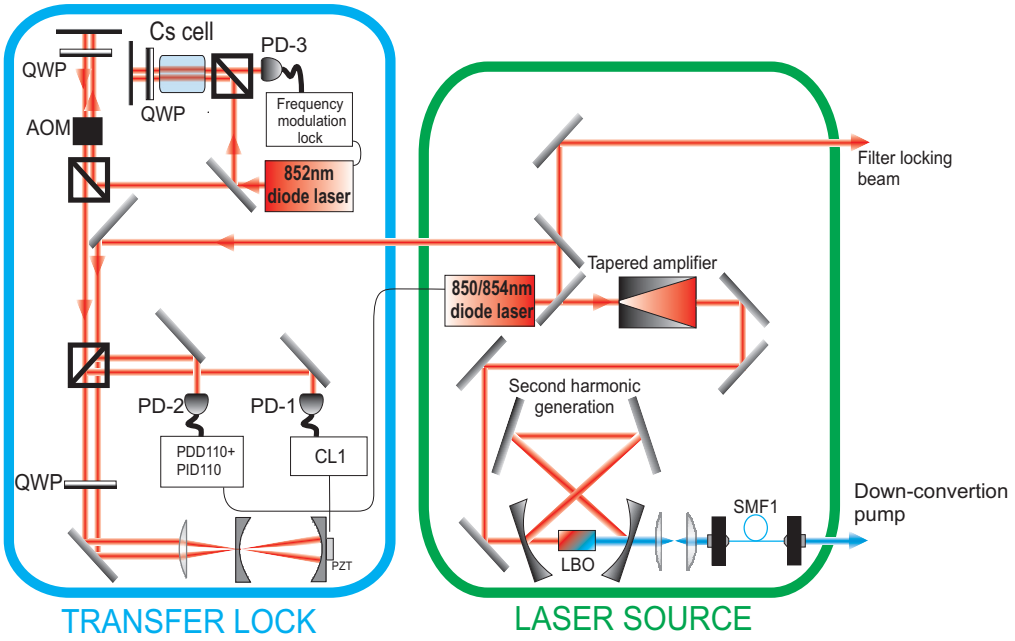

Figure 3.3.: The laser source and the frequency stabilization scheme.

3.1.1. Laser source

The laser source consists of a commercial amplified and frequency-doubled diode laser (Toptica TA-SHG 110), hereafter referred to as the master laser. The laser is an extended cavity diode laser in *Littrow* configuration. In this type of configuration a reflection diffraction grating is placed right at the output of the diode laser under an angle such that the diffraction order $m = -1$ is back reflected into the diode, while order zero is used as an output beam. The grating then acts as a frequency selective back-reflector. As a result, the laser emission spectrum is narrowed and its central emission frequency can be tuned by varying the grating angle. In our laser, this angle is controlled by a piezo placed behind the grating. The voltage applied to this piezo is a control signal over the laser frequency.

This system provides a continuous-wave laser beam of around 30 mW power, tunable to the $D_{3/2} - P_{3/2}$ and $D_{5/2} - P_{3/2}$ transitions in $^{40}Ca^{+}$ ions at 850 and 854 nm, respectively. A small fraction of this beam of about 3 mW is coupled out of the system and is used for stabilization, as will be described later. The rest is injected into a tapered amplifier, which provides an output power of up to 600 mW. This powerful beam is coupled into a second harmonic generation module consisting of a Lithium Triborate (LBO) crystal placed within a bow-tie cavity resonant with the pump beam. The output beam is at exactly half the wavelength of the pump (425 or 427 nm), and its typical power is around 100 mW.

Due to spatial walk-off in the non-linear crystal, the output beam has a highly elliptical shape. A cylindrical lens telescope is used to circularize the beam for optimum fiber coupling efficiency. For this, we carefully measured the beam shape

at different distances using a ccd camera and fitted a 2D gaussian function. We then obtained two complex gaussian beam q-parameters, which were matched using the methods described in Appendix B.

The shape corrected beam is then coupled into a polarization maintaining single-mode fiber, SMF1 (OZ-optics QPMJ-3A3A-300-3.5/125-3-2-1), and outcoupled using fiber collimators (Schäfter-Kirchhoff 60FC-4-M12-33). The overall transmission through the fiber is typically 55-65%. Fiber coupling this beam is convenient to clean the laser spatial mode and to uncouple the alignment of the laser source from the down-converter. This last point is essential since the second harmonic generation stage has to be realigned very often to maintain a high power, but this produces a spatial shift in the output beam. Without fiber coupling the whole down-conversion path would be misaligned. By fiber coupling this beam, whenever the SHG stage is realigned, it is enough to recover the fiber coupling into SMF1.

3.1.2. Frequency stabilization

The frequency lock of the laser has been designed to provide both absolute frequency stability and bandwidth reduction of the laser, as well as course and fine tunability through both transitions of interest. For this purpose, a second laser source at 852 nm, hereafter referred to as the reference laser, is first locked to one of the hyperfine transitions in the D2 line of cesium, using frequency modulation on the laser current at 20MHz and Doppler-free saturation spectroscopy (see Figure 3.3). Fine frequency tuning of the reference laser is achieved by a double-pass acousto-optic modulator (AOM, Brimrose) setup, as shown in the figure. For more details on this locking technique see reference [46, 51].

To transfer the stability of this laser to the master laser, a 15 cm long confocal Fabry-Perot reference cavity with a finesse of ~ 1000 is used. The length of this cavity is stabilized to the reference laser, while the master laser is locked to the cavity.

The stabilization of the cavity to the 852 nm reference laser is illustrated in Figure 3.4(a). Both mirrors are mounted on a rigid aluminium tube wound with a heating wire, allowing to apply heat on the cavity mount. A temperature sensor (Pt-100) is attached to the central part of the tube to monitor the cavity temperature. One of the cavity mirrors is attached to a piezo-electric transducer (PZT). To lock the cavity to the reference laser we use the Pound-Drever-Hall (PDH) technique. A phase modulation is applied to the reference laser by modulating its current with a 20MHz oscillator, applied to the Bias-T input of the Toptica laser module. The electric field of this beam can be expressed as

$$E(t) = \frac{1}{2}E_0\left[e^{i\omega t+\beta\sin(\Omega_{mod}t)}\right] + c.c. \tag{3.1.1}$$

which can be expanded, to first order in the modulation amplitude, as

$$E(t) = \frac{1}{2}E_0\left[J_0(\beta)e^{i\omega t} + J_1(\beta)e^{i(\omega+\Omega_{mod})t} - J_1(\beta)e^{i(\omega-\Omega_{mod})t}\right] + c.c. \tag{3.1.2}$$

where J_n is the Bessel function of first kind of order n. As a result of the modulation, two sidebands displaced by $\pm\Omega_{mod}$ from the central frequency ω appear.

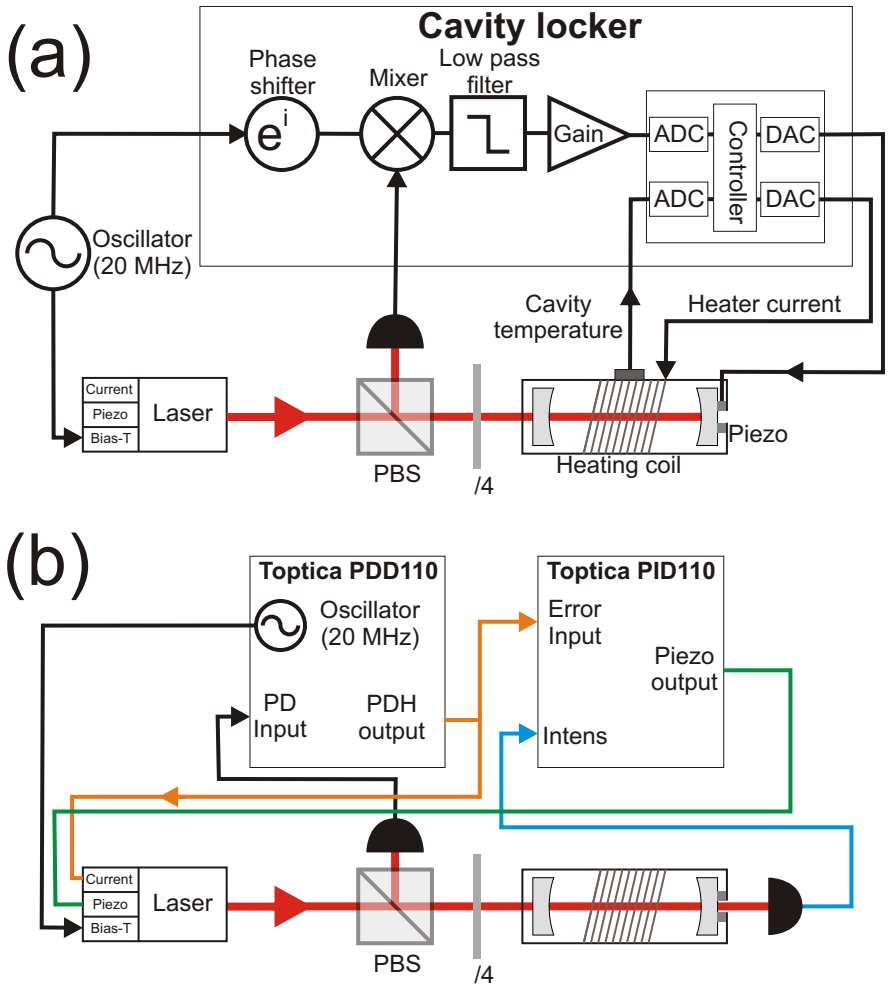

Figure 3.4.: Illustration of the two frequency stabilization schemes in use.

As shown in Figures 3.3 and 3.4(a), the reference laser beam is coupled to the cavity and the reflected signal is collected on a fast photodiode (PD1 in Figure 3.3). Let $f_r(\omega)$ be the cavity reflection spectrum for which we use expression A.0.5, with a reflectivity of $r = 99.36\%$ and a free spectral range of $FSR = 500$ MHz yielding a cavity linewidth of $\delta\omega = 2\pi \times 1$ MHz. Then, the electric field reflected from the cavity is

$$E_r(t) = E_0 \left[J_0(\beta) f_r(\omega) e^{i\omega t} + J_1(\beta) f_r(\omega + \Omega_{mod}) e^{i(\omega+\Omega)t} - J_1(\beta) f_r(\omega - \Omega_{mod}) e^{i(\omega-\Omega)t} \right]. \tag{3.1.3}$$

The photodiode voltage is proportional to the power of the field :

$$\begin{aligned} P(t) &= |E_r(t)|^2 \\ &= P_c |f(\omega)|^2 + P_s \left[|F(\omega + \Omega_{mod})|^2 + |F(\omega - \Omega_{mod})|^2 \right] \\ &\quad + 2\sqrt{P_c P_s}\{ \\ &\quad\quad \Re\left[\mathcal{E}(\omega, \Omega_{mod})\right] \cos(\Omega_{mod} t) + \Im\left[\mathcal{E}(\omega, \Omega_{mod})\right] \sin(\Omega_{mod} t) \\ &\quad \} \end{aligned} \tag{3.1.4}$$

where $\mathcal{E}(\omega, \Omega_{mod}) = f_r(\omega) f_r^*(\omega + \Omega_{mod}) - f_r^*(\omega) f_r(\omega - \Omega_{mod})$, $P_0 = |E_0|^2$ is the power of the field incident into the cavity, $P_c = J_0(\beta) P_0$ is the power of the carrier and $J_1(\beta) P_0$ is the power of the first sidebands. The signal from this photodiode is sent to the PD input terminal of the cavity locker (CL1), a home-built electronic module used to obtain the error signal and lock the cavities (Figure 3.4(a)) [39]. The cavity locker takes the input from the photodiode and mixes it with the same radio-frequency oscillator at Ω_{mod} used to modulate the laser current. After the mixer, the signal takes the form

$$V_m = \Re[\mathcal{E}(\omega, \Omega_{mod})] \sin(\phi) + \Im[\mathcal{E}(\omega, \Omega_{mod})] \cos(\phi) + 2\Omega_{mod}\text{terms} \tag{3.1.5}$$

where ϕ is the phase of the oscillator with respect to the photodiode signal, controllable with the phase shifter present in the circuit. The low-pass filter gets rid of the $2\Omega_{mod}$ terms. The resulting signal is plotted in Figure 3.5(a) for a cavity linewidth of 1 MHz and in 3.5(b) for 20 MHz, with the corresponding cavity reflection signals, for a phase shift of $\phi = 0$. The reference cavity, having a linewidth of $\sim 1MHz$ corresponds to case (a). Case (b) corresponds to the case of one of the filtering cavities, discussed in section 3.5.

The resulting error signal is then sent to an analog-to-digital converter (ADC) and then to a digital microcontroller card (Analog Devices ADuC7026) which implements two cascaded digital regulators. The first regulator feeds back a compensation signal to the cavity piezo, to maintain the cavity on resonance. The second regulator takes as an error signal the displacement of the piezo voltage from its central value of 0V and feeds back a compensation signal to the heater coil. This maintains the piezo always within its operation range. The microcontroller also accepts an additional input from the PT100 temperature sensor. When not in locking mode, a regulator takes this temperature reading and feeds back to the cavity heating coil to stabilize the cavity temperature. A temperature setpoint allows to set the desired cavity temperature.

To complete the locking chain the master laser is locked to a different longitudinal mode of the length-stabilized Fabry-Perot cavity. This is done by coupling a second beam from this laser into the cavity through a different spatial mode, so that it can be split from the reference beam. The reflected beam is then detected by a second photodiode (PD2 in 3.3 or 3.4(b)). The signal from PD2 is again demodulated and amplified by a commercial Pound-Drever-Hall detector (Toptica - PDD110). Its output signal is split in two parts, one of which is fed back directly to the current of the laser through the FET input, and the other one is sent to a

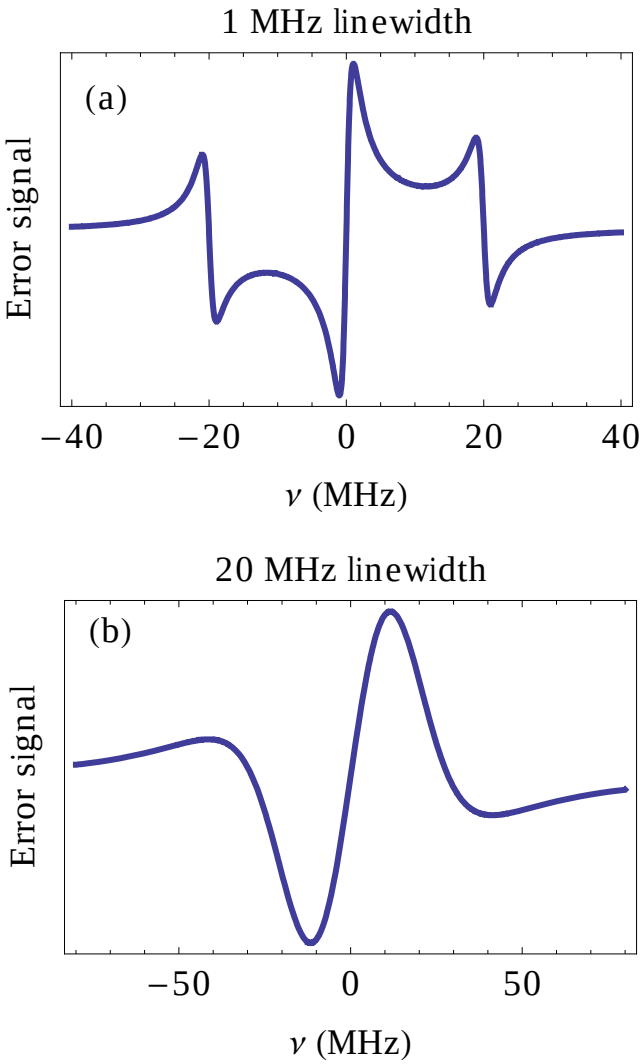

Figure 3.5.: Calculated Pound-Drever-Hall error (blue) with the corresponding cavity reflection signal (red) for a modulation frequency of 20 MHz and a cavity linewidth of (a) 1 MHz and (b) 20 MHz.

commercial PID regulator (Toptica PID110). The output of this module is fed back to the piezo moving the laser grating. The slow piezo feedback stabilizes the mean frequency of the laser, while the current feedback provides a bandwidth reduction. This technique yields a laser linewidth of around 120 kHz and an absolute stability during several hours below 130 kHz [46, 51].

While locked, the laser frequency may be tuned over a range of up to 150 MHz by changing the AOM frequency. The entire locking chain can follow AOM frequency steps lower than the cavity linewidth of 1 MHz. Note that a change $\Delta\nu_{852}$ in the frequency of the 852 nm reference laser does not correspond exactly to the same change $\Delta\nu_{850}$ in the 850 laser since they are resonant with two different lon-

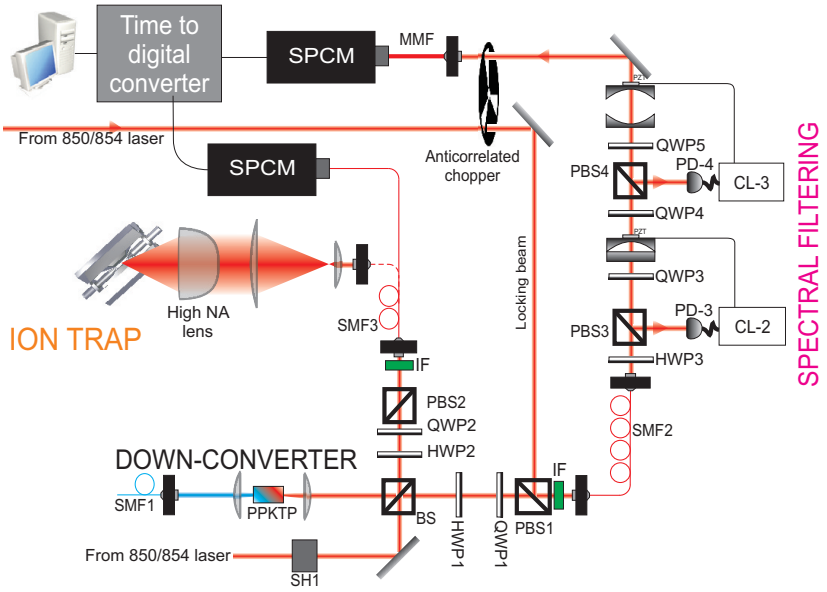

Figure 3.6.: The down-conversion and filtering stages. The meaning of the symbols used are: SMF: single-mode fiber, MMF: multi-mode fiber, HWP: half wave-plate, QWP: quarter wave-plate, PBS: polarizing beam-splitter, PD: photo-diode, CL: cavity locker, IF: interference filter, SH: optical shutter

gitudinal modes of the cavity. The two frequency changes are related by $\Delta\nu_{850} = \frac{\lambda_{852}}{\lambda_{850}}\Delta\nu_{852} \simeq 1.00235\Delta\nu_{852}$. To achieve tunability in a higher range, the master laser must be locked to a different longitudinal mode of the cavity. This changes the laser frequency in steps of the reference cavity FSR of 500 MHz. In order to cover the intermediate spectral range (between the 150 MHz AOM range and the 500 MHz FSR), the mode on which the cavity is locked to the reference laser must be modified. This is achieved by changing the cavity length through its temperature. In this way, a tunability of 0.14pm/°C (58 MHz/°C) is achieved.

3.2. Down-conversion crystal properties

Figure 3.6 shows a detailed schematic of the down-conversion setup and the filtering stage. The down-converter is a periodically poled $KTiOPO_4$ (PPKTP) crystal of dimensions $20 \times 6 \times 1$ mm oriented along the y-x-z crystallographic axes, respectively. In the longer direction it has two independent parallel poling gratings imprinted, with periods of 14.03 and 14.63 μm, designed for collinear type-II quasi-phase-matching at a temperature of 25°C for 849.8 and 10°C for 854.2 nm, respectively. The unusual and inconvenient temperature of operation of the second wavelength resulted from a mistake in the calculation of the poling period. This crystal was obtained through a collaboration with a Swedish research group

at KTH[1], who at the time of production did not have perfect knowledge of the refractive indexes of their KTP crystals. We then consulted the literature for these and found that two authors gave slightly different values for the same type of crystal [50, 52]. Being unable to conclude which was the correct value in our case, we decided to build a crystal with two different gratings for each wavelength, one for each set of refractive indices. An additional constraint in the fabrication was that only three gratings were possible, so we had to chose only one grating for one of the wavelengths. We then decided to make two different gratings for 849.8 nm using both references, and picked reference [52] for the grating at 854.2 nm, all designed for operation at 25°. It turned out that the correct values were the ones given in Ref. [50] (see Appendix C), so the period of the third grating was wrong. However, the poling period was not far from the correct value, and this allowed to achieve quasi-phase-matching at 10°. This is an inconvenient temperature to work at since water condensation at normal lab humidities sets in. To avoid it, we built a container with a dry environment around the crystal, as described in the following section.

3.3. Crystal temperature stabilization

The crystal is mounted on a small copper holder, which sits on top of a Peltier element attached to a U-shaped aluminium base plate. On the sides of this plate, heat dissipators are attached and contacted with highly temperature conductive paste. The U-shape piece is designed such that three plexiglass sheets can be attached to it, one on the top, one on the rear and one on the front, to make a closed box and produce a dry air environment around the crystal. The front and rear sheets have small holes to allow access for the input and output beams. A dry air inlet valve is attached to the top sheet. This entire box containing the crystal mount is fixed on top of a set of x-y-z translation stages and a 3-axes rotation stage allowing for fine alignment of the crystal in all degrees of freedom.

Two temperature sensors, a Pt-1000 and an NTC thermistor, are fixed in two holes close to the crystal in the copper holder. The Pt-1000 is used to measure the temperature accurately, while the NTC, with a higher response, is used for temperature stabilization. A high performance temperature controller (Wavelength electronics PID-1500) is used to stabilize the temperature with a precision better than ± 10 mK. The controller sends a small current of 200 μA to the NTC sensor and measures the resulting voltage from which a setpoint voltage is subtracted. The final error signal is fed to a proportional-integral amplifier and the resulting signal is fed back to the Peltier element current. The setpoint is controlled through an external voltage input, which allows for automatic control of the crystal temperature through the LabVIEW experiment control program. Two additional output signals from the temperature controller module give readings of the setpoint and actual temperature values. The experiment control program is designed to keep track of all these temperatures for every measurement that is performed, and can additionally perform custom scans of the crystal temperature.

[1]The crystal was fabricated by C. Canalias from the Laser physics department of the KTH in Stockholm.

Figure 3.7.: Down-conversion crystal mounting.

To lower the temperature of the crystal below the lab atmosphere due point, for example to achieve phase-matching at 854 nm (at 10°), the crystal box must be filled with dry air or nitrogen. Since the box contains holes for optical access, the dry air will diffuse through them, so a small flux of air through the inlet valve is always necessary to compensate for this diffusion. For good control on this, a humidity sensor was inserted inside the box to monitor the humidity at all times, and an air flow meter was installed in the dry air supply tube. In practice, a flux of less than 0.2L/minute is enough to keep the relative humidity inside the box below 10%. At this humidity and at a temperature of 25°, the due point is below -7°. To supply the dry air we use a 10L bottle at an initial pressure of 200mbar, which then provides around 10000 minutes of operation time before having to be refilled.

3.4. Fiber coupling of photon pairs

The down-conversion pair generation rate, as well as the coupling efficiency of the produced photons into the single-mode collection fibers strongly depends on all the modes involved in the process and also on the parameters of the nonlinear crystal. It is therefore necessary to carefully choose the focusing lens for the pump beam, as well as the collimating lenses for the signal and idler beams. Which waist size for the pump, signal and idler optimize the generation and collection efficiency is a complicated matter. The standard procedure to theoretically study this is to optimize the square modulus of the fiber coupled biphoton amplitude, given in expression 2.1.23, with respect to the three beam waists $W_{0,s}$, $W_{0,i}$ and $W_{0,p}$.

This problem is treated extensively in the literature with different approaches. For example, Kurtsiefer et al. give a simple way to calculate the angular distribution of the emitted light given the spectral filtering bandwidth and to match it to the fiber mode [53]. Bovino and coworkers use a more precise calculation, based on the fiber coupled biphoton wavefunction, such as in Equation 2.1.22, to obtain an analytical relation between all relevant experimental parameters that optimizes the collection efficiency [54]. A similar analysis was performed numerically by Ljunggren et al. [55] and an experimental optimization was performed by Fedrizzi et al. [56].

However, all these results apply to systems in which no filtering of the down-converted photons is performed or a very broad filter is used, which does not correspond to our case. We therefore took a different approach, motivated by the work in [57]. This paper concludes that the fiber-coupled efficiency of degenerate filtered down-converted photons is proportional to the efficiency of fiber-coupled second harmonic generated light in the reverse direction. This is a very useful result for our setup, since it means that we may optimize the rate of our photon pair source in the following way: send infrared 850 or 854 nm light backwards through the collection fibers, check for the blue 425/427 nm unconverted blue light, couple it into the blue fiber and maximize the blue power at its output. It is much easier to optimize the up-converted relatively powerful light than the weak down-converted beam. Moreover, with this in mind the theoretical results of Boyd and Kleinmann on the optimum modes for fiber coupled up-conversion can be applied. Namely, the Rayleigh range z_R of the collection modes (the pump mode in up-conversion) must satisfy the condition $L/z_R = 5.68$ [58]. The corresponding pump mode (the collection mode in the up-conversion process) must be a factor of $\sqrt{2}$ smaller than than the collection mode. For our configuration, with a crystal length of 20 mm and a down-converted wavelength of 854 nm, we find that the optimal collection mode should have a waist[2] of 30.9 μm and the corresponding pump mode waist of 21.8 μm.

In our setup, the collimated single-mode blue beam from fiber SMF1 (see Figure 3.6) is focused onto the crystal by a 200 mm focal length lens, producing a waist size of 22 μm. The generated photon pairs are collimated by a 150 mm focal length lens and split by a beam-splitter (BS). The latter is either a non-polarizing beam-

[2]The beam waist is the $1/e^2$ diameter of intensity profile

splitter (NPBS), if the polarization entanglement of the photons is required, or a polarizing beam-splitter (PBS), if it is not. Both output modes of the beam splitter are coupled into polarization maintaining single-mode fibers SMF2 and SMF3 of 0.11 NA (OZ-optics PMJ-3A3S-850-5/125-3-2-1) using 11 mm focal length aspheric lenses (Thorlabs C220TME-B). The lens distance to the fiber is adjustable and is set to produce a collection mode waist size in the center of the crystal of 31 μm.

Each fiber coupler is attached to a 6-axis kinematic mount (Thorlabs K6X), and the fibers are mounted on translation stages movable along the optical axis (Thorlabs SM1Z), thereby allowing precise fiber to collimator distance control. Furthermore, the whole fiber coupling system is mounted on a set of horizontal and vertical micrometer precision translation stages (Standa 7T184-13 and 7VT174-10).

3.5. Spectral filtering stage

The fiber SMF2 in the transmission arm of the beam splitter is coupled to a filtering stage for bandwidth reduction of the photon pairs. The beam is first collimated using a 4.5 mm focal length fiber collimator (Thorlabs F230FC). It is then coupled to two cascaded Fabry-Perot cavities with an overall transmission spectrum designed to block the whole bandwidth of the generated photon pairs except for a transmission window corresponding to the atomic transition linewidth. The transmission window can be tuned by active feedback stabilization of the Fabry-Perot cavities.

3.5.1. Filtering cavity mounts

Each resonator consists of two low loss cavity mirrors (Layertec). One mirror is glued onto a low voltage ring-stacked piezo actuator (PiezoMechanik HPSt 150/14-10/12), to control the cavity length. Each resonator is built on a custom designed kinematic mount, allowing to set precisely the cavity length and the angle between the mirrors. A CAD drawing of the design is shown in Figure 3.8. The mirror without piezo is glued directly to an aluminium plate with a cylindrical groove at the center, such that the mirror is centered in the mount. Similarly, the piezo holding the second mirror is glued to a second aluminium plate with a groove of the proper size. Each of these plates have a hole on the center to allow for optical access, and three holes for screws on the sides. They are fixed to the main block by means of screws. The cavity mount is attached to a set of horizontal and vertical translation stages and a yaw-pitch rotation stage. Both cavity mount systems and all the additional optics are attached to a linear rail (Eksma 810-0005). This rail provides ease of alignment of all the components. The rail has a scale engraved on it, which allows to place the components at specific distances between them with good precision and reproducibility. Additionally, it makes the whole filtering stage portable after it has been mounted. Since the cavity position can be adjusted in all degrees of freedom, no additional mirrors are required to align them. A photograph of the filtering stage is shown in Figure 3.9.

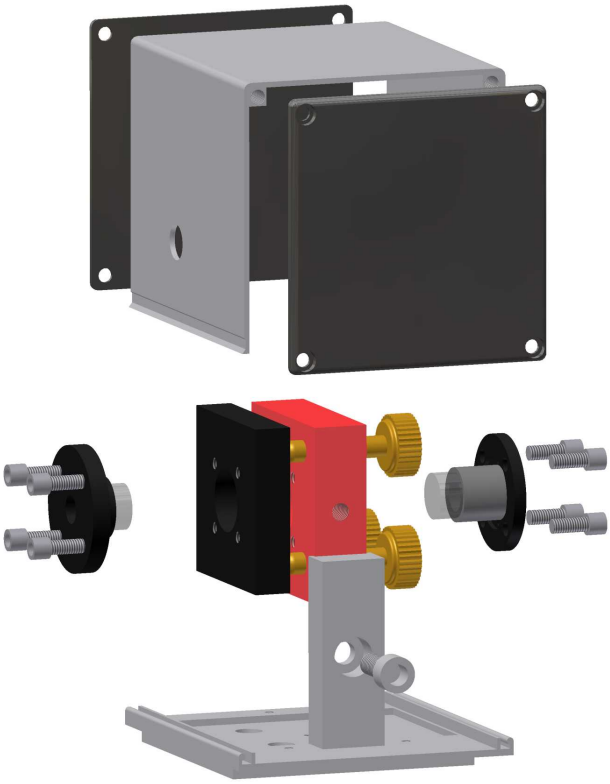

Figure 3.8.: CAD drawing of the cavity mount design.

3.5.2. Cavity filter spectral design

The filtering stage was designed with several goals in mind. First, the transmission on resonance should be as high as possible while keeping a sufficient extinction out of resonance. Second, the transmission spectrum should cover the whole SPDC emission spectrum, which was initially estimated to be around 0.5 nm = 208 GHz (at 850 nm). In addition, the transmission bandwidth of the system should coincide with the atomic transition linewidth ($\sim$ 22 MHz). Note that to achieve these conditions with a single Fabry-Perot cavity would require a free spectral range (FSR) greater that 208 GHz and a linewidth of 22 MHz, which would correspond to a Finesse of $\sim 10^4$. A cavity of such a finesse and with high transmission on resonance cannot be built without considerable technical difficulties. First, it would be necessary to mount it under vacuum to avoid air absorption losses, which are not

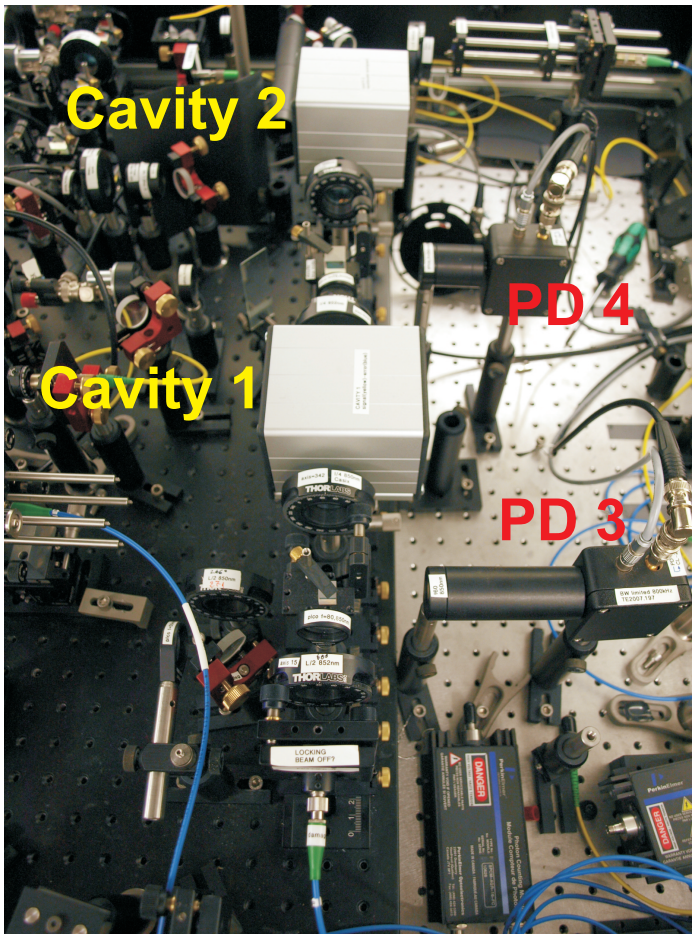

Figure 3.9.: Photo of the filtering stage, composed of two cascaded Fabry-Perot cavities. All elements are mounted in a linear rail, allowing to easily displace and fix them to the desired distances.

negligible at this Finesse. Second, it would require using mirrors with extremely high quality optical coatings, with transmittivity below 100 ppm and losses below 10 ppm.

To avoid these complications, we chose to use a system composed of two cascaded cavities of lower finesse. The first cavity was designed so that its FSR is one order of magnitude higher than the bandwidth of the crystal emission spectrum, therefore transmitting in a single longitudinal mode. Furthermore, the FSR of the second cavity is designed to be significantly higher than the linewidth of the first cavity, and so that its bandwidth is equal to the desired value of 22 MHz. This is done by choosing appropriate values of the mirror reflectivities and cavity lengths, according to expressions A.0.9 and A.0.10. All mirrors were specified to have the same reflectivities of 99.5%, in a wavelength range of 800 to 900 nm, and low losses $L \lesssim 10^{-3}$, to achieve the impedance matching condition (see Eq. A.0.6) and maximum cavity transmission. For these values, we expected a finesse of $F = 616$, and

Length	$\Delta\nu$ [MHz]	FSR [MHz]	Transmission
100 μm	2435.07	1.5×10^6	0.961169
11 cm	22.137	13636.4	0.961169

Table 3.1.: Designed spectral properties of the filtering cavities.

we set the cavity lengths to $L_1 = 100$ μm and $L_2 = 11$ cm. With this, we expected the cavity spectral values given in table 3.1.

Regarding the cavity mirror geometries, both cavities are implemented with mirrors of 12.5 mum diameter. The short cavity is implemented with a plane and a curved mirror (plano-concave), the curved mirror having a radius of 1 m. This allowed to achieve a cavity length of 100 μm. The long cavity is bi-concave with mirrors of 15 cm radii.

After building the cavities, their transmission spectra were experimentally characterized by performing laser spectroscopy on them. For characterizing the broadband cavity, the 852 nm laser was mode-matched and coupled into it and the transmission was monitored with a photo-diode (details on the mode-matching will be given in the next section). At the same time, the signal from the cesium saturation spectroscopy obtained with the same laser was monitored, providing an absolute frequency reference. The laser frequency was scanned through the resonance of the cavity, and both the cavity transmission and Cs-spectroscopy signals were recorded simultaneously. The result is shown in Figure 3.10. The saturated absorption peaks, shown in the insets, were identified as the transitions between the different hyperfine levels in the $S_{1/2}$ and $P_{3/2}$ manifolds. From lower to higher frequencies, the respective transitions are $|6^2S_{1/2}, F = 3\rangle \leftrightarrow |6^2P_{3/2}, F = 4, 3, 2\rangle$ and $|6^2S_{1/2}, F = 4\rangle \leftrightarrow |6^2P_{3/2}, F = 5, 4, 3\rangle$, and the corresponding crossovers. These peaks were used to calibrate the frequency axis in the scans, using the transition frequencies deduced from the splittings of the excited level given in [59] and the exact splittings of the ground state, given by the current definition of the second. The resulting bandwidth of the short cavity, after fitting a lorentzian function to the data, is 2.5373 ± 0.0005 GHz (FWHM).

The bandwidth of the narrowband cavity was measured by coupling through it the 850 nm laser and modulating its current with a $\nu_m = 20$MHz oscillator. The resulting frequency modulation produced frequency sidebands at $\pm n\nu_m, n = 0, 1, 2, ...$, with amplitudes which decrease strongly with n. The carrier 850 nm laser frequency was then scanned through the cavity resonance. The transmission spectrum of the cavity was recorded with and without frequency modulation, as shown in Figure 3.11. The former case, shown in the inset, provides a calibration of the frequency axis. The cavity linewidth is then obtained by fitting a lorentzian to the modulation-free peak and taking into account the time calibration. The resulting cavity linewidth is 22.51 ± 0.11MHz

Finally, we also obtained an estimation of the crystal emission spectrum. This was done by coupling down-converted light transmitted through cavity 1 directly to the SPCM and measuring the coincidence rate as a function of the piezo voltage, while scanning it through the emission spectrum (Figure 3.12). The piezo voltage

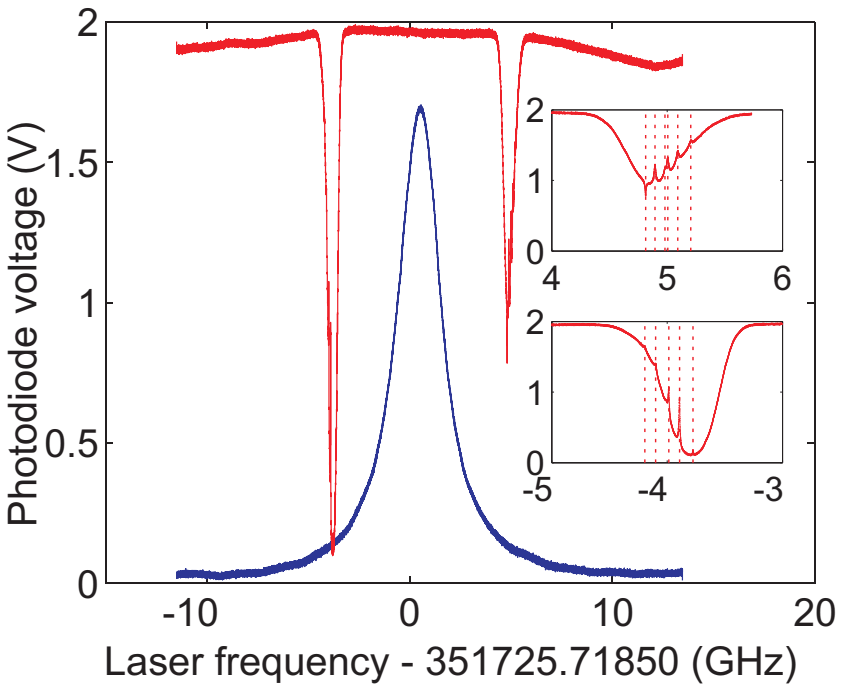

Figure 3.10.: Measurement of the broad cavity linewidth. The 852 nm laser was scanned through the cavity resonance (blue data) and through the D-lines of Cesium in a vapor cell (red data) using saturation absorption spectroscopy. The saturation peaks (inset) were used to calibrate the time axis.

to frequency calibration was obtained by performing a full FSR scan. A Gaussian fit to the data yields a FWHM of the photon pair spectrum of 143 ± 7 GHz and a single photon bandwidth of 202 ± 10 GHz.

3.5.3. Measuring the cavity lengths

We also measured precisely both cavity lengths to obtain their FSRs. For this, note that the resonance condition of the $TEM_{m,n,q}$ mode of a spherical mirror cavity, with longitudinal mode number q and transverse mode numbers m, n is given by equation A.0.22, which can be rewritten as $d = \frac{c}{2\nu}\left[q + \frac{\Delta\xi(d)}{\pi}(m+n+1)\right]$. Here d is the cavity length and ν is the laser frequency. $\Delta\xi(d)$ is the Gouy phase shift, which reads $\Delta\xi(d) = 2\arccos[(1-d/R)]$ for a symmetric cavity with mirror radii R and $\Delta\xi(d) = 2\arccos\left(\sqrt{1-d/R}\right)$ for a plano-concave cavity of length d and with the concave mirror having radius R. Note that the variation of the Gouy phase shift is negligible when the cavity length is changed by half a wavelength (one FSR). Therefore, to obtain the length of each cavity, we can scan its piezo over more than half a wavelength and we determine the ratio between the transverse mode

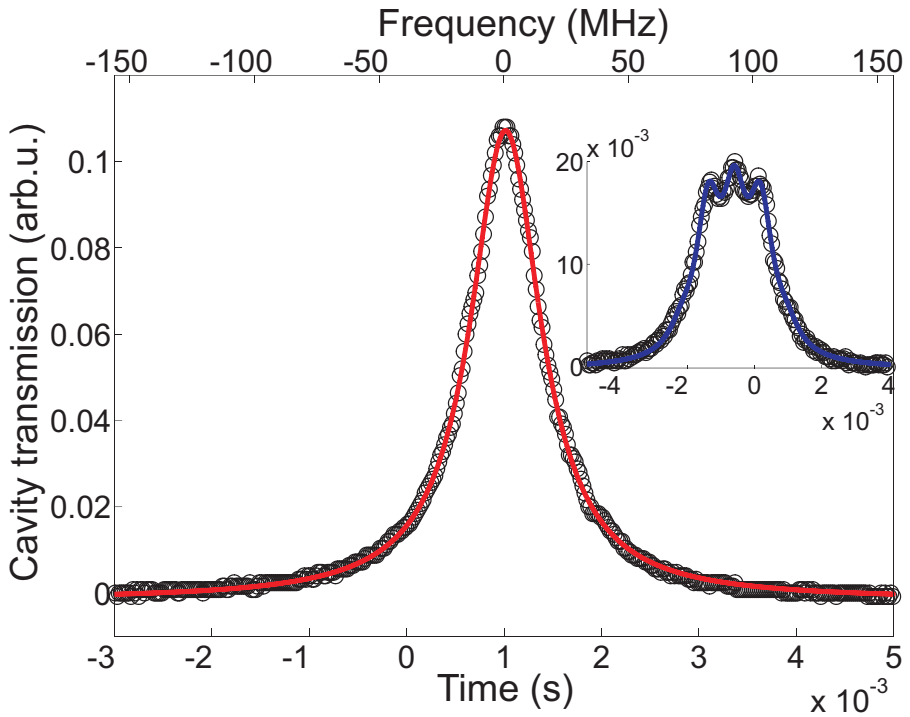

Figure 3.11.: Measurement of the narrow cavity linewidth. The 850 nm laser was scanned through the cavity. The solid line is a lorentzian fit to the data. In the inset, a second scan was preformed, now with a 20 MHz frequency modulation producing sidebands in the cavity transmission spaced by 20MHz. A superposition of a symmetric set of lorenztian lines were fitted to obtain a time-frequency calibration (solid curve).

spacing and the longitudinal mode spacing, $\frac{d_{1,0,q}-d_{0,0,q}}{d_{0,0,q}-d_{0,0,q+1}} \equiv r$. The Guoy shift is then given by $\Delta\xi = \pi r$ and, knowing the cavity mirror radii, the cavity length is $d = R\,(1-\cos\Delta\xi)$. Finally, the $FSR = \frac{c}{2d}$ and the cavity finesse is $F = FSR/\delta\nu$. All the relevant spectral properties of the crystal and cavities are given in Table 3.2 for comparison.

The crystal emission spectrum together with the combined cavity transmission spectra are plotted in Figure 3.13.

3.5.4. Mode matching

In general, a laser beam incident on a Fabry-Perot cavity is decomposed into a superposition of the different transverse cavity modes, designated as $\mathrm{TEM}_{m,n}$ (see Appendix A). If these modes are not degenerate, which is usually the case for a non-confocal cavity, only one of these modes is resonant at a given cavity length. The cavity would only transmit the part of the input beam which projects onto this mode. Therefore, for optimum transmission of the filter, the input beam must be

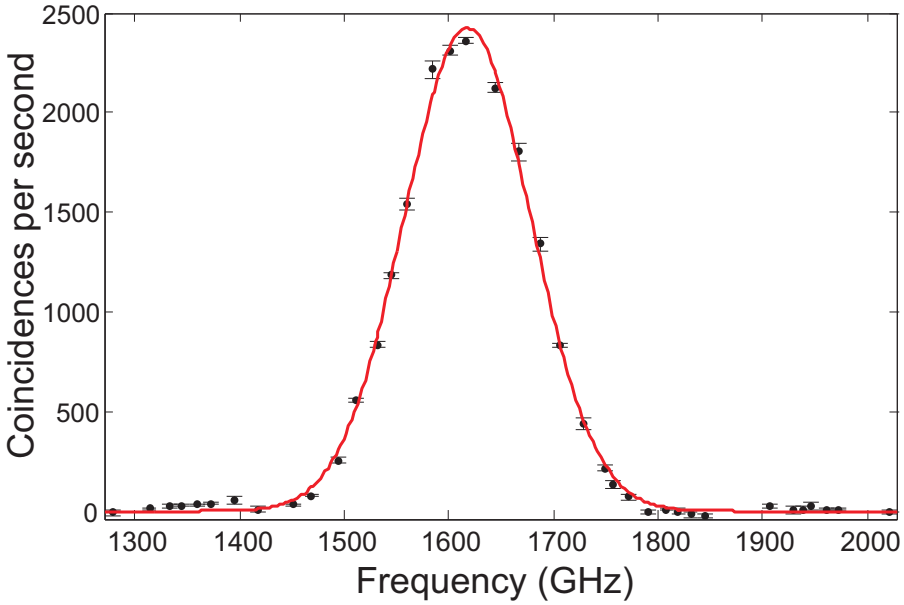

Figure 3.12.: Fiber-coupled crystal coincidence spectrum measured by recording the coincidences while scanning the voltage of the filtering cavity 1. The frequency was calibrated by performing a scan over the full free spectral range. The solid line is a Gaussian fit to the data revealing a bandwidth of 143(7) GHz.

mode-matched to only one of these modes, typically the $TEM_{0,0}$. This mode is a well defined gaussian beam which is calculated from the measured cavity length and the mirror curvature. In our case, the input laser mode is also a well defined gaussian beam since it is coupled out of a single-mode fiber. Hence, the input beam and the cavity mode may be perfectly matched by means of a single spherical lens. Note that the output beam of the first cavity is also a gaussian beam, and it may be matched in the same way to the input mode of the second cavity.

To achieve this, a single plano-convex lens before each cavity is used. We first measured the beam mode after the fiber collimator using a ccd camera. We measured the beam profile at different longitudinal positions and fitted a gaussian func-

Element	**Bandwidth (MHz)**	**FSR (GHz)**	**Finesse**	**Length (mm)**	**Decay time (ns)**
Crystal	$202(10) \times 10^3$	-	-	-	-
Cavity 1	$2.5373(5) \times 10^3$	$1.92(4) \times 10^3$	759(14)	$78(2) \times 10^{-3}$	627.26(12)
Cavity 2	22.51(11)	14.60(2)	649(11)	10.274(17)	7.07(3)

Table 3.2.: Measured properties of the filtering cavities and the crystal emission. The displayed values are the cavity bandwidths, free spectral ranges (FSR), lengths, and the photon decay time out of each cavity.

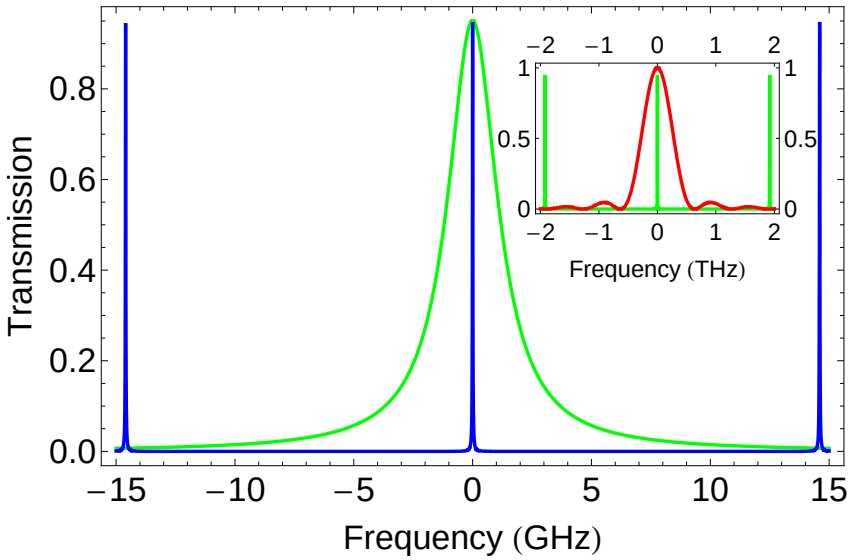

Figure 3.13.: Illustration of the combined spectra of the two filters and down-conversion emission. In blue, the narrowband filter of 22.5 MHz linewidth. In green, the broader filter with a linewidth of 2.5GHz. In the inset, the broad filter is shown together with the crystal emission spectrum of 202GHz.

tion to each profile. The resulting gaussian widths were then plotted as a function of the longitudinal position, and a fit of expression $W(z - z_0)$ given by A.0.20 was performed to obtain the relevant beam parameters z_R, z_0. From this, the complex beam parameter $q = z_0 + iz_R$ was obtained. We then performed a gaussian beam propagation simulation through all optical elements in the filtering stage, taking into account the thickness of the lenses and cavity mirrors. The fiber collimated mode is matched to the mode of the first cavity by an 80 mm focal length lens. Additionally, the transmission mode of this cavity was matched to the mode of the second cavity by means of a 70 mm lens. Figure 3.14 shows the resulting geometry of the entire beam-line for optimal mode matching. With this optimum mode matching, a transmission efficiency through each cavity of 95% was reached.

As mentioned earlier, the use of a linear rail system to place the cavities and the lenses with a calibrated scale is of great convenience to put the calculated distances between lenses and cavities into practice. In fact, after placing the elements at the calculated values, the optimum mode-matching condition was reached without having to empirically change their distances much.

The best method to align the filtering cavities is to implement a setup as shown in figure 3.15. A photodiode placed in reflection (or in transmission) allows to monitor the distribution of cavity modes and a CCD camera monitoring the cavity transmission allows to identify each mode. While scanning the length of the cavity, the different transverse modes show up in the camera, and a decrease in reflected power is observed in the photodiode. By keeping the cavity length fixed

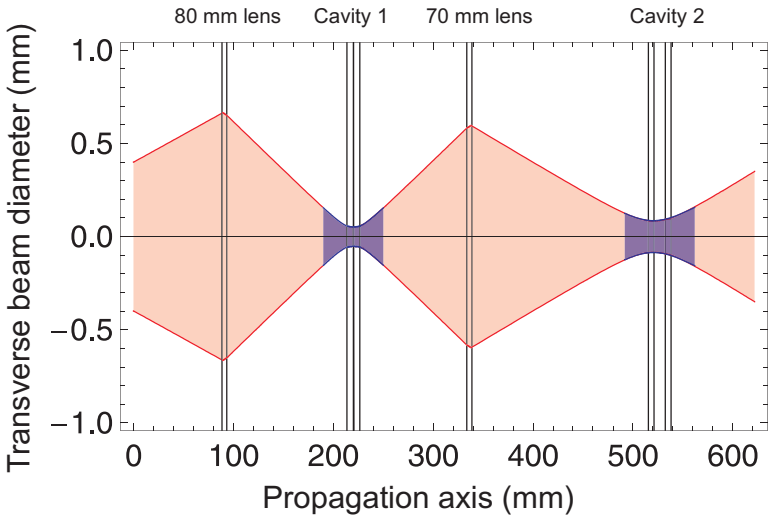

Figure 3.14.: Propagation of the beam in the filtering stage (light red), and the cavity modes propagated through the cavity mirrors (dark blue). The input mode, on the left, is the measured mode out of the SMF2 outcoupler. The beam passes through an 80 mm focal length lens, couples through the first cavity mirror and is matched to the cavity mode calculated from the measured cavity length. It then propagates to the second cavity through a 70 mm focal length lens to match its mode. The lenses and cavity mirrors were modeled with their specified interface curvatures and spacings and literature values of BK7 were used for the refractive index. The calculated optimum positions for the elements were verified experimentally to give near-perfect mode matching.

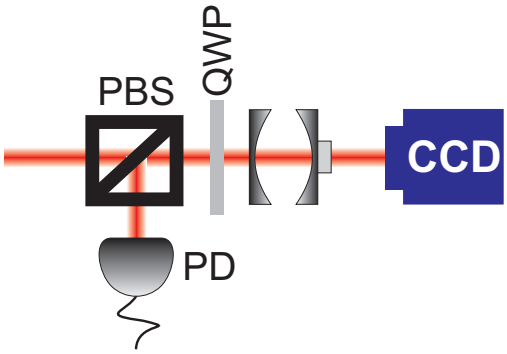

Figure 3.15.: Setup for aligning the filtering cavities. PBS: Polarizing beam-splitter, PD: Photodiode, QWP: quarter-wave plate, CCD: ccd camera

on resonance with one particular transverse mode, its profile can be recorded by

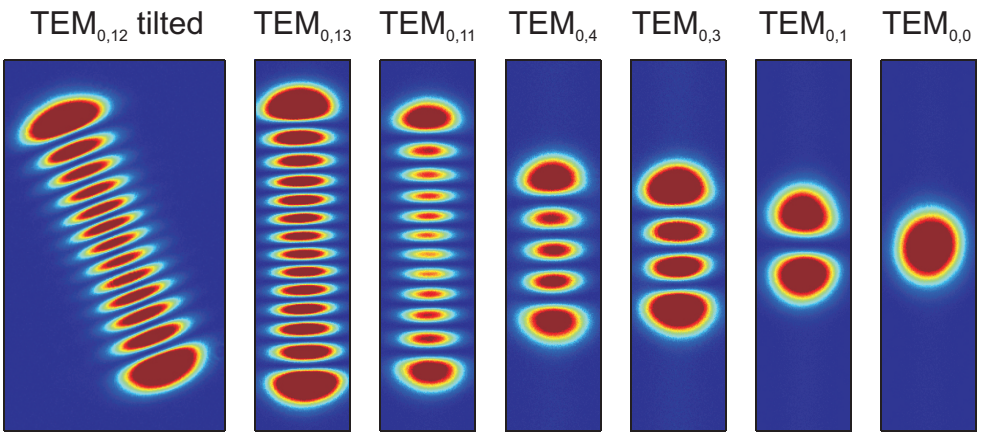

Figure 3.16.: Images observed with the CCD camera when the cavity length was kept fixed at particular transverse modes.

the camera (Figure 3.16). This allows to identify the mode that corresponds to each dip in the reflected signal, as shown in Figure 3.17.

A procedure to align the cavity is describes in the following. Scan the cavity length periodically with a triangular wave. While observing the mode profile in the CCD camera, assuming a mode profile such as in the leftmost panel of Figure 3.16, rotate and laterally displace the cavity until the mode become vertical as in the following panels. Move the cavity vertically and tilt it along the vertical plane to reduce the intensity of high order modes, while increasing the intensity of lower order ones. When reaching a situation in which only the set of lowest order modes are visible in the camera, do the fine alignment while monitoring the photodiode signal. The signal will look something like in the bottom panel of Figure 3.17. Try to reduce as much as possible the relative intensity of higher order modes, using the CCD camera to identify them if necessary, while moving the cavity in all degrees of freedom. For the final reduction of higher order modes the cavity must be "beam-walked".

If higher order dips do not vanish while aligning the cavity transversely, its longitudinal distance must be varied. Repeating this process iteratively leads to a situation in which higher order mode dips are not visible, as in the top panel of Figure 3.17. The inset shows a zoomed trace of the fundamental mode dip. A lorentzian fit yields a suppression in reflection of up to 96%. The remaining reflection is probably due to imperfect impedance matching, as explained in Appendix A.

3.5.5. Stabilizing the cavity length

The length of each filtering cavity is actively stabilized to be on resonance with the master laser. For this, an auxiliary master laser beam, hereafter named the locking beam, is coupled to the cavities through the reflection port of a polarizing beam splitter (PBS1) before the single-mode fiber SMF2 (see Figure 3.6). At the output

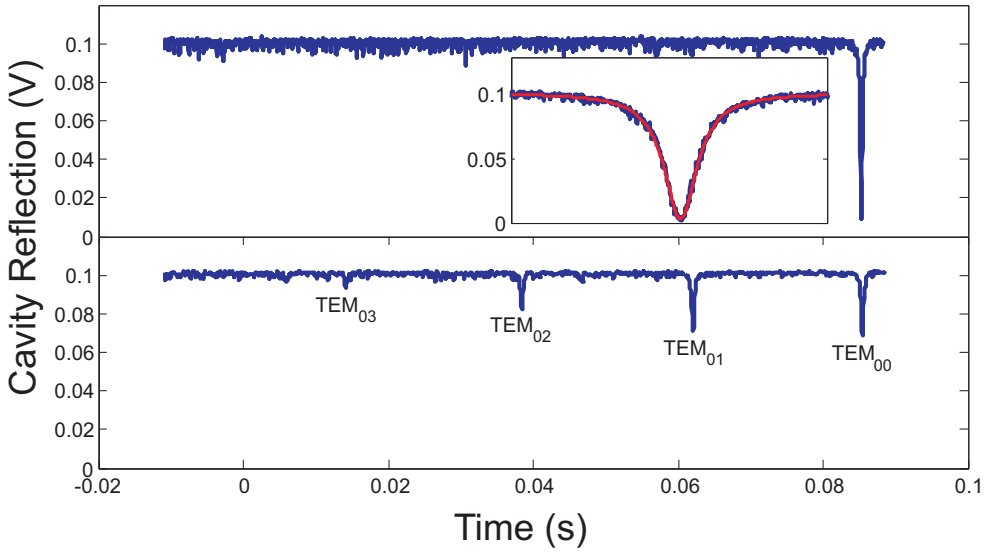

Figure 3.17.: Reflection signal measured by the photodiode while scanning the cavity length. In the top panel, the cavity is properly aligned and mode matched so a strong dip is observed only for the fundamental TEM_{00} mode, and higher order modes are suppressed. The inset shows a zoom into the dip of the TEM_{00} mode in the mode-matched case, indicating that the cavity reflection is suppressed to up to 96%. The bottom panel shows a case in which the cavity is not properly aligned to the beam, and thus the cavity mode is not matched to the input beam.

port of SMF2, a half-wave plate (HWP3) is used to slightly rotate the polarization of the locking beam, which at this point is vertical, allowing a small part of it to be transmitted through PBS3. This also induces a small, but controllable loss of the order of less than 1% of the down-converted photons, which are horizontally polarized. The locking beam then passes through a quarter-wave plate (QWP3) and reaches cavity 1. By a set of QWPs and PBSs the back-reflected locking beams from each cavity are coupled to fast photo-diodes for cavity stabilization.

Cavity 1, which has a broad linewidth, is stabilized using another cavity locker unit (CL-2), as for the reference cavity. In this case, the cavity length is modulated with a 50 kHz oscillator, which excites a high order resonance of the piezo. The reflection signal from the cavity (PD3) is demodulated with the same oscillator. The resulting signal is the derivative of the cavity reflection, and is therefore an adequate error signal for stabilizing the cavity length. A PID regulator implemented in a micro-controller then produces the final compensation signal, which is fed back to the piezo transducer. For cavity 2, the same technique as for the reference cavity is used, making use of the 20 MHz laser frequency modulation to produce a PDH signal. Cavity locker CL-3 provides the compensation signal which is fed back to the piezo. The transmission of both cavities is coupled to a single-photon-

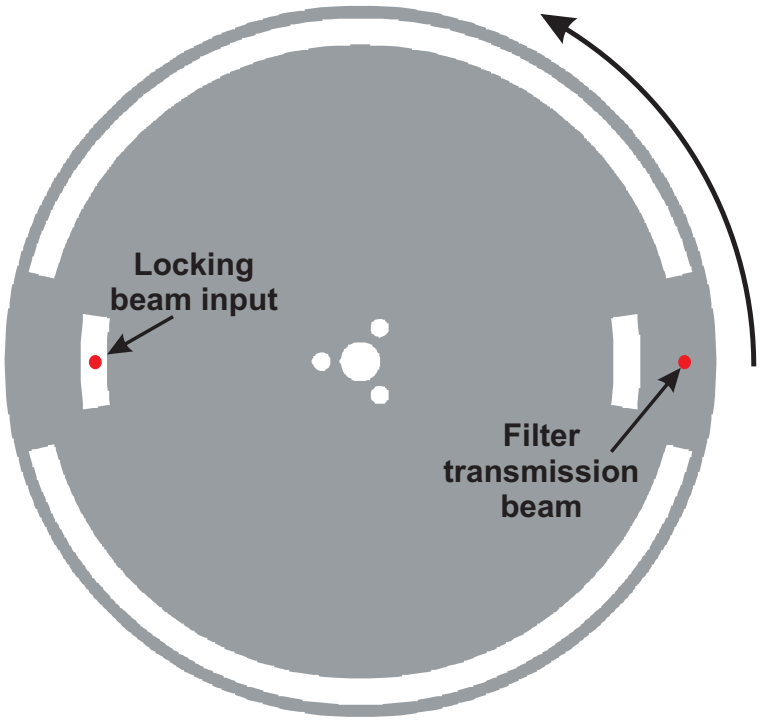

Figure 3.18.: Design of the chopper disk to avoid exposing the avalanche photodiode in the transmission of the filtering stage to the locking beam. A security margin in which both locking and transmission are blocked is necessary due to the finite diameter of the beam. For optimum chopping speed, the beam is focused at the chopper position.

counting-module (SPCM) through a multimode fiber (MMF). To avoid exposing the detectors to the relatively powerful locking light, the transmission of the filtering cavities passes through one side of an optical chopper. The locking beam, before being coupled into the filtering stage, passes through the opposite side. The chopper design, shown in Figure 3.18, is such that the transmission/blocking ratio is about $85:15$, meaning that the cavities are stabilized 15% of the time.

Thanks to the rigid mounting of the cavities and their relatively short length, they are passively very stable when the locking beam is chopped off. The cavities usually remain on resonance with the locking beam during several hours without any strong external mechanical perturbation. In case they fall out of lock, an automatic relocking function implemented in the cavity lockers makes them find the resonance again. For this, the reflection signals from PD-3 and PD-4 are monitored at all times by the CL-2 and CL-3, respectively. If one of the signals exceeds a predefined threshold, meaning that the cavity is out of lock, the corresponding cavity locker interrupts the feedback loop and performs a scan on the piezo voltage. When the reflection signal falls below the threshold again, the feedback is reactivated.

Cavity	Relocking threshold (mV)	Error signal set-point (V)
1	50	1.25
2	45	0.1

Table 3.3.: Relevant parameters of the cavity lockers

The feedback stabilization and relocking functions are only performed during the phase when the locking beam is on. An additional photo-diode (not shown in the Figure) monitors the power of the locking beam. Together with a comparator this provides a digital signal to the cavity lockers of the state of the locking beam. This same signal is later used in the experiments of interaction with the ion to trigger the experimental loop.

Note that for the relocking mechanism to work, the cavity reflection photodiode signals must be set such that they exceed the threshold value when the cavity is out of resonance and decrease below it when it is on resonance. Table 3.3 displays the relocking threshold values and the setpoint voltages of the two cavities.

4. Ion traps

The second part of the setup involved in the experiments presented in this thesis is an ion trap apparatus capable of storing a single $^{40}Ca^{+}$ ion or linear strings of a few ions. This setup was constructed in parallel to the source and the details are presented in three other PhD theses. Here we give a brief summary of the relevant features for completeness.

4.1. Ion Trapping

Ion trapping was first achieved by Wolfgang Paul in 1953 using a combination of static and dynamics electric fields, and later by Hans Georg Dehmelt in 1959, using static electric and magnetic fields. The first kind, nowadays known as Paul traps, are widely used in quantum information processing experiments, while the second kind, known as Penning traps, are mostly used for precision measurements of atomic properties. Both Paul and Dehmelt were awarded the Nobel prize in 1989 for their inventions.

To confine a charged particle in three dimensions using a static electric field, a potential of the form $V(x,y,z) = \alpha x^2 + \beta y^2 + \gamma z^2$ with $\alpha, \beta, \gamma > 0$ would be required. However,such a potential does not satisfy Laplace's equation, which requires $\nabla^2 V = 2(\alpha + \beta + \gamma) = 0$. Nevertheless, three-dimensional confinement with electric fields is possible if these are time dependent. The operation of Paul traps relies on the so-called Ponderomotive force experienced by a charged particle in a time dependent inhomogeneous electromagnetic field. Let $\mathbf{E}(\mathbf{r})$ be the amplitude of an electric field oscillating at frequency Ω_{rf}. Neglecting the effects of the weak associated magnetic field, a particle with charge q and mass m experiences a time-averaged force given by $\mathbf{F}_{pm}(\mathbf{r}) = -\nabla U_{pm}(\mathbf{r})$, where

$$U_{pm}(\mathbf{r}) = \frac{q^2}{4m\Omega_{rf}^2}|\mathbf{E}(\mathbf{r})|^2. \tag{4.1.1}$$

is the potential energy of the particle averaged over the fast oscillation. Note that this force does not depend on the sign of the charged particle, and is attractive if $|\mathbf{E}(\mathbf{r})|$ increases with the distance to the origin $|\mathbf{r}|$. It has an easy interpretation, noting that in each period of oscillation, at the turning point further away from the center the particle experiences a higher force than in the turning point closer to the center. The charge then suffers a net force inwards. The motion produced by this force is the so-called secular motion. In addition, the particle also suffers a fast driven force at frequency Ω_{rf}, producing the so-called micro-motion.

In our labs we use radio-frequency driven (RF) linear Paul traps, originally designed by the Blatt group in Innsbruck [60]. Their geometry consists of four blade

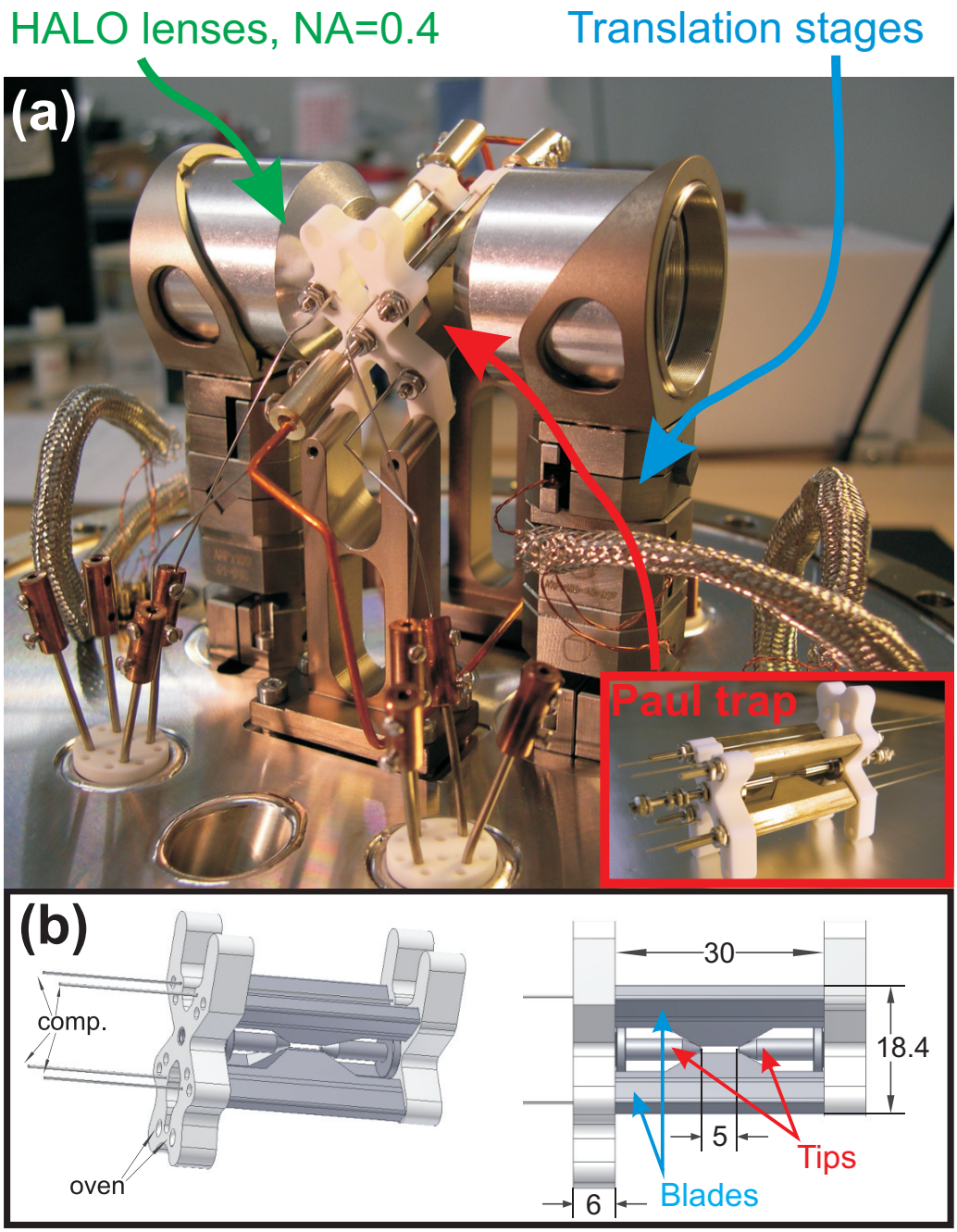

Figure 4.1.: (a) Ion trap picture (b) drawing of trap geometry

electrodes displaced symmetrically along the longitudinal direction of the trap, and two end tip electrodes, appearing as two needles placed in the trap axis at each end (Figure 4.1). The two blade electrodes opposing each other located at

$(x, y, z) = (0, \pm r_0, 0)$ are connected to ground, while the other two, located at $(\pm r_0, 0, 0)$ are connected to a radio-frequency high voltage, oscillating at frequency Ω_{rf} with a peak voltage V_{rf}. The end tips, located at $(0, 0, \pm d_0)$ are biased with a constant voltage V_{et} which is higher than the average rf voltage. This arrangement generates a potential $U(x, y, z) = U_r(x, y) + U_t(z, y, z)$, composed of a radial component, which close to the center of the trap can be approximated as

$$U_r(x, y) = \frac{V_{rf}}{2r_0^2} \sin(\Omega_{rf} t) \left(r_0^2 + x^2 - y^2\right), \tag{4.1.2}$$

and an axial component

$$U_a(x, y, z) = \left(\frac{V_{et}\alpha'}{2d_0^2}\right) \left(2z^2 - x^2 - y^2\right). \tag{4.1.3}$$

The resulting equations of motion, $m\ddot{r_i}(t) = -e\frac{\partial U}{\partial r_i}$, can then be cast in terms of the so called *Mathieu equation*

$$\frac{d^2 r_i}{dt^2} + [a_i - 2q_i \cos(\Omega_{rf})] \frac{\Omega_{rf}^2}{4} r_i = 0 \tag{4.1.4}$$

with

$$a_x = a_y = -\frac{1}{2}a_z = -\frac{4e\alpha' V_{et}}{md_0^2\Omega_{rf}^2}, \qquad q_y = -q_x = \frac{2eV_{rf}}{mr_0^2\Omega_{rf}^2}, q_z = 0. \tag{4.1.5}$$

If the oscillation frequency Ω_{rf} is fast enough so that the field seen by the particle is almost constant during its oscillation, then Equation 4.1.4 can be averaged over one oscillation period to give

$$m\ddot{\bar{r}}_i = -\partial_{r_i} U_{pm}(\bar{\mathbf{r}}) \tag{4.1.6}$$

where $\bar{r}_i$ denotes the position of the particle averaged over one period and U_{pm} is the ponderomotive potential given by equation 4.1.1.

A novel feature of our setup is the presence of two lenses placed at opposite sides of the trap inside the vacuum chamber (see Figure 4.1). They consist of custom-designed high numerical aperture laser objectives (HALO) with a numerical aperture NA = 0.4 and a focal length of 25 mm. Each of them can collect about 4% of the solid angle. The objectives consist of 4 anti-reflection coated lenses and is designed to be diffraction limited. The HALOs are both used to efficiently collect the fluorescence light emitted by a single ion or several ions and to tightly focus a light beam onto the ion to enhance its interaction efficiency. Each HALO is mounted on a set of translation stages (Attocube xyz-positioner, ANPxyz 100) allowing control over the lateral, vertical and longitudinal positions of the HALOs.

4.2. Ion trap setup

Figure 4.2 shows a detailed view of the optical setup around the ion trap configured for experiments combined with the entangled photon source. The ultra-high vacuum (UHV) vessel containing the ion trap is shown on the right. Eight viewports

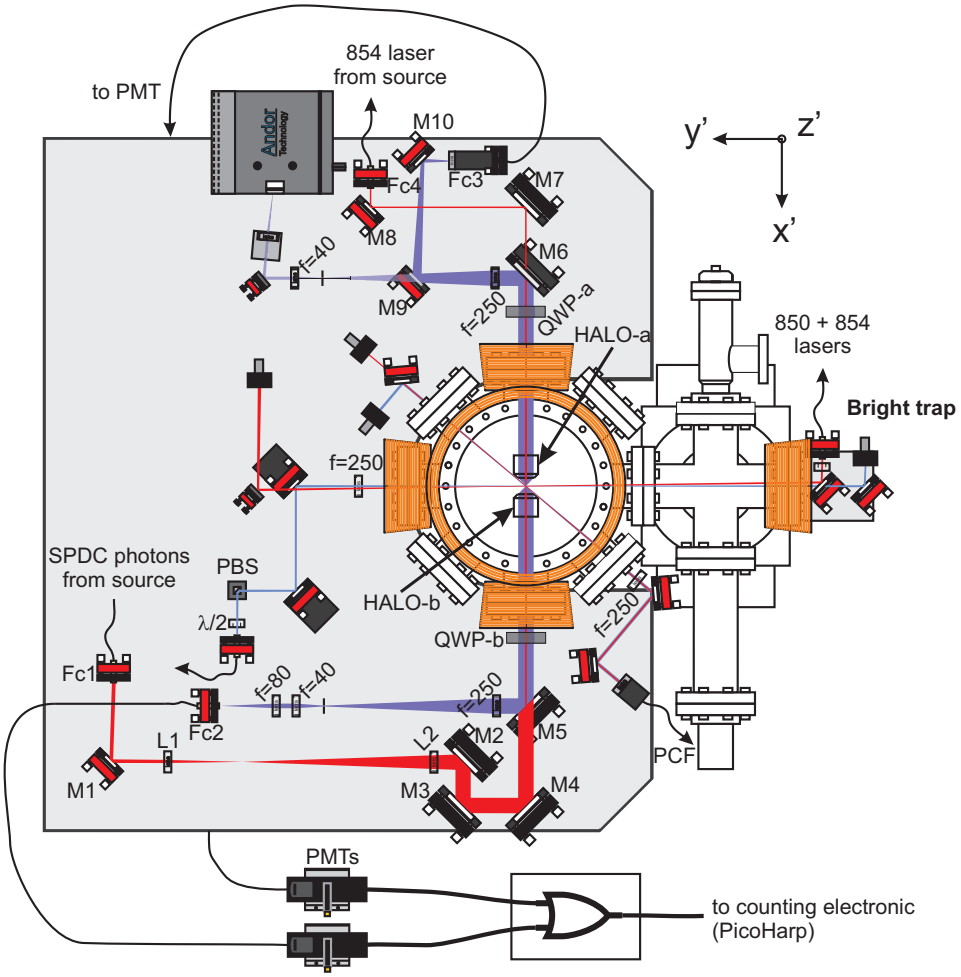

Figure 4.2.: Schematic drawing of the ion trap table, showing all relevant optical components. Only one ion trap is shown for simplicity, although another trap is present in the lab in the left part of the table.

in the horizontal plane, together with two more viewports in the top and bottom and additional small viewports in the diagonals allow for a wide optical access to the trap. The orange cylinders are magnetic field biasing coils and are present in all three dimensions, enabling full control over the magnetic field experienced by the ion. The quantization axis is usually set along the HALO direction, by biasing the coils along that direction and using the other set of coils to compensate stray magnetic fields (see Figure 4.2).

The photons arrive from the SPDC source to the ion through a single mode fiber terminated by fiber coupler Fc1. A telescope consisting of lenses L1 and L2 expands the beam to a full diameter of 10 mm. Mirrors M2-M4 mounted on high precision kinematic holders allow for precise alignment of the SPDC photon beam onto the ion, through HALO-b.

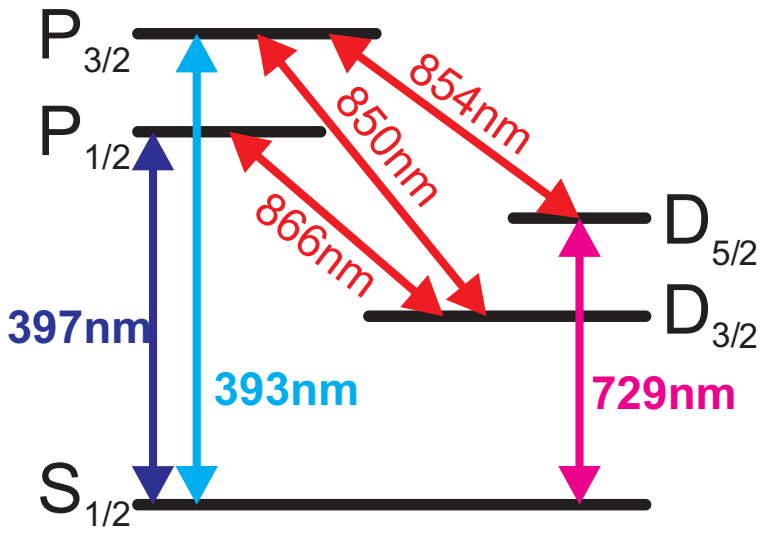

Figure 4.3.: $^{40}Ca^{+}$ level scheme.

The lateral viewports are used to couple the 850, 854 and 397 nm lasers to the ion. After traversing the trap, they are each coupled to individual photo-diodes, allowing for intensity stabilization by feeding back the corresponding error signal to the AOMs controlling each laser beam (see following section). The 854 $\sigma^{+/-}$ polarized laser, which will be employed to optically pump the ion into specified Zeeman sub-levels (see section 7.3, is sent through HALO-a since it must propagate along the magnetic field direction.

4.3. The $^{40}Ca^{+}$ ion

The ion trap setup is designed to trap $^{40}Ca^{+}$. Its energy level scheme is shown in Figure 4.3. A more detailed scheme, including Zeeman splitting is illustrated in Figure 5.1. The levels shown include the ground state $S_{1/2}$, the two first unstable excited states $P_{1/2}$ and $P_{3/2}$ with lifetimes of ~7 ns, and two metastable states $D_{3/2}$ and $D_{5/2}$ with lifetimes of 1.2 seconds.

4.4. Laser system

To address the different transitions in $^{40}Ca^{+}$ (see Figure 5.1) and control the internal state of the ion, lasers at wavelengths of 397, 729, 850, 854, 866 nm are necessary. The lasers must be frequency stabilized well below the atomic transition linewidth, and frequency drifts must be avoided.

The ion is Doppler cooled by means of the 397 nm laser, slightly red detuned below the $S_{1/2} \leftrightarrow P_{3/2}$ transition. As the ion can decay to the metastable $D_{3/2}$ state,

an 866 nm *repumper* laser must also be used to avoid optical pumping to this level.

In our lab, all these lasers are extended cavity diode lasers in the Littrow configuration, like the 850/854 nm master laser of the SPDC source, described in section 3.1. All lasers except the one at 729 nm are stabilized to a Cesium atomic reference at 852 nm by means of a transfer lock using Fabry-Perot cavities of moderate finesse (~ 1000), as explained in section 3.1. This locking scheme provides a typical short and long term frequency stability of ~ 130 kHz for each laser, which is far below the typical transition linewidth of 22MHz (see reference [46] for details). The 729 nm laser addressing the dipole forbidden $S_{1/2} - D_{5/2}$ transition is used to perform coherent manipulations of the optical qubit composed of those two states, and to perform state detection. Since the transition is dipole forbidden, having a linewidth of 0.13 Hz, one wishes that the 729 nm laser be stabilized to the smallest possible bandwidth, much below the 130 kHz of the other lasers. For this purpose, the stabilization scheme with transfer cavities is not viable. Typically it is stabilized to an extremely high-finesse and low thermal expansion cavity. The measurements presented in this thesis did not require the use of the 729 nm laser. However, in schemes where the photonic entanglement is transferred to the atomic states, the stabilization of the 729 laser is required, and its stabilization has been set up during the writing of this thesis.

4.5. Trapping calcium ions

To trap calcium ions, a beam of neutral calcium atoms must be sent through the trap and some atoms must be ionized.

The ion trap is equipped with two tubes containing metallic Calcium granules connected to a resistive heater. By applying a current of around 4-6 A, the calcium sample is heated to about 300-400$^\circ C$. The tubes have an orifice at one end and are oriented towards the trap center, thereby directing the Calcium beam to it [61].

To ionize calcium atoms a photoionization scheme, described in detail in [61], is implemented. The setup works in a two-step process by which one electron in a neutral Calcium atom is excited by a 423 nm laser to the $^1\mathrm{P}_1$ level, and finally to the continuum by an LED, centered around 390 nm. The LED and the oven are controllable through buttons in a LabVIEW program, and can be switched on and off at any desirable time.

Once ionized, the atom is trapped and laser cooled as mentioned above. The ion then scatters a continuous flux of 397 nm fluorescence photons. These are collected by the HALOs and directed either to photo-multiplier tubes (PMTs)[1] or to a single-photon sensitive EMCCD-camera (Electron Multiplying Charge Coupled Device) from Andor Technology. The presence of a single ion is signaled by the appearance of a round spot on the camera image. Strings of more than one ion can also be created, appearing as a stable sequence of aligned spots. To control the

[1] Initially, two Hamamatsu H7360-02 PMTs were used. Although the specified photon detection efficiency at 400 nm was around 20%, they turned out to be less efficient. Later, two Hamamatsu H7422P-40SEL were bought, with a specified photon detection efficiency of 28% at 400 nm.

Figure 4.4.: Pictures of a single and strings of several ions visualized with the EMCCD camera. The inclination is due to the corresponding tilt of the trap with respect to the horizontal.

amount of ions that are loaded, it is usually necessary to work at a low oven current (around 4 A) and quickly switch off the LED when the desired number of ions appears on the camera. With this method, it is possible to trap a selected number of atoms. EMCCD-camera pictures of different numbers of ions in the trap are shown in Figure 4.4.

4.6. Experimental setup coupling the source to the ion trap

Due to space constraints, the source and the ion traps were constructed in separate labs. From the practical point of view, this was somewhat inconvenient, since operating both experiments at the same time, especially when done by a single person, required often commutation between the two rooms. From the technical point of view, the situation was not so dramatic, although some important issues had to be taken into account.

As explained in chapter 3, both arms of the source are fiber coupled. This is usually done with 2 meter long single-mode (SM) fibers. In the first experiments coupling the source and the ions, polarization-maintaining (PM) fibers were used in both arms. The photon pairs were split in the source by a PBS, and each photon is coupled into its corresponding fiber ensuring that their polarization was aligned

with the fiber polarization axis. To direct the source photons to the ions, a long 15 meter fiber of the same type was used. The two fibers were connected together using a standard fiber-to-fiber coupler. Although this introduced some insertion losses (typically measured to be around 15%), it turned out to be very convenient. Mainly, it allowed to decouple the source from the ion system whenever necessary. In this way, the two setups could be aligned separately, and then combined together.

In more advanced experiments, where photons from a polarization entangled pair must reach the ion, a non-polarization-maintaining SM fiber must be used. Such a fiber was installed between the two labs. It was inserted through a plastic flexible tube connecting the two labs and conveniently fixed to minimize polarization fluctuations due to temperature drifts and mechanical stress.

To characterize the polarization stability of the fiber, we coupled in a linearly polarized laser beam and measured the output polarization with a polarimeter (Thorlabs PAX5710). The observed variation of the horizontal projection of the polarization during one hour is shown in Figure 4.5. A variation of less than 0.5% proves the stability of the system.

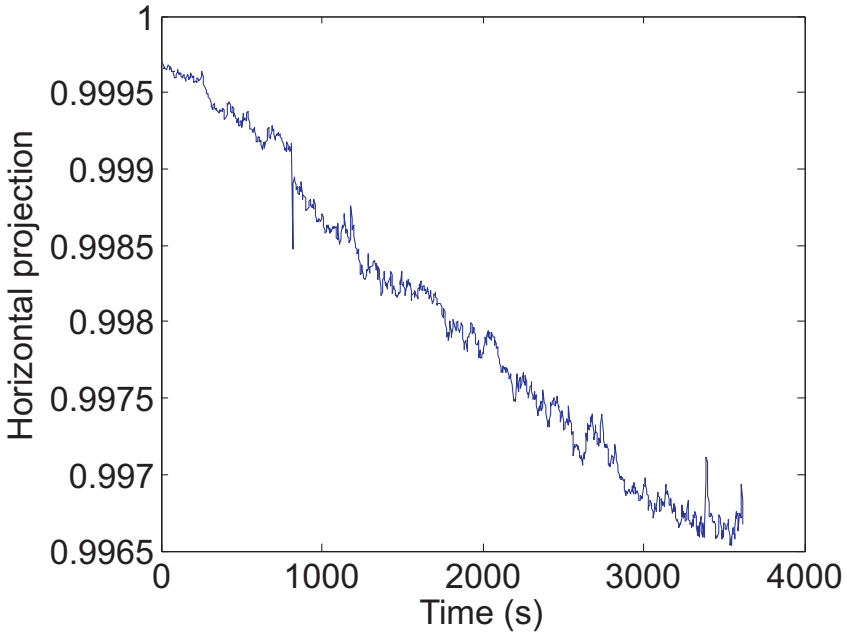

Figure 4.5.: Variation of the horizontal projection of the fiber output polarization in 1 hour.

5. Detecting single-photon single-atom interaction

This chapter will first offer a brief discussion of some possible schemes to detect the interaction of single photons with single $^{40}Ca^{+}$ ions. The efficiencies of the different schemes will be estimated and their usefulness for quantum information processing will be assessed. A technique which was developed in this thesis to experimentally detect the instant of a photon absorption will also be discussed. This method involves some parameters which will determine the probability of detecting the events and the uncertainty in the determination of the interaction time. The optimization of these parameters will be discussed.

5.1. Level scheme of $^{40}Ca^{+}$

Our setup is designed to trap single $^{40}Ca^{+}$ ions. The level structure of this species is presented in Figure 5.1. It has no nuclear spin and therefore no hyperfine splitting. For quantum information processing purposes two types of qubits are usually chosen: an optical qubit formed by one magnetic sublevel of $S_{1/2}$ and one sublevel of $D_{5/2}$, or an RF-qubit formed by the two sublevels of $S_{1/2}$.

The interaction with down-conversion photons is realized through an electric dipole or *allowed* transition. Such transitions arise from the interaction of the the electric dipole moment of the atom $\mathbf{D}$ with the electric field of the photon $\mathbf{E_0}$. The interaction hamiltonian can be written as

$$\mathcal{H}_I = e\mathbf{D} \cdot \mathbf{E_0} \cos(\omega t). \tag{5.1.1}$$

Other contributions to the hamiltonian, due to the interaction with the magnetic field and of higher order in the electric field, can be shown to be much smaller than 5.1.1.

In a semiclassical approach, the total hamiltonian is obtained by summing expression 5.1.1 to the atomic hamiltonian, whose eigenvalues are the atomic levels represented in Figure 5.1:

$$\mathcal{H} = \mathcal{H}_A + \mathcal{H}_I \tag{5.1.2}$$

To obtain the transition rates, one must apply time dependent perturbation theory, treating term 5.1.1 as the perturbation. For light resonant with a transition between two levels $|a\rangle$ and $|b\rangle$ and for a hydrogen-like atom, the transition amplitude is proportional to $\epsilon \cdot \mathbf{r}_{ab}$, where

$$\mathbf{r}_{ab} = \langle a| \mathbf{r} |b\rangle \tag{5.1.3}$$

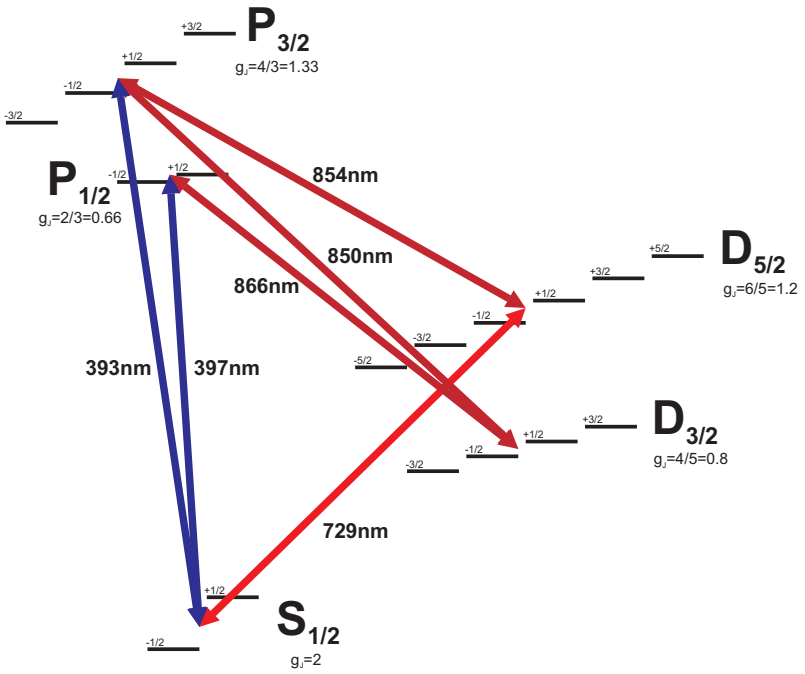

Figure 5.1.: $^{40}Ca^{+}$ level scheme, shown with Zeeman sublevels. The Landé g-factors of each level, governing the strength of the Zeeman splitting, are shown.

and ϵ is the polarization of the electric field; $\mathbf{r}$ is the position vector of the valence electron. The two eigenstates $|a\rangle \equiv \left|n^a, l^a, j^a, m_j^a\right\rangle$ and $|b\rangle \equiv \left|n^b, l^b, j^b, m_j^b\right\rangle$ are fully characterized by the four quantum numbers n, l, j, m_j. In our experiment, the transitions of interest are between states $|nL_J, m_J\rangle = \left|6D_{5/2}, m_J\right\rangle$ or $\left|6D_{3/2}, m_J\right\rangle$ and $\left|6P_{3/2}, m_J\right\rangle$. Thus, in virtue of the Wigner-Eckart theorem, the matrix element 5.1.3 is proportional to a factor (reduced matrix element) characterizing the overall strength of the particular transition and to the Clebsch-Gordan coefficients $\left\langle j^a, m_j^a, k=1, \Delta m \middle| j^b, m_j^b \right\rangle$, where k=1 is the rank of the tensor operator $\mathbf{r}$, and Δm is its spherical component. Values of these coefficients are listed in Figure 5.2.

5.2. Schemes of atom-photon interaction in $^{40}Ca^{+}$

In the following we consider different schemes to detect the interaction of 850 and 854 nm photons with a single $^{40}Ca^{+}$, through the $D_{3/2} \leftrightarrow P_{3/2}$ and $D_{5/2} \leftrightarrow P_{3/2}$ transitions, respectively. For the sake of simplicity, we will not consider the Zeeman structure of each level, for the moment. This will be treated in a later section, where polarization state transfer from photons to atoms is considered.

Four different interaction schemes are depicted in Figure 5.3. In (a), the 397 cooling laser and the 866 repumping laser are continuously switched on, so the ion emits a continuous flux of 397 nm fluorescence photons when decaying from $P_{1/2}$

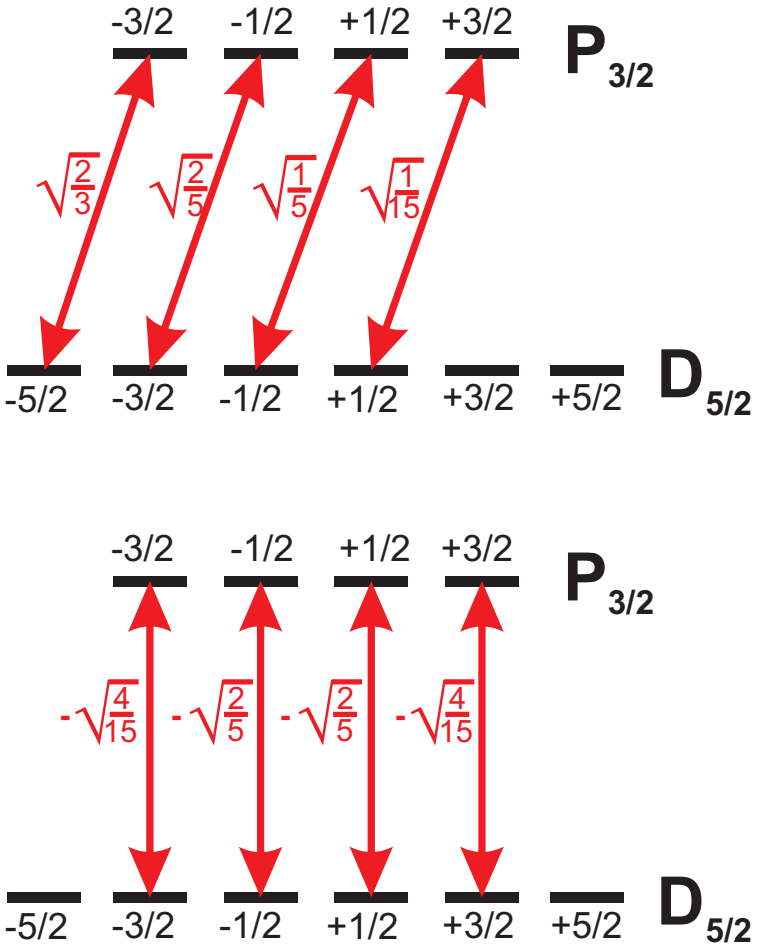

Figure 5.2.: Clebsch-Gordan coefficients of the $D_{5/2} \leftrightarrow P_{3/2}$ transition for Δm = 1 (top) and Δm = 0 (bottom). Δm = -1 transitions have identical coefficients to their corresponding symmetric Δm = 1 transitions.

to $S_{1/2}$. These photons are monitored with a photodetector. Since some of the population is in the $D_{3/2}$ level, the ion can additionally absorb 850 nm SPDC photons from the source. An 850 nm photon absorption excites the ion to $P_{3/2}$, from where it can decay to $S_{1/2}$, $D_{5/2}$ or back to $D_{3/2}$. The decay to the $D_{5/2}$ metastable state leaves the ion uncoupled to any other level by the present lasers, so the emission of fluorescence ceases. This effect, known as a quantum jumps, is in general used to measure the state of the ion $S_{1/2}$-$D_{5/2}$ ion qubit in quantum information processing implementations with trapped ions. In this case, the quantum jump signals the absorption of an 850 nm photon from the SPDC source.

Case (b) is a similar implementation of case (a) using the $D_{5/2} \leftrightarrow P_{3/2}$ transition. This case will be discussed in more detail below.

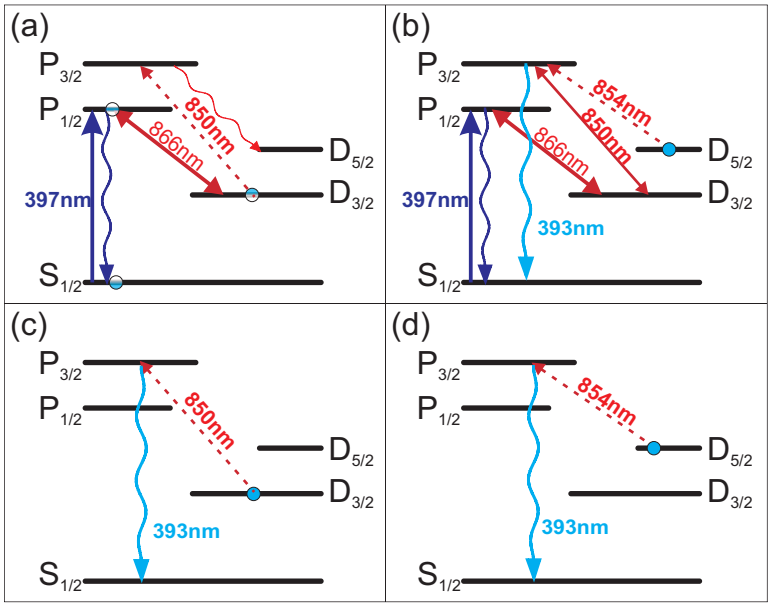

Figure 5.3.: Four different schemes to detect the interaction of single SPDC photons with single $^{40}Ca^{+}$ ions. In (a) and (c), the source is tuned to 850 nm, while in (b) and (d) it is tuned to 854 nm. See text for details.

In cases (c) and (d), the effect signaling the SPDC photon absorption is now the detection of the single 393 nm photon which is emitted when the ion decays from $P_{3/2}$ to $S_{1/2}$. For this, the 397 and 866 nm lasers are switched off. As will be shown below, these schemes allow transferring the polarization state of the SPDC photon to the internal state of the ion, in particular, to the Zeeman substates of the $S_{1/2}$ manifold.

In this thesis, schemes (a) and (b) were implemented experimentally. Scheme (a) led to the first proof of absorption of SPDC photons by a single ion, while scheme (b) allowed to observe more interesting features, such as the correlation of the absorption event with the detection of the twin photon. The results of the first experiments realized with scheme (a) are reported in more detail in [61], and will be briefly summarized in section 7.1. The experiments with scheme (b) led to the main results of this thesis, so this scheme will be described in full detail below.

The scheme is illustrated in Figure 5.4. The 397 and 866 nm lasers illuminate the ion continuously. In a first step, panel (a), the ion is cooled by the 397 nm laser, together with the 866 nm repumper. Later, in panel (b), the ion is prepared in the metastable $D_{5/2}$ state by optical pumping with an 850 nm laser. Finally, in (c), the ion may absorb an 854 nm SPDC photon and decay into $S_{1/2}$, thus reentering the cooling cycle and restarting the emission of fluorescence. This onset of fluorescence is what signals the absorption of an SPDC photon in this case. Note that the ion can also decay spontaneously from $D_{5/2}$ to $S_{1/2}$, with the same revival of fluorescence emission. Therefore, an 854 nm photon absorption and a spontaneous decay event

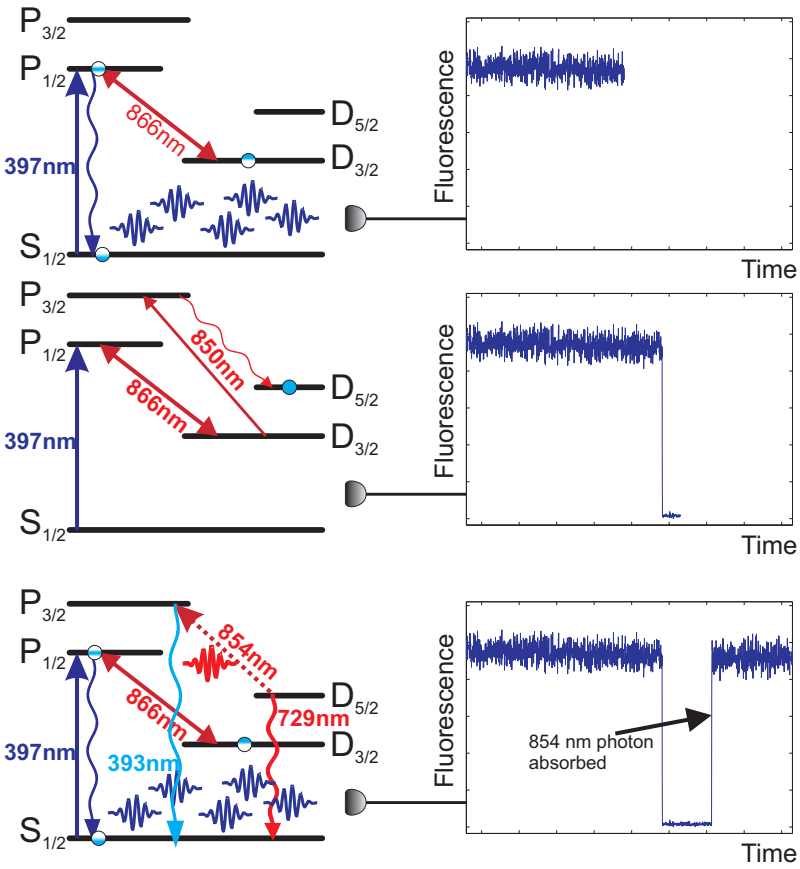

Figure 5.4.: A detailed description of scheme (b) in Figure 5.3.

cannot be distinguished in this scheme.

There are two possibilities for implementing this scheme: continuous excitation or pulsed excitation. In a continuous experiment all lasers are left on indefinitely. The three phases (a), (b) and (c) take place in a random succession. In this case, the 850 nm laser must be highly attenuated, such that the rate of excitation to the $D_{5/2}$ is similar to the rate of absorption of 854 nm SPDC photons. This must be so to ensure that after an 854 nm photon absorption, the ion will emit a long enough stream of fluorescence photons such that at least one of them is detected with certainty. On the other hand, if a pulsed sequence is used, the three phases are deterministically divided in time. In such case, in phase (b) a strong 850 nm laser pulse is sent during a short time interval, thus pumping the ion deterministically to the $D_{5/2}$ state. A pulsed scheme is more convenient to maximize the amount of time the ion spends in the $D_{5/2}$ state waiting for a SPDC photon absorption, as will become apparent in Chapter 7.

Although not considered up to now, the Zeeman structure of the $^{40}Ca^{+}$ atomic level scheme is important in various aspects. For example, preparing the ion in a specific magnetic substate leads to an increase in the interaction efficiency with the SPDC photons. This can be done by optically pumping the ion to the outermost

substates of $D_{5/2}$, $m = \pm 5/2$, using 854 nm $\sigma^{+/-}$ polarized light effectively polarizing the ion, such that its magnetic moment gets aligned with the external magnetic field. The resulting transition dipole moment between this state and the excited $P_{3/2}, m = 3/2$ state has the highest value out of all $D_{5/2} \leftrightarrow P_{3/2}$ transitions, as is deduced from the values of Clebsch-Gordan coefficients in Figure 5.2.

More importantly, the Zeeman structure can be harnessed to develop schemes to map the polarization state of a photon to the Zeeman substates of the ion, as will be explained in section 8.1.

5.3. Detecting the photon absorption event

One important issue for the implementation of schemes (a) and (b) in Figure 5.4 is how to extract from the fluorescence detection data the photon absorption times. This problem is considered in some detail in this section.

In these schemes a photon absorption event is signaled by a start or stop in the detection of the flux of fluorescence photons emitted by the ion (a quantum jump). It is then necessary to extract the times when this sudden change in the fluorescence rate happens.

A typical data file, obtained with our counting electronics (PicoHarp), consists of a list of 64 bit values representing the time, in units of 4 ps, of each detection (or click) of a fluorescence photon. From these lists, the photon absorption event must be extracted. We developed two methods to do this.

5.3.1. Method 1

In the first method, a time trace of the fluorescence rate is obtained. This is done by dividing the time axis in small intervals (bins) of size δt and counting the number of clicks in each bin. By plotting a histogram of the distribution of counts per bin throughout the whole file, a threshold number of counts c_{th} dividing the on and off states is defined (see e.g. Figure 7.8). This threshold is usually defined as the point between the two peaks in the histogram where the frequency reaches its minimum. Next, the fluorescence trace is filtered using a moving average. Let $c_n = c(n\delta t)$ be the number of fluorescence counts detected in bin n, between times $n\delta t$ and $(n+1)\delta t$. The filtered trace is given by

$$\overline{c_n} = \frac{1}{2M+1} \sum_{m=n-M}^{n+M} c_m \tag{5.3.1}$$

The filtered fluorescence trace is then scanned, searching for the bin n in which the count rate decreases below the threshold in scheme (a), or increases above the threshold in scheme (b):

$$\overline{c_n} < c_{th}, \tag{5.3.2a}$$

$$\overline{c_n} > c_{th}. \tag{5.3.2b}$$

The time of absorption of an SPDC photon is then given by $t_n^{abs} = n\delta t$, and is obtained with a precision of δt.

This method has two main drawbacks: 1) The resulting time of absorption may have a finite delay with respect to the real absorption event, due to the arbitrariness in the definition of the threshold. 2) Fluctuations in the fluorescence rate when the ion is on lead to fluctuations in the absorption time. If the fluorescence rate drifts significantly during the data acquisition time, the detected absorption time will drift accordingly with respect to the real absorption event time.

5.3.2. Method 2

The limitations in the last method can be overcome by complementing it with a second procedure. First, method 1 is used to predetect the quantum jump events. Instead of taking the time $t_n^{abs} = n\delta t$ at which one of expressions 5.3.2 holds as the quantum jump time, we first extract the set of clicks t_m contained in some interval $(t_n^{abs} - T/2, t_n^{abs} + T/2)$ around t_n^{abs} and perform an additional analysis with them:

- The delays $\Delta t_m = t_m - t_{m-1}$ between each pair of successive detection times t_m are obtained.
- A threshold delay τ_{th} is appropriately defined as will be shown below.
- Then, when

$$\Delta t_{m+1} > \tau_{th} \text{ and } \Delta t_m < \tau_{th}, \tag{5.3.3}$$

  the fluorescence emission must have ceased in the time interval (t_m, t_{m+1}). Similarly, if

$$\Delta t_{m+1} < \tau_{th} \text{ and } \Delta t_m > \tau_{th}, \tag{5.3.4}$$

  the fluorescence emission is likely to have restarted in (t_m, t_{m+1}).

The efficiency of this method depends strongly on the value of the delay threshold τ_{th}, which must be optimized. To this end, let's consider a set of three successive clicks, t_1, t_2 and t_3, which define two delays $\Delta t_1 = t_2 - t_1, \Delta t_2 = t_3 - t_2$. Four cases must be considered, depending on the state of the ion during each time delay:

- Case 1: Ion is on in both delays
- Case 2: Ion is off in both delays
- Case 3: Ion is on during the first delay and off during the second delay
- Case 4: Ion is off during the first delay and on during the second delay

Cases 3 and 4 are the cases we want to detect. We now assume that the time of fluorescence clicks, detected when the ion is on, follows a Poisson distribution. This is a reasonable assumption for long enough time delays, for which the quantum properties of the light emitted by the ion are negligible, and the detection of one fluorescence photon becomes completely independent of the detection of the previous photon. Under this assumption, the probability of detecting two fluorescence photons separated by a time $(t, t + dt)$ is given by

$$p_{on}(t)dt = \frac{1}{\tau_{on}} \exp\left(-\frac{t}{\tau_{on}}\right) dt, \tag{5.3.5}$$

where $\tau_{on} = 1/R_{on}$ is the inverse of the rate of detected photons when the ion is on. Similarly, assuming that the background clicks that are detected when the ion is off are poissonian-distributed, we can write

$$p_{off}(t)dt = \frac{1}{\tau_{off}} \exp\left(-\frac{t}{\tau_{off}}\right) dt \tag{5.3.6}$$

as the probability for detecting two background clicks within $(t, t+dt)$. Here, $\tau_{off} = 1/R_{off}$, where R_{off} is the rate of background clicks.

To evaluate the efficiency of this detection method, it is necessary to calculate the probability that, if the state of the ion during the two delays Δt_1 and Δt_2 is in any of the four cases mentioned above, we would actually detect it.

For example, in order to detect that the ion undergoes a quantum jump from on to off (case 3), or from off to on (case 4), the method looks for an event where conditions 5.3.3 or 5.3.4 hold. The probability of this event is given by

$$\begin{aligned} p_{on-off}(\tau_{th}) &= \int_0^{\tau_{th}} p_{on}(t)dt \int_{\tau_{th}}^{\infty} p_{off}(t)dt \\ &= \exp\left(-\frac{\tau_{th}}{\tau_{off}}\right)\left[1 - \exp\left(-\frac{\tau_{th}}{\tau_{on}}\right)\right]. \end{aligned} \tag{5.3.7}$$

This probability can be interpreted as the efficiency of detecting a photon absorption event at the moment when it happens, using this method.

The method can also erroneously identify quantum jump events. This happens if the ion is in the on or in the off state during both delays (cases 1 and 2), but by chance conditions 5.3.3 or 5.3.4 hold. The probability for each of these false events are given by

$$\begin{aligned} p_{on-on}(\tau_{th}) &= \int_0^{\tau_{th}} p_{on}(t)dt \int_{\tau_{th}}^{\infty} p_{on}(t)dt \\ &= \exp\left(-\frac{\tau_{th}}{\tau_{on}}\right)\left[1 - \exp\left(-\frac{\tau_{th}}{\tau_{on}}\right)\right], \end{aligned} \tag{5.3.8}$$

if the ion is on (case 1), and

$$\begin{aligned} p_{off-off}(\tau_{th}) &= \int_0^{\tau_{th}} p_{off}(t)dt \int_{\tau_{th}}^{\infty} p_{off}(t)dt \\ &= \exp\left(-\frac{\tau_{th}}{\tau_{off}}\right)\left[1 - \exp\left(-\frac{\tau_{th}}{\tau_{off}}\right)\right], \end{aligned} \tag{5.3.9}$$

if the ion is off (case 2).

The dependence of these probabilities with the delay threshold τ_{th} are plotted in Figure 5.5 for a typical situation in our experiments, with $R_{on} = 5 \times 10^5$ counts/s, and $R_{off} = 10^3$counts/s. The optimum delay threshold[1] in this case is $\tau_{th} = 12.4\mu$s and yields a probability of 98.5% of detecting the quantum jump event. For this

[1]for which the probability of detecting a quantum jump event is maximum

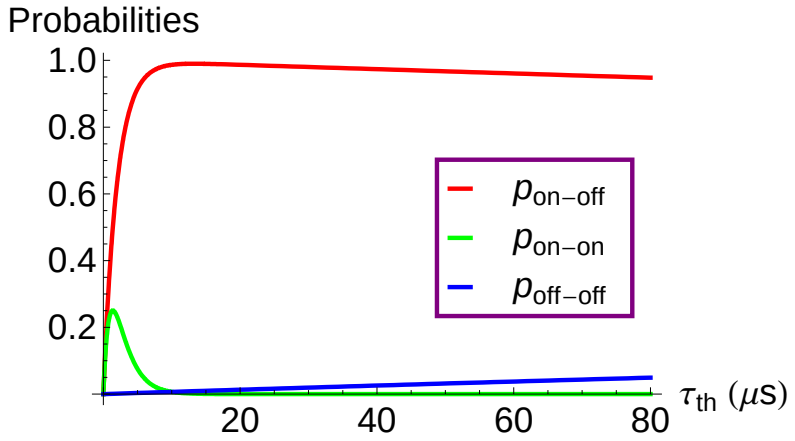

Figure 5.5.: Dependence on the delay threshold τ_{th} of the probability of detecting a real quantum jump event (red), of detecting a false quantum jump event when the ion is on (green) and when it is off (blue).

optimum value of τ_{th} regarding detection efficiency, the probability of erroneously identifying a quantum jump when the ion is on is given by $p_{on-on} = 0.2\%$, and when it is off $p_{off-off} = 1.2\%$.

At this point it becomes clear why it is necessary to preselect, using method 1, the clicks around the quantum jump event, before searching for the absorption event using the delay threshold method. If no preselection is performed, many false quantum jumps will be detected. However, if a few clicks (e.g. 20) are selected around the quantum jump event, the probability of a false quantum jump will be negligible.

Moreover, this problem can be completely avoided by adding additional conditions in the detection of the quantum jump event. For example, condition 5.3.4 can be extended to

$$\Delta t_{n+1}, t_{n+2} < \tau_{th} \text{ and } \Delta t_n, t_{n-1} > \tau_{th}, \tag{5.3.10}$$

and an analogous extension can be performed on condition 5.3.3. The quantum jump detection probability is now the square of expression 5.3.7, and erroneous quantum jump probabilities in the off and on state are the square of 5.3.9 and 5.3.8, respectively. The resulting probability of erroneously identifying quantum jump events is negligible when a small number (<100) of preselected clicks are used.

In Figure 5.6 we calculate, using condition 5.3.4, the optimum delay threshold and the corresponding detection probability for any combination of rates R_{on} and R_{off} typically observed in our experiments.

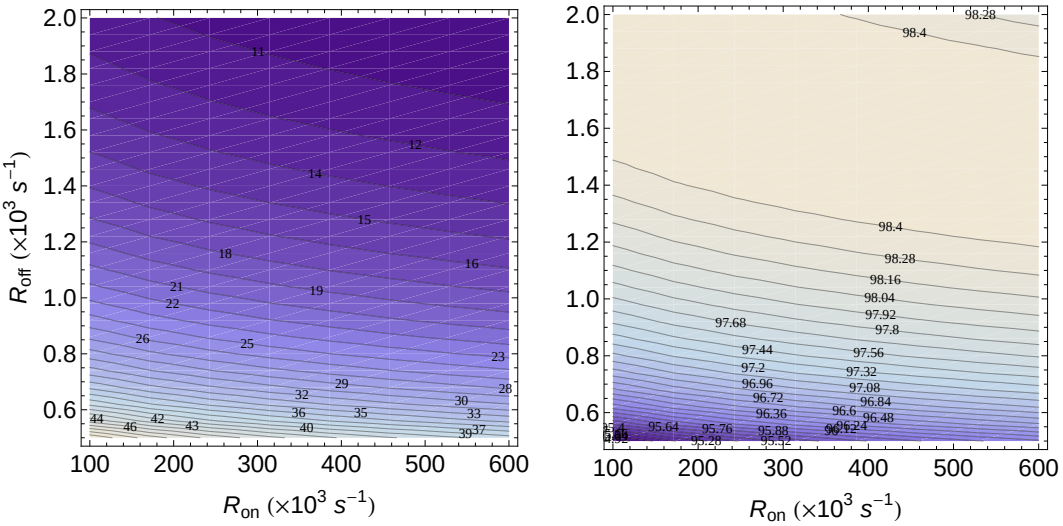

Figure 5.6.: Optimum delay threshold in μs (left) and the corresponding detection probability (right) as a function of the detected fluorescence rate when the ion is on R_{on} and the background rate when the ion is off R_{off}.

5.3.3. Detection time resolution

We now tackle the problem of determining the time resolution of detecting a single photon absorption event by means of method 2, described in the last section. We will assume that the first (or last) detected fluorescence photon signaling the absorption of an SPDC photon was successfully extracted from the data.

Consider a single atom that starts emitting a constant flux of single photons at a rate R at time $t = 0$. This time corresponds to the moment of the SPDC photon absorption event (the quantum jump). We also assume that a single-photon detector is monitoring the ion and has a probability p of detecting a single photon emitted by the latter. The detector will then detect a constant flux of photons at an average rate $r = pR$.

The precision with which the time of the absorption event is determined by the first detection of a photon is defined as the time after the atom starts emitting for which the probability of having detected the first photon is higher than some conventional value, e.g. 95%. We must then obtain an expression for this probability. For this, we first notice that the probability that the n-th emitted photon is the first to be detected is given by $P_n = (1-p)^{n-1} \times p$, that is, the probability of not detecting the first $n-1$ photons times the probability of detecting the n-th emitted photon. Here, n is the average number of emitted photons after a time t, given by $n = Rt$. Additionally, the probability that the ion emits a photon in a small time interval (t, t+dt) is given by $dn = Rdt$. Hence, the probability of detecting a photon in this

same time interval is given by $P_n dn$, which can be written as

$$\begin{aligned} P_n dn &= (1-p)^{n-1} pRdt \\ &= \left(1 - \frac{r}{R}\right)^{Rt-1} rdt \\ &= \exp\left[Rt \log\left(1 - \frac{r}{R}\right)\right] \frac{r}{1 - r/R} dt \end{aligned}$$

which, for $R >> r$ ($\log(1 - r/R) \simeq -r/R$), becomes

$$P(t)dt = \exp(-rt)\, rdt.$$

We have defined $P(t)dt$ to be the probability of detecting the first photon in the time interval (t,t+dt). The condition $r << R$ implies that $p << 1$, and it does hold in our experiment where we typically have $p \approx 10^{-2}$.

Finally, the probability of detecting the first photon before a time t_f is given by

$$\int_0^{t_f} P(t)dt = 1 - \exp(-rt_f) \tag{5.3.11}$$

which takes the value of 0.95 at $t_f \simeq 3/r$. Thus, the uncertainty of the photon absorption detection time is given by (in the 95% criterion)

$$\delta t = 3/r. \tag{5.3.12}$$

This proves that the fluorescence detection rate completely determines the time resolution with which the photon absorption event can be measured. In our experiment, we achieved a rate of up to 600000 s^{-1}, which results in a $\delta t = 5\mu s$.

In the experiments we will consider, the absorption of single SPDC photons by a single ion is detected with the techniques described above. At the same time, these absorption events are also triggered by the detection of the partner SPDC photon. The triggering event has a time resolution given by the filtered photon wavepacket duration, which turns out to be 7 ns (see Chapter 6). Therefore, the triggering event is much more precise than the photon absorption (quantum jump) event. This will become apparent when the $g^{(2)}$ correlation function between the two events will be obtained.

The $g^{(2)}$ function is easy to model. Assume that the trigger is taken as the start event at time t_1 and the first detected fluorescence photon as the stop event at time t_2. The time distribution of these individual events relative to the actual time of absorption are given by $p_1(t_1) = \exp(-\delta\omega t_1)$ and $p_2(t_2) = \exp(-rt_2)$, respectively, where $\delta\omega = 2\pi \times 22$ MHz $= 1/(7.23\text{ns})$ is the frequency bandwidth of the filtered photon. The $g^{(2)}$ function is then given by

$$\begin{aligned} g^{(2)}(\tau) &= \int_{-\infty}^{\infty} dt_1 \int_{-\infty}^{\infty} dt_2 p_1(t_1) p_2(t_2) \delta[\tau - (t_2 - t_1)] \\ &= (r + \delta\omega) \begin{cases} \exp(-r\tau) & \text{for } \tau \geq 0\,, \\ \exp(\delta\omega\tau) & \text{for } \tau < 0\,. \end{cases} \end{aligned}$$

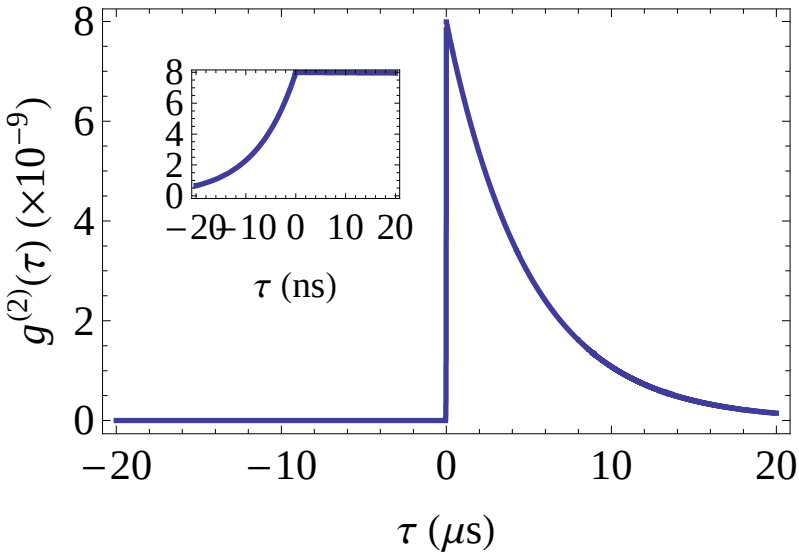

Figure 5.7.: Theoretical model of the $g^{(2)}$ function to expect in the trigger absorption measurement.

This function is plotted in Figure 5.7 for the real experimental parameters already mentioned above. Note the asymmetric shape, owing to the difference in time resolutions of the two events defining the coincidences.

The experimental $g^{(2)}$ is obtained by calculating a histogram of the number of paired detections in both channels as a function of their time delay. For this histogram, a bin size Δt must be defined. It is clear from signal-to-noise considerations that the bin size should be chosen such that all coincident events appear in a single bin. On the other hand, the background due to accidental correlations must be considered. This background can be easily calculated as $R_1 R_2 \Delta t T$, where R_1 and R_2 are the rates of events in each channel and T is the acquisition time. Note that the background level increases with the bin size Δt, so Δt should not be chosen too big. A compromise in terms of signal-to-noise ratio must be established. Typically, $\Delta t = 3/r$, as in Equation 5.3.12, is a good choice.

To analyze the data, we developed a code implementing method 2 in C. The program, named *DetectQuantumJump*, takes an input file of binary 64 bit numbers (obtained from PicoHarp) representing the times of each click, and gives an output file of 64 bit numbers representing the first (or last) click detected after (or before) each quantum jump event. This file, together with the file of trigger clicks, can then be used to calculate a $g^{(2)}$ correlation function, by means of a second C program, *g2calc*.

To test the correct operation of the code, an artificial data set was generated and analyzed with the programs. The data set emulates the measured data, including poissonian noise, but with perfect correlation efficiency. One file consists of a list of clicks with random delays. The delay probability distribution is switched between the ion-on delay distribution 5.3.5 and the ion-off delay distribution 5.3.6.

The switching between the two corresponds to quantum jumps and is also done randomly, with a rate similar to the experimental rate of quantum jumps. Whenever the distribution switches from off to on, a click is saved in a second file which corresponds to the trigger data file. Therefore, 100% correlation efficiency is assumed. By running the code implementing method 2 on this data, its efficiency can be assessed.

All random delays are generated using inverse transform sampling [62]. A uniform random number generator is used to produce a real random number $x \in (0, 1)$. Then the cumulative distribution function (cdf) $F(x) = \int_0^x p(X)dX$ of the desired distribution $p(X)$ is obtained. Finally, the inverse of the cdf is applied to the uniform random number to obtain a random number y with distribution $p(x)$: $y = F^{-1}(x)$. This is simple in the case of the exponential distribution $p(x) = 1/\tau \exp(-x/\tau)$, for which $y = F^{-1}(x) = -\tau \log x$, where τ is the decay constant of the exponential distribution.

6. Characterization of the photon pair source

This chapter gives a full characterization of the relevant properties of the photon pair source. First, the time correlation between the two photons is measured, from which an assessment of the photon bandwidth is obtained. Next, the tunability of the source around the atomic transitions is demonstrated, followed by a measurement of the source brightness. Finally, the polarization entanglement of the photon pairs is characterized.

6.1. Time correlation and frequency bandwidth of photon pairs

To characterize the time correlation between the two paired photons and their bandwidths, we perform a measurement of the second order correlation function $G^{(2)}(\tau)$ between the unfiltered and filtered photons, which was calculated theoretically in section 2.1.3. For this, we coupled both the fiber SMF3 and the filter transmission fiber (MMF) into single photon counting modules (Perkin Elmer SPCM-AQ14/15) (see Figure 3.6. The detection signal from each detector is sent to a time-correlated single-photon counting system (TCSPC, PicoHarp 300 from PicoQuant GmbH), which records a histogram of the time delay between detections in the unfiltered arm and the filtered arm. A typical histogram is shown in Figure 6.1. The date was obtained by integrating over a time of 2900 s. A strong correlation peak indicates the time correlation between the detection of the two photons. The time delay of around 5 ns was introduced electronically by making the cable connecting the detector with the PicoHarp module longer in the second channel. This is necessary since negative time delays are not detectable in the histogram mode of the PicoHarp device.

The shape of the measured histogram coincides with that of the calculated $G^{(2)}(t, t+\tau)$ function, in expression 2.1.32. We then perform a least-square fit of a decaying exponential function $Ae^{-2\pi\delta\nu t}$ to the data set on the right of the step to obtain the filtered bandwidth $\delta\nu = 22.0 \pm 0.5$ MHz, which corresponds to a decay time of $\tau = \frac{1}{2\pi\delta\nu} = 7.25 \pm 0.17$ ns. This value agrees perfectly with the cavity transmission linewidth of 22.5 MHz, measured in Section 3.5.

A simple interpretation of this data is the following. The unfiltered photon, having a broad spectrum of 130 GHz and a narrow time spread of 6.8 ps (see Section 2.1.3), is a precise reference for the time of creation of each photon pair. The partner photon is delayed in the filtering cavities, bouncing repeatedly between the cavity mirrors, for an average time $\tau = 7.25ns$. The exponential decay is due to the fact

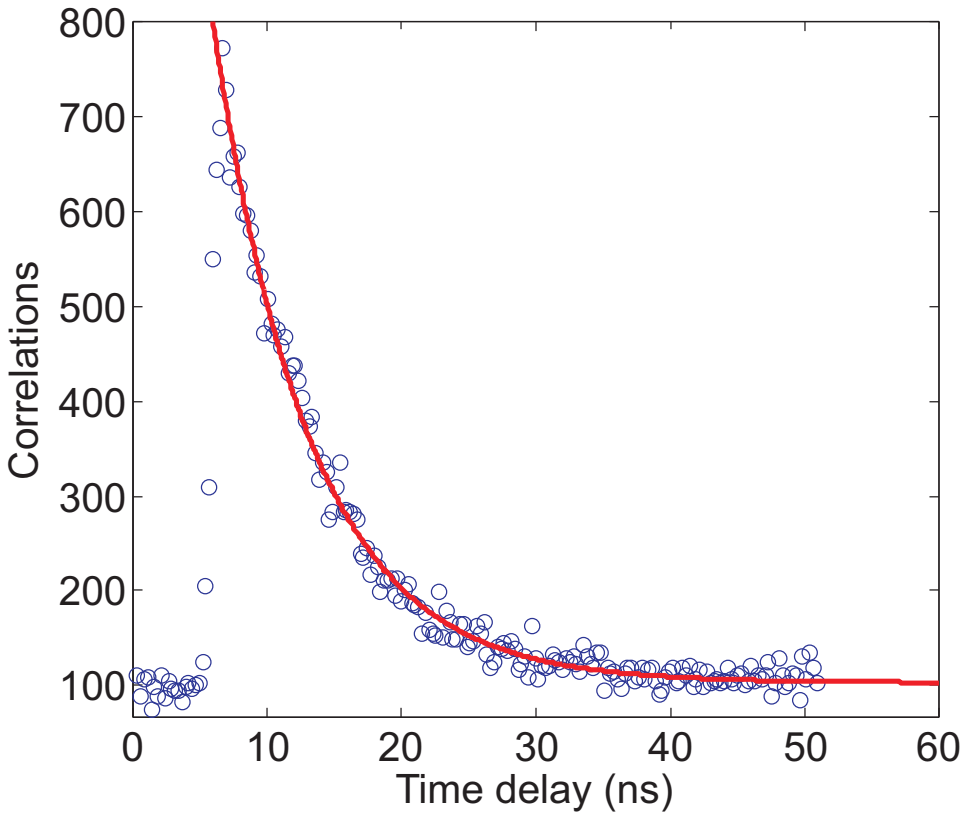

Figure 6.1.: Time correlation measurement of the photon pairs. The horizontal axis is the time delay between a detection of an unfiltered photon and the subsequent detection of a filtered photon. The vertical axis is the number of paired detections. Each time bin is 256 ps wide. The exponential decay is the ring down of the photon in the narrowband cavity. The integration time was 2900 s.

that the probability that the photon was transmitted through the cavity mirrors at the n-th round-trip decays exponentially with n. The time of the n-th round-trip is $t_n = n \times t_{rt}$, where t_{rt}, the photon round-trip time in the cavity, is given by $t_{rt} = 2L/c = 1/FSR$, and thus $t_n = n/FSR$. After a time $t_n = \tau = 1/2\pi\delta\nu$ the photon would have remained in the cavity with probability $1/e$. Thus, $n = FSR/2\pi\delta\nu$ showing that the cavity finesse divided by 2π is the number of round-trips the photon performs until the probability that it is still inside is $1/e$.

Note that, since the FSR of the narrowband cavity is 14.6 GHz, and the corresponding round trip time $t_{rt} = 68.5$ ps, the incoming photons should be transmitted through the cavity only after a multiple of t_{rf} and the histogram should then display periodic peaks with this spacing. However, the broadband photons pass first through the broader filtering cavity, with a linewidth of 2.5 GHz, and a decay time of 64 ps. Then, the incoming photons are spread to a time of the same order as

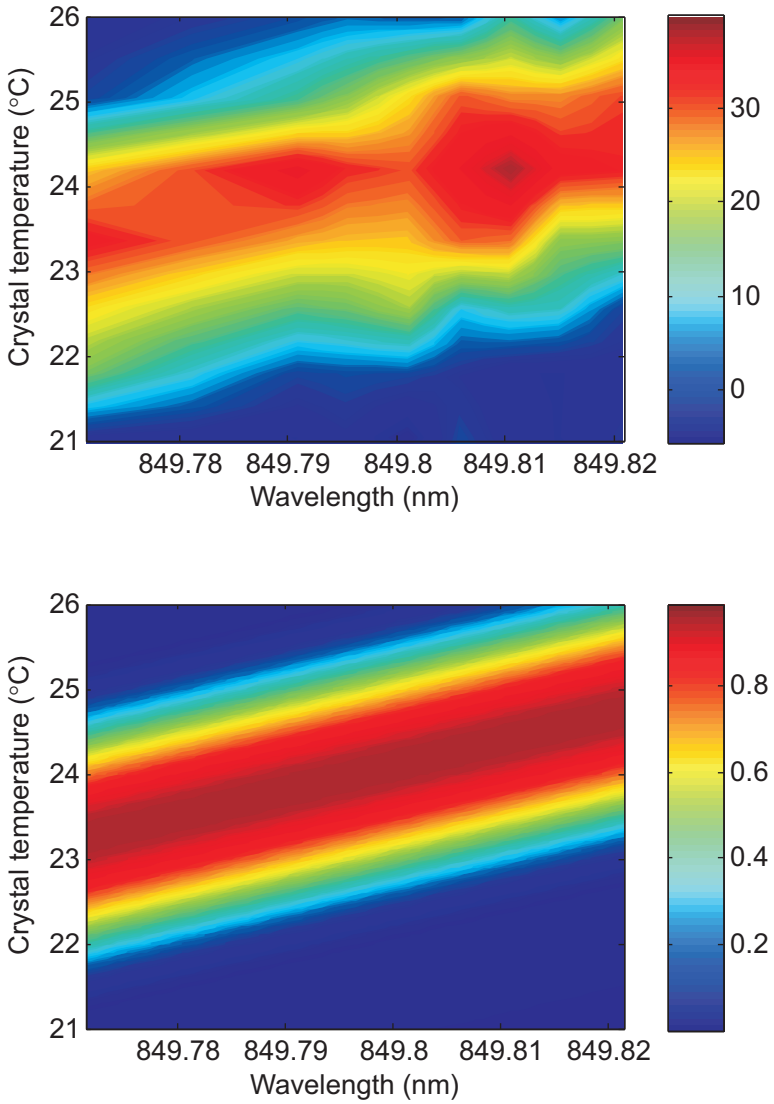

Figure 6.2.: Experimental coincidence rate (top panel) and theoretical coincidence coincidence efficiencies (lower panel) as a function of the 850 laser wavelength and the crystal temperature.

the round trip time of the second cavity, and the peak structure can not be resolved. In addition, the detectors have a jitter of 500 ps, washing out any structure with a characteristic time below this value.

6.2. Tunability of generated photons

The central wavelength of the photon pairs can be adjusted by tuning the master laser wavelength. The down-converted photon pairs will be generated at the wavelengths satisfying the phase-matching conditions 2.1.1 and 2.1.2. Taking into account the crystal poling with period Λ and the refractive indices of each beam, these can be written as

$$\omega_p = \omega_s + \omega_i \tag{6.2.1}$$

$$\begin{aligned} \frac{\omega_p n\left(\omega_p, \mathbf{e_p}, T\right)}{c} &= \frac{\omega_s n\left(\omega_s, \mathbf{e_s}, T\right)}{c} \\ &+ \frac{\omega_i n\left(\omega_i, \mathbf{e_i}, T\right)}{c} \\ &+ \frac{2\pi}{\Lambda} + \Delta k, \end{aligned} \tag{6.2.2}$$

where $\omega_{P,S,I}$ are the pump, signal and idler frequencies, $\mathbf{e_{P,S,I}}$ their polarizations, T is the crystal temperature, Λ is the poling period, and Δk is the small allowed wave-vector mismatch due to the finite length of the crystal. The down-conversion efficiency η is given by

$$\eta\left(\omega_P, \omega_S, \omega_I, T\right) \propto \frac{\sin^2\left(\frac{\Delta k L}{2}\right)}{\left(\frac{\Delta k L}{2}\right)^2}. \tag{6.2.3}$$

To obtain the efficiency of degenerate pairs we set the signal and idler wavelengths to the same values $\omega_S = \omega_I = \omega_P/2$ in expressions (6.2.1) and (6.2.3). Figure 6.2 shows the measured filtered photon coincidences, and its theoretical prediction, as a function of the laser wavelength, tuned around the $D_{3/2} - P_{3/2}$ atomic transition, and crystal temperature. The measurement was performed by recording the total number of coincidences for different values of the crystal temperature and laser wavelength. The crystal temperature was varied by setting different setpoint values in the PID1500 temperature regulator (see Section 3.3). The laser wavelength was tuned by locking the laser to different longitudinal modes of the transfer cavity (see Section 3.1). For the theoretical prediction we used Sellmeier equations for the refractive indices and thermoptic coefficients given in Appendix C [50], and a poling period of 14.043μm at 25°C, with a temperature variation given by a published thermal expansion coefficient [63]. Even though this effect was included in the model, it was seen to have a negligible contribution compared to the thermoptic effect (variation of refractive index with temperature). The laser wavelength is given in air and was measured using our commercial wavemeter, HighFinesse WS-U, with a wavelength accuracy of 0.1 fm. The $D_{3/2} - P_{3/2}$ transition wavelength was measured to be 849.8015 nm. Taking into account that no parameter was fitted from the data, the agreement between theory and experiment is remarkable. From the graph we see that the wavelength of the photon pairs can be fine tuned around the $D_{3/2} - P_{3/2}$ atomic transition by adjusting the crystal temperature around $24°C$.

From Figure 6.2 we derive a variation of the central photon wavelength with temperature of $3.4\times10^{-2}\ nm/^{\circ}C$, a temperature bandwidth (FWHM) of $2.05^{\circ}C$ and a wavelength bandwidth (FWHM) of 0.076 nm. It is clear that for the tuning range of interest for interaction with an atomic transition ($\sim$100 MHz $\equiv\ 2\ \times\ 10^{-4}$ nm) the variation of the central photon wavelength with temperature compared to the temperature bandwidth is negligible. In experiments with atoms it is enough to control the crystal temperature with a precision of around 0.5°C.

6.3. Source brightness

One complication present in all the coincidence measurement in this experiment arises from the highly asymmetric detection rates in the two photon channels. In the unfiltered arm, the rates are of the order of $10^7 s^{-1}$, whereas in the filtered arm they are around $10^3 s^{-1}$. Given that the detector dead-time is specified to be around 50 ns, we can then expect a strong saturation in the unfiltered arm. In order to avoid this saturation loss in our characterization, we ran all the measurements at a low pump power. Moreover, we assume that all the properties of the source are conserved for higher powers. To assess the brightness of the source we measured the coincidence rate of filtered pairs as a function of the pump power. To do this, we set up a pump power regulator placing a half wave-plate mounted on a motorized rotation stage and a polarizing beam splitter before fiber SMF1 (see Figure 3.3), and a photodiode monitoring the outcoupled pump power, split from the main beam slightly transmitting mirror. The photodiode voltage is used as an error signal to feed back on the wave-plate angle and regulate the power to a specified setpoint. A automated LabVIEW program perfoms a scan of the pump power and records the number of coincidences in 600 s. The low power values were used to perform a linear extrapolation to high power. From this, we directly obtain a brightness of 4.8 pairs/(s mW). For the maximum pump power of 70 mW this results in an extrapolated detection rate of 340 pairs/s. Taking into account the bandwidth and the detector efficiencies, we find the spectral brightness of generated narrowband pairs to be 1.0/(s MHz mW).

6.4. Polarization entanglement of the photon pairs

We also characterized the polarization correlations of the photon pairs in the source. We used a NPBS to split the photons and placed a set of polarization analyzers in each arm. For a first characterization, only a HWP and a PBS was used in each arm, HWP1-PBS1 and HWP2-PBS2, respectively (see Figure 3.6). QWP1 and QWP2 were removed for this measurement. We measured the coincidences in 1 hour, obtained by integrating the time correlation peaks and subtracting the accidental coincidences, for different settings of HWP1 and HWP2's angles. The angle of HWP2, in the reflection arm of the NPBS, was set to four different values, 0°, 22.5°, 45° and 67.5°. In this way we performed polarization rotations with respect to the horizontal of twice these values and set the detection basis in the transmission of the

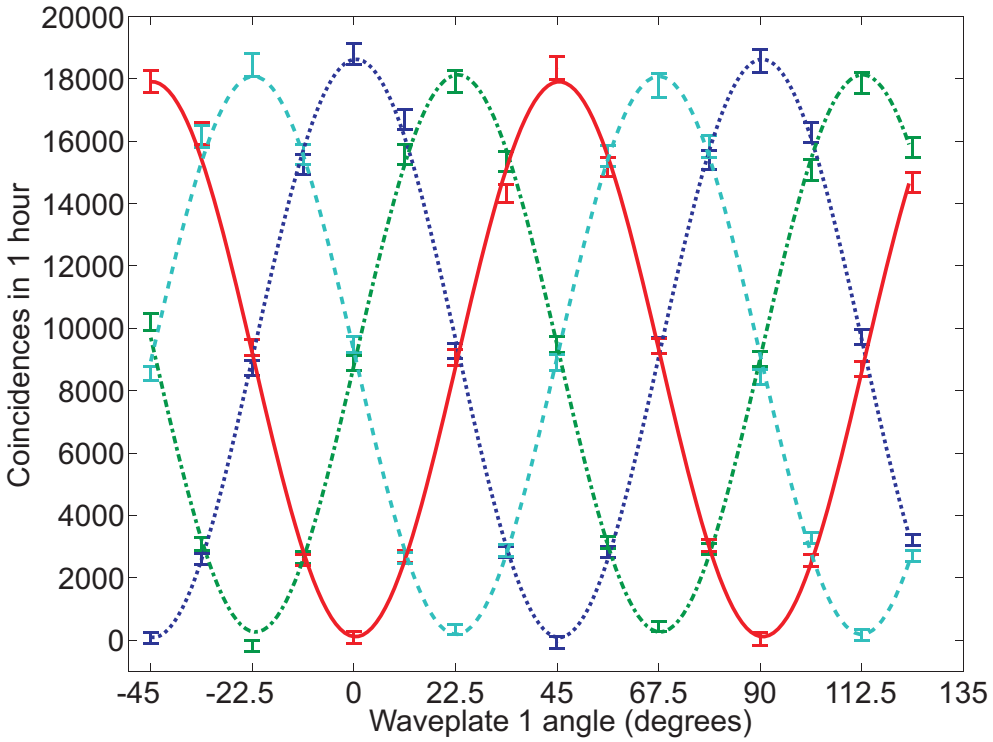

Figure 6.3.: Polarization correlation measurement. In each data set HWP2 was set to a fixed angle and HWP1 was rotated. The curves are least-square fits to the data. HWP2 angles for each data set are: $0°$ (red solid), $22.5°$ (green dash-dots), $45°$ (blue dots), $67.5°$ (light blue dashes). The average visibility is $99\ \%$ in the HV basis and $97.5\ \%$ in the DA basis

PBS to the four states $|H = 0°\rangle, |D = 45°\rangle, |V = 90°\rangle$, and $|A = 135°\rangle$, respectively. For each of these settings, HWP1 was rotated in steps of $12.5°$. Each data set was fitted with the function $a[1 + V \sin(\frac{\theta-\theta_0}{\alpha})]$. The results are shown in Figure 6.3. For the four aforementioned settings of HWP2, the obtained visibilities are $98.8 \pm 1.4\ \%, 97.1 \pm 1.2\ \%, 99.1 \pm 1.2\ \%$, and $97.9 \pm 1.5\ \%$, respectively.

A full characterization of the polarization properties of the two photons was obtained by performing a tomographic reconstruction of the two photon polarization state. For this, a quarter wave plate (QWP) was added in each polarization analyzer. Following [64], the coincidences counts in 1 hour were recorded for 16 different settings of the angles in the four different waveplates. Using the methods described in [64], a maximum likelihood estimate of the density matrix was obtained. The statistical error in the matrix was estimated by performing a set of 100 instances of the tomographical reconstruction, each of them with a different set of Poissonian noise added to the count rates. In the $\{|H,H\rangle, |H,V\rangle, |V,H\rangle, |V,V\rangle\}$ basis, the resulting matrix is given by

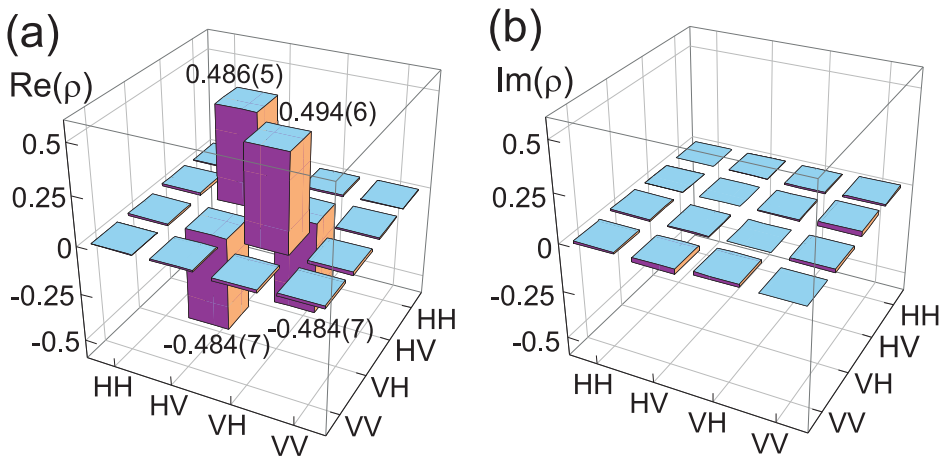

Figure 6.4.: Representation of the real part (a) and imaginary part (b) of the reconstructed density matrix.

$$Re\left[\rho\right] = \begin{pmatrix} 0.00024(6) & 0.0023(13) & -0.0048(15) & 0.00112(15) \\ 0.0023(13) & 0.4855(22) & -0.4651(16) & 0.0038(19) \\ -0.0048(15) & -0.4651(16) & 0.5056(20) & -0.000245(18) \\ 0.00112(15) & 0.0038(19) & -0.000245(18) & 0.0087(4) \end{pmatrix} \tag{6.4.1}$$

$$Im\left[\rho\right] = \begin{pmatrix} 0 & -0.0027(15) & 0.0001(15) & 0.0008(2) \\ -0.0027(15) & 0 & -0.002(4) & 0.0270(17) \\ 0.0001(15) & -0.002(4) & 0 & -0.0243(18) \\ 0.0008(2) & 0.0270(17) & -0.0243(18) & 0 \end{pmatrix} \tag{6.4.2}$$

and it is plotted in 6.4.

The knowledge of the density matrix allows us to characterize the degree of entanglement by calculating different entanglement measures. For example, the concurrence, calculated as

$$C[\rho] = max\left(0, \sqrt{\lambda_1} - \sqrt{\lambda_2} - \sqrt{\lambda_3} - \sqrt{\lambda_4}\right) \tag{6.4.3}$$

where λ_1 - λ_4 are eigenvalues of $\sqrt{\sqrt{\rho}\left(\sigma_y \bigotimes \sigma_y\right)\rho^*\left(\sigma_y \bigotimes \sigma_y\right)\sqrt{\rho}}$, ρ^* is the complex conjugate of the density matrix ρ and σ_y is the Pauli spin matrix, gives $C = 0.948 \pm 0.015$. The overlap fidelity $F = \langle\Psi^-|\rho|\Psi^-\rangle$ with the maximally entangled singlet state $|\Psi^-\rangle = \frac{1}{\sqrt{2}}(|\mathrm{H}\rangle|\mathrm{V}\rangle - |\mathrm{V}\rangle|\mathrm{H}\rangle)$, amounts to $97.6 \pm 1.1\%$.

The proximity of the measured polarization state to the singlet state was achieved by tuning the angle of the 50/50 beam-splitter separating the two photons. The angle was tuned by sending in a 850 nm laser beam with linear polarization through the same input port as the SPDC photons. The polarization of the reflected beam

was analyzed with a polarimeter (Thorlabs PAX5710). The angle of the beam-splitter was set such that the birefringence introduced by the beam-splitter was minimized, hence preserving the polarization of the input beam for different polarization angles. It is clear that this is ideally achieved with normal incidence, but such configuration does not allow splitting geometrically the two photons. Therefore, a small angle was allowed for, resulting in a slight reminiscent birefringence which is responsible for the unperfect fidelity of the measured state with respect to the singlet state.

7. Interaction of heralded single photons with a single ion

Trapping single ions and producing photon pairs suitable for interacting with them are remarkably complex tasks from the technical point of view, as was shown in Chapters 3 and 4. An even more challenging problem is to couple the two systems, and to achieve controlled interaction between single photons and single ions. Apart from developing the individual systems, a substantial research effort was dedicated to coupling them and to performing experiments which combine both setups.

This chapter describes how the combination of the two systems was achieved and which results were obtained. The first section briefly explains the first experiments, where the photon pair source was tuned to the 850 nm $D_{3/2} \leftrightarrow P_{3/2}$ transition of $^{40}Ca^{+}$, and the first signatures of the interaction was obtained. These experiments were realized in full collaboration between all members of the team, and the detailed explanations can be found in another thesis [61]. The conclusion from this experiment was that the efficiency of the scheme was not high enough to clearly observe interesting quantum features of the atom-photon interaction. The following sections explain thoroughly the experiments realized with a more efficient scheme, where the source was tuned to the 854 nm $D_{5/2} \leftrightarrow P_{3/2}$ transition of $^{40}Ca^{+}$. With this configuration, the single-photon single-atom interaction rate was high enough to observe the time correlation between the absorption of one photon and the detection of the partner photon. Several schemes to observe this interaction were tested, from lower to higher complexity and degree of control over the system. A full analysis of different experiments and techniques used to obtain these results will be developed in this chapter, which forms the core part of this thesis.

7.1. First detection of interaction between SPDC photons and a single ion on the $D_{3/2} \leftrightarrow P_{3/2}$ transition.

The experiments described in this section were performed in collaboration with other members of the team, and the detailed explanation of the results can be found elsewhere [42, 61]. Here they are summarized for completeness.

The simplest scheme to observe the absorption of down-converted photons by the $^{40}Ca^{+}$ ion is briefly described in Chapter 5. The ion is continuously driven by the 397 and 866 nm lasers. The 397 laser is red detuned to cool the motion of the ion, while the 866 laser is necessary to repump the ion out of the $D_{3/2}$ state. Under these excitation conditions, the ion continuously emits 397 nm photons, when decaying from the excited $P_{1/2}$ state to the $S_{1/2}$ ground state. Part of these photons are captured by the HALO lens and are detected by the PMT. Under no other ex-

Transition	Branching ratio	Oscillator strength
$P_{3/2} \leftrightarrow S_{1/2}$	93.47%	0.6262
$P_{3/2} \leftrightarrow D_{3/2}$	0.66%	0.0103
$P_{3/2} \leftrightarrow D_{5/2}$	5.87%	0.0618

Table 7.1.: Branching ratios [65] and oscillator strengths [61] of decays from $P_{3/2}$.

citation, the PMT detects a constant rate of photons. In this scheme, the source is tuned to the 850 nm $D_{3/2} \leftrightarrow P_{3/2}$ transition. The absorption of a photon from the source by the ion excites it to the $P_{3/2}$ level. The subsequent decay probability to the different levels is given by the branching ratios, in Table 7.1.

The ion most likely decays to the $S_{1/2}$ ground state and no effect is detected because the interruption of the 397 nm scattering lasts only a few nanoseconds. However, with about 6% probability it decays to the metastable $D_{5/2}$ state, which is uncoupled to any other level. The ion then stops emitting 397 photons and the count rate in the PMT suddenly drops to the background level. This event is termed a *quantum jump* because the quantum state of the ion has changed "suddenly" [18, 19, 20].

Spurious quantum jump events can also arise from other sources, such as collisions with background gas atoms or excitation to the $P_{3/2}$ state by absorption of background light. To give a convincing proof that the observed jumps are caused by the source photons, we performed two proof-of-principle experiments.

In the first experiment, we measured the rate of quantum jumps as a function of the temperature of the PPKTP crystal in the source, while sending to the ion the unfiltered photon. In parallel, the rate of detected photons in the filtered arm vs. temperature was measured. Figure 7.1 shows the experimental data, together with the theoretical curve which models it. A variation in the crystal temperature produces a shift in central frequency of each photon pair, around the degenerate frequency corresponding to half the pump frequency. To very good approximation, the frequency dependence on temperature is linear. Therefore, a scan in the crystal temperature is equivalent to scanning the unfiltered photon spectrum through the atomic transition. Since the filter mimics the absorption spectrum of the ion and the spectra of the two photons in the pair are symmetric, the filter transmission rate and the quantum jump rate have a similar dependence on the crystal temperature. The solid line in Figure 7.1 is obtained theoretically as explained in Section 2.1.2. Since it closely fits both data sets, we can conclude that they follow the same behavior, as expected. The data was taken in four sweeps, each at 15 minutes per point, for a maximum of one hour acquisition per temperature setting. The average rate of quantum jumps for the optimum temperature is 0.58 jumps/min.

In the second experiment, we coupled the filtered photon to the ion and measured the rate of quantum jumps versus the central frequency of the source, thereby tuning the filtered photon around the $D_{3/2} \leftrightarrow P_{3/2}$ atomic transition. The data was taken in several sweeps of 5 minutes, for a total of 1 hour acquisition time per point. The resulting data is shown in Figure 7.2. The rate of quantum jumps in the optimum frequency is 0.23 ± 0.06, essentially one third of the rate that was obtained with

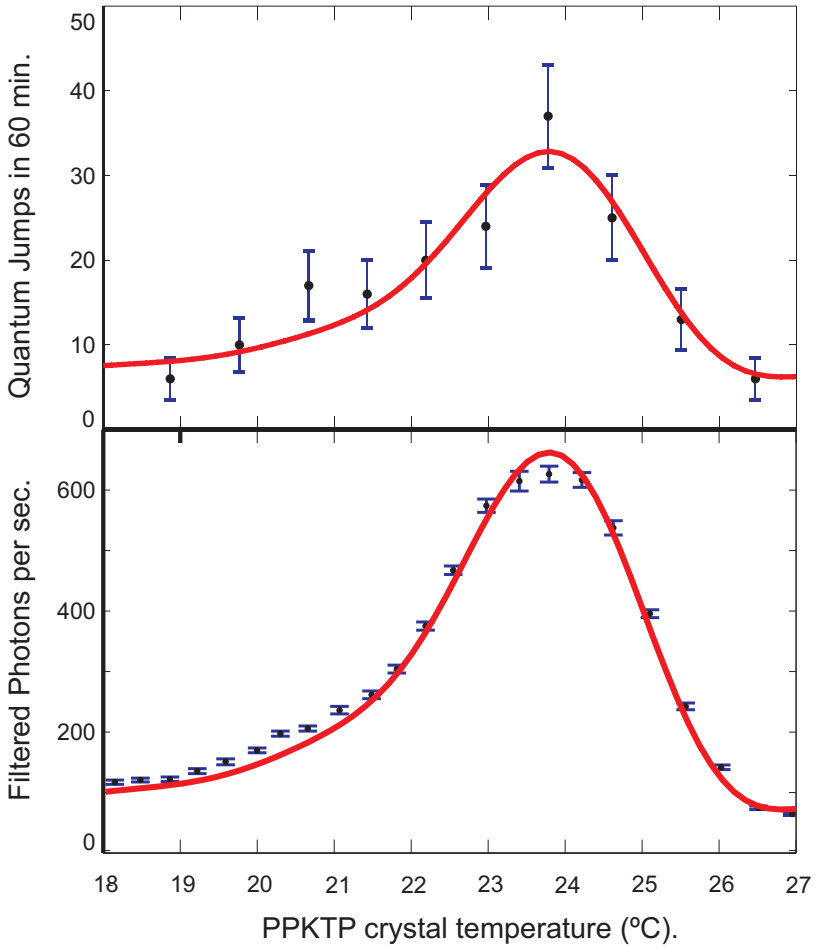

Figure 7.1.: Rate of quantum jumps (top) and of detected filtered photons (bottom) as a function of the PPKTP crystal temperature. The solid red curves are the calculated curves based on the fiber coupled down-conversion spectrum described in Section 2.1.2.

the unfiltered photon experiment. Such a low rate did not allow to obtain the data with good statistics within a reasonable time, so the errors in the measurements are substantially high. In any case, the measured dependence satisfyingly matches the calculated curve (solid line), obtained by convoluting the filtered photon spectrum and the measured atomic transmission spectrum.

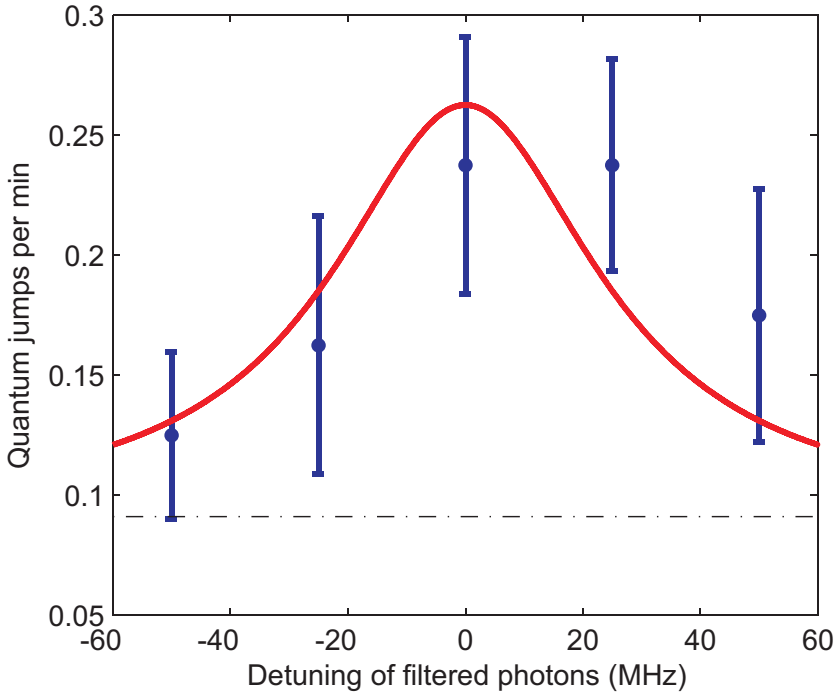

Figure 7.2.: Rate of quantum jump (top) produced by the filtered photons as a function of their central frequency, detuned around the atomic transition (calibrated to by at 0MHz). The solid curve is the expected lorentzian line obtained from convoluting the atomic transition spectrum with the filtered photon spectrum. The dotted line represents the measured rate of spurious quantum jumps, measured by covering the SPDC beam.

7.2. Absorption of heralded photons in the $D_{5/2} \leftrightarrow P_{3/2}$ transition: continuous driving

This section discusses the first experiments we performed to observe the interaction of SPDC photons with a single $^{40}Ca^{+}$ ion on the $D_{5/2} \leftrightarrow P_{3/2}$ transition. Here, all the preparation, excitation and detection of the ion happens in a continuous way. First, the experimental setup coupling the two systems will be briefly described. Then, the techniques to align the SPDC photon beam onto a single ion will be elaborated, followed by a discussion on how to excite the ion to maximize the rate of fluorescence it emits. Later, the first experimental evidence we obtained of the interaction of the ion with the SPDC photons will be explained, followed by the main results of this section, showing the correlation of the absorption event with the detection of the partner photon.

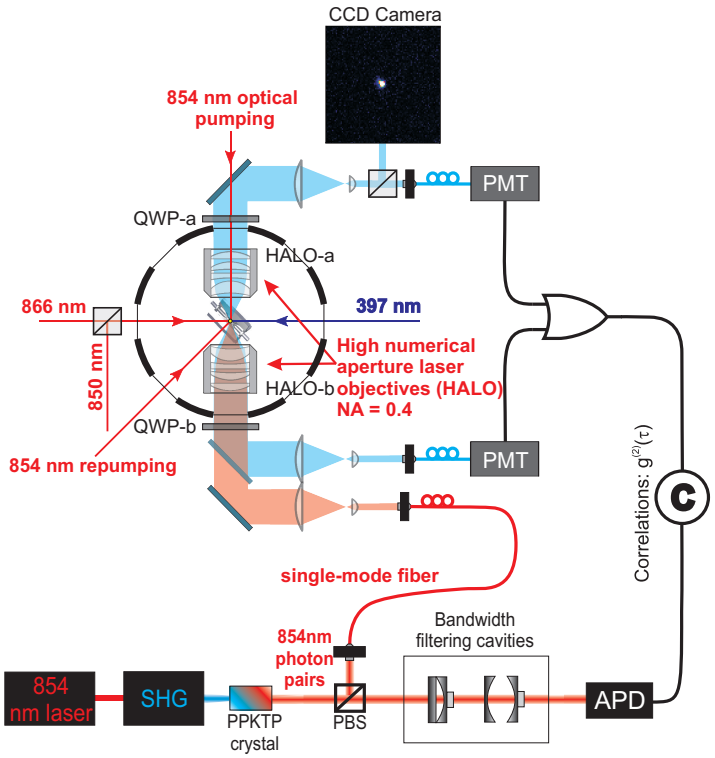

Figure 7.3.: Simplified scheme of the experimental setup connecting the ion trap and the SPDC photon source used to detect the interaction of a single $^{40}Ca^{+}$ ion with down-converted photons. See text for details.

7.2.1. Experimental setup

The ion trap and photon pair source setups have already been described in detail in Chapters 3 and 4. Here it is briefly shown how the two systems were combined to perform photon-ion interaction experiments. Figure 7.3 shows a simplified diagram of the experimental setup.

The 854 master laser is tuned to the $D_{5/2} \leftrightarrow P_{3/2}$ transition. It is frequency doubled and down-converted into degenerate photon pairs at the same wavelength. These photons are split, one is directed to the ion and the second one is sent to the frequency filtering stage, which is designed to mimic the atomic absorption spectrum. The transmission of the filter is coupled to an avalanche-photodiode (APD) which detects single photons. The pulses generated in the APD are sent to one channel of PicoHarp. The photon going to the ion is expanded to cover the full HALO aperture, and is then focused tightly onto the ion to maximize the photon absorption probability. The aim is to detect the correlations between the filtered photon and the absorption event of its partner photon by the ion. This absorption event is detected by monitoring the 397 blue fluorescence light emitted by the ion. Both HALOs are used to collect the fluorescence light, covering in total 8% of the solid angle. Multimode fibers are used to collect this light and direct it to two

photo-multiplier tubes (PMTs), each of which produce a TTL pulse whenever it detects a photon. These pulses are combined in an OR gate and sent to the second channel of PicoHarp.

7.2.2. Tuning and aligning the source with the ion

Two important previous steps before trying to detect the single-photon single-ion interaction must be realized: the tuning of the source to the atomic transition and the alignment of the source beam onto the ion. These tasks are usually realized once every day before starting the experiment, and repeated periodically during the experiment to ensure that the conditions are preserved stable. Here we describe each of the tasks in detail.

Tuning and aligning the source on the ion are somewhat cumbersome tasks the first time they are done, but then become simple routinely jobs for everyday operation. Both procedures rely on sending the source 854 nm laser beam directly to the ion. As shown in Figure 3.6, an 854 laser beam passes through an electronic shutter (SH1), then gets to the beam-splitter (BS) which splits the SPDC photons, and is transmitted and coupled to the single mode fiber (SM3) which goes to the ion trap setup. A digital signal controlling the shutter is produced by a National Instrument data acquisition card (DAQ) and can be controlled at any time through the LabView computer control program.

When the tuning and alignment tasks have to be done, SH1 is activated, sending the 854 laser to the ion through the same mode used for the SPDC photons. The laser reaches the ion through HALOa, and is set to vertical polarization. Since the magnetic field is always set along the HALO axis, the V-polarized 854 nm laser can excite both σ^+ and σ^- transitions with the same intensity. No π transitions are induced. Additionally, the ion is excited by the 397, 866 and 850 nm lasers, while fluorescence is recorded on the PMT. If no 854 laser is coupled to the ion, or if it is far off-resonant, the ion is efficiently pumped to the $D_{5/2}$ level and no fluorescence is observed. If the 854 laser is properly tuned and aligned on the ion, it will efficiently repump the ion out of the $D_{5/2}$ state and back to the cooling cycle, hence increasing the rate of fluorescence. The fluorescence rate thus provides a reference signal to optimize the alignment and the tuning.

Course alignment and tuning: The alignment of the down-conversion beam on the ion is performed by adjusting the HALO position and the incoupling mirrors (M1-M4 in Figure 4.2). The initial alignment is done geometrically, by centering the 854 nm laser beam on the input and output vacuum chamber viewports. This ensures that the beam is traversing the center of the ion trap. At this point, the laser has to be roughly tuned to the atomic transition. To do so, the laser must be operated unlocked and roughly set to the literature value of the transition wavelength by varying the laser piezo voltage and biasing current by hand. With sufficiently high 854 laser power, this should be enough to start observing fluorescence on the PMT. Once the fluorescence signal is detected, the laser wavelength is tuned and the beam is aligned by maximizing the PMT rate. If the fluorescence rate becomes insensitive to any of the two parameters, as a consequence of the saturation of the

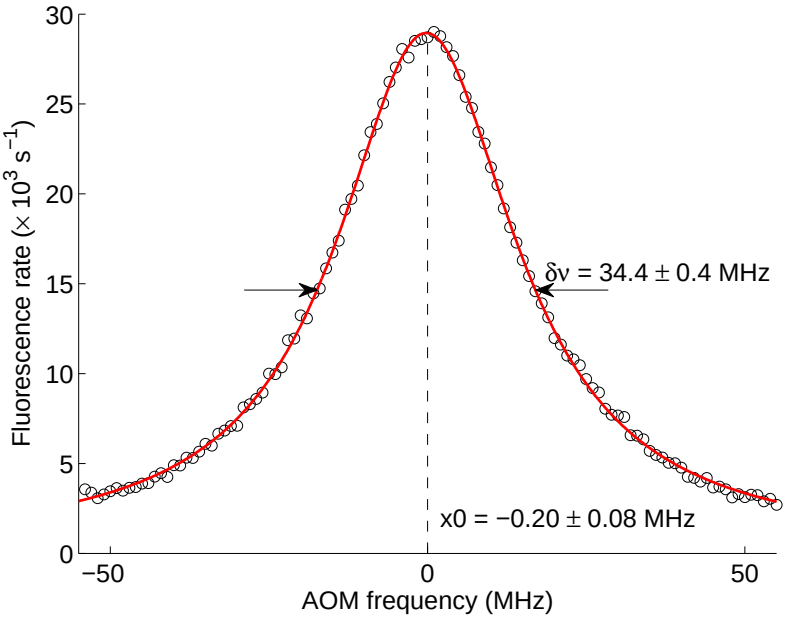

Figure 7.4.: Excitation spectrum performed by scanning the source 854 nm laser frequency while the fluorescence rate detected in the PMT is recorded. The 397, 866 and 850 lasers are also exciting the ion.

$D_{5/2} \leftrightarrow P_{3/2}$ transition, the 854 laser power is reduced below saturation. In practice, to seek for the first signal, a power of around 1 mW is used. When the beam is close to its optimum alignment and the wavelength is close to resonance, very low power, of the order of 100 nW, is needed. Note that this beam is tightly focused onto the ion by the HALO lens, producing high intensities with quite low laser powers.

Fine alignment and tuning: Once the 854 laser is roughly tuned on resonance and the corresponding wavelength measured with the wavemeter is known it is stabilized to the closest transfer cavity mode. If the resulting wavelength is far from the resonance the transfer cavity temperature must be varied, as explained in Section 3.1.

As described in Chapter 3, the source can be precisely tuned by varying the central frequency of the RF signal feeding the AOM. The AOM controls the frequency of the 852 nm reference laser onto which the transfer cavity is locked to. The transfer cavity length therefore follows this frequency change, and the frequency of the 854 nm master laser, which is itself locked to this cavity, is varied accordingly. Since the filtering cavities are locked to this master laser, the variation of the RF signal frequency is finally transferred to a change in the central frequency of the filtered photons. Energy conservation in SPDC requires that the partner photons with which the filtered photons are time correlated are also detuned by the same frequency.

Fine tuning of the wavelength, once the laser is locked close to resonance, is done by varying the AOM RF frequency. This task must be realized every day before

starting interaction experiments, and whenever some unexpected problem might cause the source to get detuned from resonance (as for example a jump out of lock of the transfer cavity). For this, an 854 excitation spectrum is taken, by scanning the AOM driving frequency and recording the fluorescence rate at each value. This is performed automatically with a sequence implemented in our pulse sequencer (Hydra). A typical spectrum which results from this is plotted in Figure 7.4. A lorentzian fit determines the AOM frequency of the atomic resonance. Since the 854 laser excites both σ transitions, the spectrum is an average over all transitions which vary the magnetic quantum number by $\Delta m = \pm 1$. In particular, the resulting spectrum is symmetrical around the degeneracy transition frequency (for null magnetic field). For low magnetic fields, the spectrum can be approximated fairly well with a lorentzian function and the position of the peak of the lorentzian corresponds to the degeneracy frequency. Once the transition wavelength is found, the wavemeter reading of the 854 nm laser wavelength provides a good reference to tune the source later. The typical range of values for this reading is 854.2084(1) nm in air, where the error is due to the accuracy of the wavemeter.

The fine alignment of the SPDC photon beam is realized by optimizing the fluorescence rate while varying the position of each optical element. Initially, the HALO and incoupling mirrors (M1-M4 in Figure 4.2) are optimized one by one, independently. Later, the HALO and one incoupling mirror (e.g. M4) are beam-walked in each degree of freedom. Finally, the position of the fiber outcoupler (Fc1) and the mirror before the magnifying telescope (M1) are beam-walked. This process is repeated iteratively until the fluorescence rate does not increase anymore. As with the frequency tuning, it is necessary to keep the 854 nm laser power low enough to avoid saturating the transition.

The distance of the HALO to the ion must also be optimized to set the focal spot of the 854 beam at the position of the ion. The distance is initially varied in continuous mode of the piezo stage, until a peak in the fluorescence rate is found. Then, the position is scanned more carefully by shifting the Z-piezo stepwise through the fluorescence peak. After a few steps, the focal spot can suffer some lateral displacement, so a bit of compensation with the X and Y piezos must be performed, always optimizing the fluorescence rate. This is illustrated in Figure 7.5, where the fluorescence dependence with the HALO distance is plotted. During this measurement, the 854 laser intensity was kept far below saturation during the full position scan. The fluorescence rate should then be proportional to the 854 laser intensity at the ion position. Since the beam entering the HALO is collimated, scanning the HALO distance and monitoring the fluorescence rate is a way of characterizing the focused mode along the propagation axis. However, a reliable calibration of the piezo displacement per step is not available, so not much can be done with this data beyond determining the optimum position.

7.2.3. Fluorescence photon detection efficiency

One important parameter of the ion trap system is the efficiency of detection of the 397 nm fluorescence photons. In our setup, both HALOs are used to collect these.

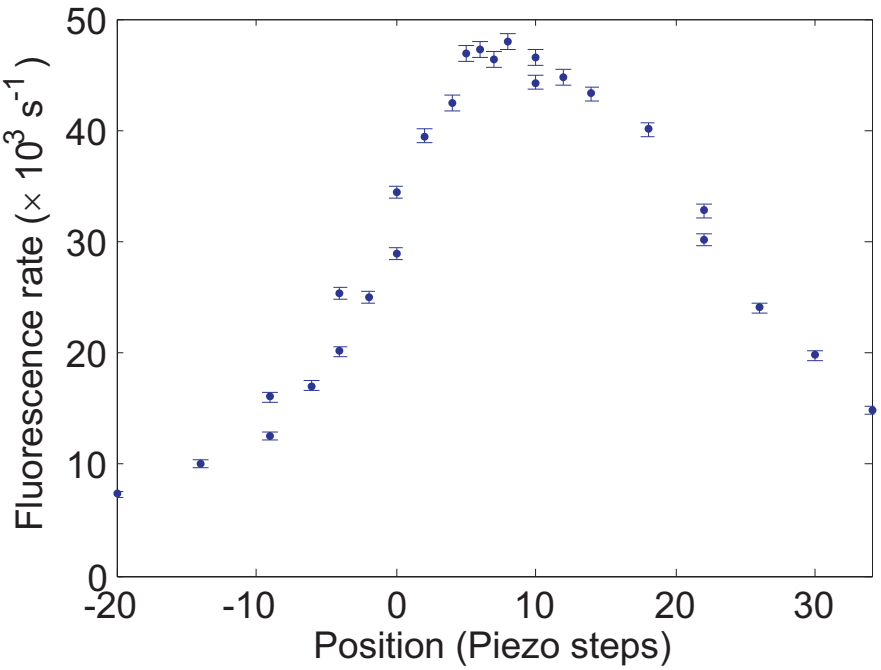

Figure 7.5.: Fluorescence rate dependence with the distance of the HALO from the ion. Each step of the piezo position was driven with a peak voltage of 20V.

In principle, each HALO collects 4% of the solid angle and the PMT photon detection efficiencies are estimated to be 30%. However, each beam passes through several optical elements and are fiber coupled before reaching the PMTs, so additional losses are expected.

To characterize these losses completely, we performed spectroscopy on the $D_{3/2} \leftrightarrow P_{1/2}$ transition of a single ion. For this, we recorded the fluorescence rate $f_{exp}(\nu)$ collected by both HALOs as a function of the frequency of the 866 nm laser, ν in the presence of the 397 nm repumping laser. By means of an eight-level Bloch equation model of the system we fit these spectra obtaining all the relevant experimental parameters, including the laser Rabi-frequencies, the detuning of the 397 laser, the magnetic field and polarizations of both lasers [46]. The model itself gives the relative population of all the the atomic levels as a function of the 397 laser frequency, ν, and in particular of the $P_{1/2}$ state, $p_{P_{1/2}}(\nu)$. This function is fitted to the experimental spectrum $f_{exp}(\nu)$ by adjusting all experimental parameters and a scaling factor A relating the two functions. The detected fluorescence rate is given by $p_{P_{1/2}} \times \Gamma \times \eta$, being $\Gamma = 2\pi \times 20.99$ MHz the $P_{1/2}$ level decay rate and η the detection efficiency. Hence, the detection efficiency is given by $\eta = A/\Gamma$. An example excitation spectrum is shown in Figure 7.6 with the corresponding model fit. The extracted parameters $(\Omega_{397}, \Omega_{866}, \Delta_{397}, \Delta_{866}) = 2\pi \times (13.05, 4.02, -14.77, -15.96)$ MHz are the Rabi frequencies of the 397 and 866 lasers, the detuning of the 397 laser and the resonance frequency of the 866 transition, respectively, $B = 4.79$ Gauss is the applied

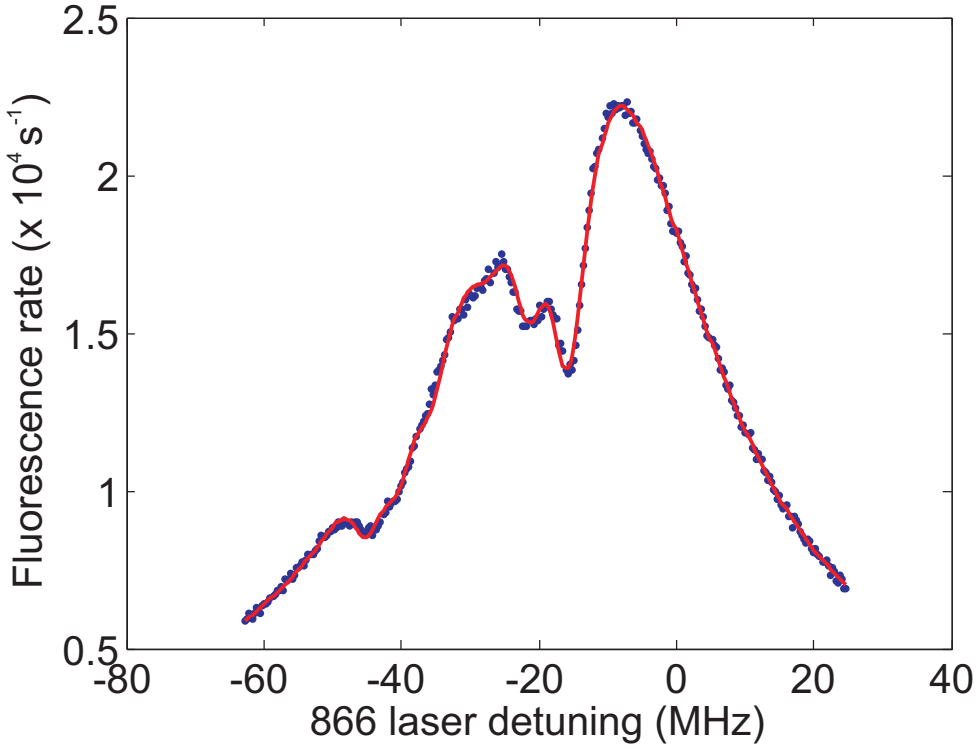

Figure 7.6.: 866 nm laser excitation spectrum. Dots are experimental data points and the solid line is a fit to the eight level Bloch equation model.

magnetic field and $A = 1.48 \times 10^6$ counts/s is the scaling amplitude. From this last values, we extract a detection efficiency of $\eta = \frac{1.48}{2\pi \times 20.99} = 1.12\%$. This value can be explained as the product of the collection angle of both HALOs (8%), the detection efficiency of each PMT (30%) and all the losses in the optics traversed by the fluorescence light (50%).

7.2.4. Detection of the interaction on the $D_{5/2} \leftrightarrow P_{3/2}$ transition

This subsection describes the first attempts to detect the interaction of a single ion with the SPDC photons tuned to the 854 nm $D_{5/2} \leftrightarrow P_{3/2}$ transition. The source was tuned and aligned to the ion as described in the previous subsection. When the alignment process was completed, the 854 laser was switched off and the 850 laser was strongly attenuated, such that it induced a rate of quantum jumps lower than the decay rate of the $D_{5/2}$ level. Fluorescence photons at 397 nm were collected with one HALO and directed to a PMT to detect them. The time-tags of each click were stored for postprocessing.

A typical trace of the fluorescence rate against time is plotted in Figure 7.7. The plot was obtained by counting the number of clicks in bins of 1 ms, during a total time of 100 seconds. The ion is repeatedly undergoing quantum jumps. The

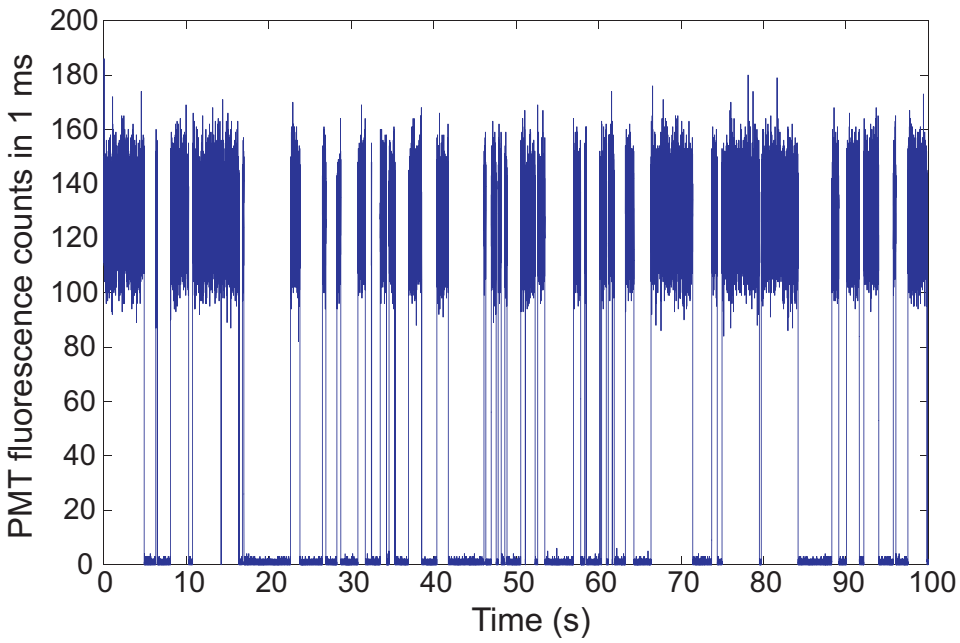

Figure 7.7.: Trace of detected fluorescence photon counts in the PMT when ion is jumping between the bright and the dark state. A binning of 1 ms is used.

absorption of a photon from the 850 nm laser and the subsequent decay from the $P_{3/2}$ state to the uncoupled $D_{5/2}$ state removes the ion from the cooling cycle, hence stopping the emission of 397 nm fluorescence photons. The ion can get back to the cooling cycle, therefore becoming bright again, by two mechanisms:

- Spontaneous decay to the $S_{1/2}$ state,
- Absorption of an 854 nm photon from the source and subsequent decay from $P_{3/2}$ to $S_{1/2}$ or $D_{3/2}$.

To prove the interaction of the SPDC photons with the ion, we then realized two measurements, one with the source beam on and a second one with the source beam blocked. For each measurement, we obtained a fluorescence time trace as in Figure 7.7 and we measured the duration of each dark period, using the threshold technique described in Chapter 5. To obtain the threshold for the onset of a quantum jump, a histogram of the counts in the full time trace is plotted (Figure 7.8). The bright state is clearly distinguished from the dark state by setting a threshold value between the two peeks. A good criterion to set this threshold is to take the point of minimum counts between the two peaks in the histogram. A matlab code automatically obtains this threshold, detects each quantum jump and measures their duration.

Histograms of the quantum jump durations are plotted in Figure 7.9, for the case when the ion is not exposed to the SPDC photons (a) and when it is (b). Bins of 200

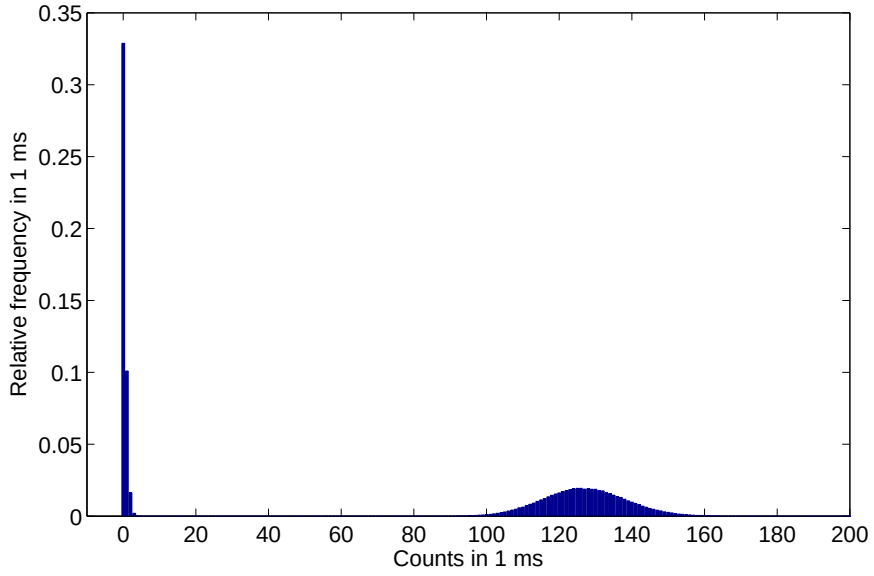

Figure 7.8.: Histogram of detected fluorescence photon counts when the ion is jumping between the bright and the dark state. A binning of 1 ms is used.

ms were used, and the histogram was normalized to one by dividing the counts per bin by the total number of events. These normalized histograms are statistical approximations of the distribution of dark period durations.

We now explicitly derive these distributions. Assume that the ion is initially in the $D_{5/2}$ state with 100% probability. Additionally, the probability that the ion decays in a small interval ΔT is $p_1(\Delta T) = R_1 \Delta T$, where R_1 is the rate of spontaneous decay of the $D_{5/2}$ level. Similarly, $p_2(\Delta T) = R_2 \Delta T$ is the probability that it absorbs an 854 photon and reenters the cooling cycle within this same time period. The probability $P(t)\Delta T$ that the ion reenters the cooling cycle in the time interval $(t, t + \Delta T)$ is given by the probability that it has not done so in a time t times the probability of decaying in the following ΔT seconds. Therefore, $P(t)\Delta T = [1 - p_1(\Delta T)]^n [1 - p_2(\Delta T)]^n [p_1(\Delta T) + p_2(\Delta T)]$, where $n = t/\Delta T$. We have used the fact that the probabilities p_1 and p_2 describe events which are statistically independent. Finally, taking the limit for infinitely small times ΔT we get

$$\begin{aligned} P(t)dT &= \exp(-R_1 t)\exp(-R_2 t)(R1 + R2)dT \\ &= e^{-(R_1+R_2)t}(R1 + R2)dT \end{aligned} \tag{7.2.1}$$

Note that $P(t)$ is a probability distribution function, and as such it is normalized. Additionally, the average decay rate R and decay time τ can be obtained by fitting an exponential function to the data, or more simply as,

$$R = 1/\tau = 1/\langle t \rangle, \tag{7.2.2}$$

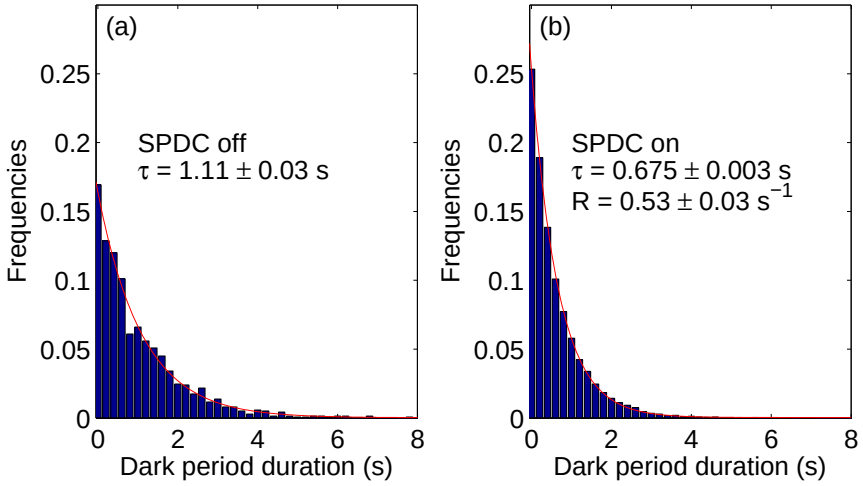

Figure 7.9.: Histograms of dark period duration when ion is exposed to the highly attenuated 850 nm laser. In a), the ion is not exposed to the SPDC photons at 854 nm. This is therefore a measurement of the spontaneous decay time of the $D_{5/2}$ level. In b) the ion is exposed to the source photons. Solid curves are exponential fits to data, and the displayed decay times are derived from such fits.

that is, computing the average over the measured dark period durations. The corresponding error is given by the standard error of the mean

$$\begin{aligned} \delta\tau &= \frac{\sigma_t}{\sqrt{N}} \\ \delta R &= R^2 \delta\tau, \end{aligned}$$

where σ_t is the standard deviation of the measured sample of delays and N is the number of events.

In case 7.9(a) of our measurements the only decay mechanism present is spontaneous emission from $D_{5/2}$ to $S_{1/2}$. In case (b), both spontaneous emission and stimulated absorption from $D_{5/2}$ to $P_{3/2}$ contribute. We can then compute the rates R_1 and R_2 from this data. For the spontaneous decay time we directly obtain $\tau_1 = 1110 \pm 30$ms, from the data in Figure 7.9(a), which corresponds to $R_1 = 0.901 \pm 0.024\text{s}^{-1}$. From Figure 7.9(b), we get $\tau = 675 \pm 3$ms and a corresponding rate, $R = R_1 + R_2 = 1.481 \pm 0.007\text{s}^{-1}$. Subtracting these two values we obtain the rate $R_2 = 0.53 \pm 0.03\text{s}^{-1}$ of absorption of an 854 nm photon from the source and the subsequent decay to $S_{1/2}$ or $D_{3/2}$. The corresponding photon absorption rate, taking into account the branching ratios given in Table 7.1, is $R_a = R_2 \times \frac{100}{100-5.87} = 0.56 \pm 0.03\ \text{s}^{-1}$. Note that the quantum jump rate in the $D_{5/2} \leftrightarrow P_{3/2}$ transition is around 56 times stronger than in the $D_{3/2} \leftrightarrow P_{3/2}$ transition.

The spontaneous decay time of the $D_{5/2}$ level $\tau_1 = 1110(30)$ ms is in good agreement with the literature value of 1168(11) ms [66]. The small difference may be

explained by spurious processes such as collisions quenching the $D_{5/2}$ state.

7.2.5. Correlated absorption under continuous excitation

After detecting a clear signature of SPDC photon absorption events by a single ion, we were ready to search for the time correlation of these events with the detection of the twin photon. The first attempts to realize such an measurement were performed with the source tuned to the $D_{3/2} \leftrightarrow P_{3/2}$ transition at 850 nm, as reported in [61]. Several technical difficulties present in those first experiments, both on the ion setup and on the source setup, impeded the observation of a clear correlation:

- A low rate of 0.58 photon absorptions / min. This was due to the low efficiency of the interaction scheme using the $D_{3/2} \leftrightarrow P_{3/2}$ transition at 850 nm. The low efficiency of this scheme with respect to the $D_{5/2} \leftrightarrow P_{3/2}$ scheme can be understood in terms of the different branching ratios and oscillator strengths of the transitions involved. The absorption probability of a photon on a given transition is directly proportional to its oscillator strength [67, 61]. The ratio of the oscillator strengths of the $D_{5/2} \leftrightarrow P_{3/2}$ and $D_{3/2} \leftrightarrow P_{3/2}$ transitions, given in Table 7.1, gives a factor of 6 higher efficiency in the $D_{5/2} \leftrightarrow P_{3/2}$ scheme. In addition, for a quantum jump event to be detected in the $D_{3/2} \leftrightarrow P_{3/2}$ scheme, the ion must decay to the $D_{5/2}$ state upon the absorption of an 850 nm photon. Therefore, the efficiency of this scheme is lower by an additional factor of 0.0587 given by the branching ratio of the $P_{3/2} \leftrightarrow D_{5/2}$ transition (Table 7.1). The absorption rate of the $D_{5/2} \leftrightarrow P_{3/2}$ scheme is therefore a factor of 102 more efficient than in the $D_{3/2} \leftrightarrow P_{3/2}$ scheme. As a consequence, experiments with the $D_{3/2} \leftrightarrow P_{3/2}$ scheme required extremely long acquisition times in the correlation measurements (over 12 hours), during which the stability of both experiments was hard to maintain. It was substantially improved by switching to the 854 nm transition which enhanced the rate by 2 orders of magnitude.
- A low detection efficiency of the 397 nm fluorescence photons, which directly determines the time resolution of the photon absorption event (see Chapter 5). This was improved in several ways: 1) By using both HALOs (with two PMTs) to collect the 397 nm fluorescence (only one HALO-PMT was used in the original experiments). The clicks from both detectors were combined into a single channel by means of a TTL OR circuit. A factor of two in efficiency was gained. 2) By replacing the old PMTs by more efficient ones (see Section 4.5). Another factor of 2-3 was gained. 3) Cleaning optical fibers used to collect the ion fluorescence and to direct it to the PMTs. The fibers tips turned out to be quite dirty during the first experiments. Overall, a factor of 10 was gained in the count rate of the fluorescence photons, and therefore in the time resolution of the SPDC photon absorption event.
- Background light on the trigger arm produced APD clicks not coming from SPDC photons. This light seamed to arise from fluorescence produced in the PPKTP crystal by the pump laser, at wavelengths above 860 nm. It was eliminated by introducing an additional 900 nm short-pass interference filter (Ed-

mund Optics NT47-588) in the trigger arm, after the filtering cavities. The use of a single-mode fiber, instead of a multimode fiber, to collect the light after the filtering cavities and direct it to the APD also helped.

Overall, the signal-to-noise ratio of the whole measurement was improved by 2 to 3 orders of magnitude, with an increase of 2 orders of magnitude in rates, and a corresponding reduction in the required acquisition time and gain in stability.

The experimental procedure to detect the correlations starts as follows. The source is properly aligned, for high efficiency, as described in Chapter 3. A single ion is loaded in the ion trap. The conditions of operation of the ion trap are set and calibrated with the procedure described in Chapter 4. As a result, the ion is exposed to a magnetic field biasing the main coils, and therefore the quantization axis is set along the HALO direction. Next, the source is tuned to the atomic transition and aligned on the ion, using the techniques described in section 7.2.2. This step is usually repeated every 30 minutes, to ensure stability in the alignment and tuning conditions. The 397 and 866 laser frequencies and intensities are set to achieve the highest possible fluorescence rate.This is important to achieve a high time resolution in the photon absorption event. Under the best conditions, rates of up to 6×10^5 photons / s are detected with both PMTs. This allows a time resolution, given by 5.3.12, of 5 μs. Finally, the 850 nm laser, exciting the $D_{3/2} \leftrightarrow P_{3/2}$ transition and pumping the ion to the dark $D_{5/2}$ state, is switched on. Its power is set such that the rate of quantum jumps (excitations to $D_{5/2}$) it induces is lower than the decay rate from $D_{5/2}$. Typically, a rate of 0.3 quantum jumps per second are produced. This laser is directed to the ion perpendicular to the magnetic field and with vertical polarization, thereby exciting both σ^+ and σ^- transitions. As a consequence, this optical pumping scheme prepares the ion in a mixture of all Zeeman substates of $D_{5/2}$.

To acquire the data, the APD detecting the trigger photons and the PMTs detecting the ion fluorescence are connected to two channels of the PicoHarp module. The time-tagged time-resolved (TTTR) mode is used to save the arrival times of each click on the two channels. Each event consists of a 64 bit number giving the detection time with a resolution of 4 ps[1]. However, the limit in time resolution is given by the jitter of the detectors. The APD has a time resolution of ~ 400 ps while the PMTs have around 280 ps. Moreover, these values are far below both the typical precision of $\sim 5\mu$s with which a photon absorption event can be detected and the time spread of the trigger photon (7 ns).

To prove the time correlation between the photon absorption and the detection of the trigger photon, we calculate the $g^{(2)}(\tau)$ correlation function between the two events. First, the photon absorption event must be extracted from the data. For this, the technique described in Section 5.3 is used. This technique detects the end of each quantum jump and saves the first fluorescence photon detection time after the ion turns on. As a result, a file of click times representing the moment when the ion reentered the cooling cycle is obtained. This list is then correlated with the

[1]The rate of data storage in this experiment is huge: the fluorescence channel accumulates ~ 4 MBytes/s while the trigger channel saves ~ 8 kBytes/s. A typical data acquisition shot lasts 10 minutes, amounting to a total of 2.4 GBytes.

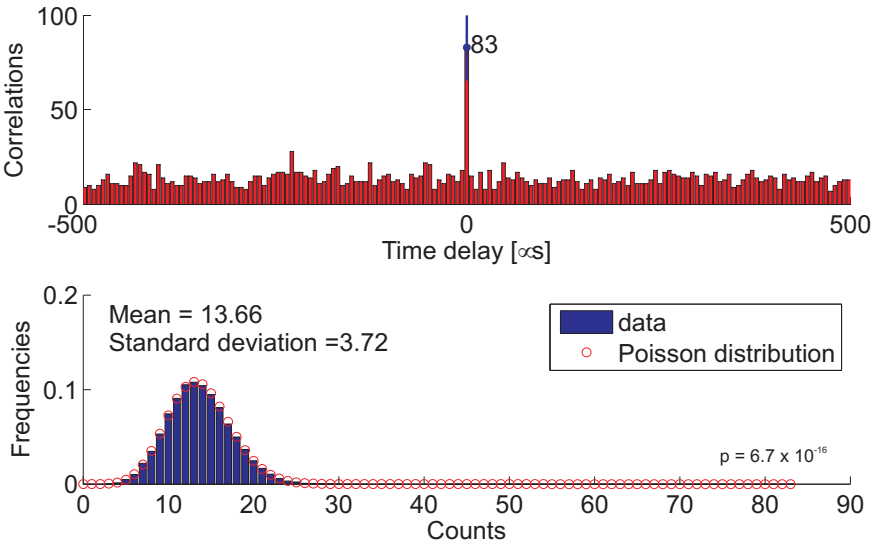

Figure 7.10.: Measurement of correlations between trigger photon and the quantum jump event. Top: $g^{(2)}$ correlation function as a function of the time delay between the two events. Bottom: Statistical analysis of data. The distribution of counts is plotted and compared to a poissonian distribution with a mean value obtained from the average number of counts in the background. Also shown is the probability that the correlation event happened by chance.

times of trigger photon detections, available in a separate file, obtaining the desired $g^{(2)}$ function.

A typical example of the resulting $g^{(2)}(\tau)$ correlation function as a function of the time delay τ between absorption and trigger events is shown in figure 7.10a. A binning of 6 μs was used, ensuring that all correlation events fall into a single bin. The data corresponds to a total of 50 minutes of acquisition time. A clear peak at delay $\tau = 0$ emerges above a random background. In figure 7.10b, a statistical analysis of the $g^{(2)}$ histogram is performed. A histogram of the number of correlations in the background is plotted, together with the calculated Poisson distribution $P_{BG}(\mu = 13.66; m)$. Here, m is the number of correlations in the background points, and μ is the mean value, obtained by averaging the background counts. The distribution of background counts is perfectly well reproduced by the Poisson distribution. This allows us to perform a test of the significance of the correlations observed at delay $\tau = 0$, namely m = 83. We calculate the probability that at least this number of correlations was obtained by chance, that is $p = \sum_{m=83}^{\infty} P_{BG}(\mu; m)$, resulting in a value of $p = 6.7 \times 10^{-16}$. The probability that the correlation peak was observed due to fluctuations in the background is completely negligible.

Now we can characterize the correlation efficiency, by first deriving the absorption rate and then comparing to the correlation rate. A similar analysis as the one performed to obtain Figure 7.9 yields an absorption rate of $R_{abs} = 0.55 \pm 0.04$ s^{-1}.

The correlation rate is $R_{corr} = [(83 - 13.7) \pm \sqrt{83}]/3000\ \mathrm{s}^{-1} = 0.023 \pm 0.003\ \mathrm{s}^{-1}$. These two numbers cannot be compared directly. The correlation rate is a direct measurement of the number of correlations per unit time, while the absorption rate is obtained by measuring the average decay time from the $D_{5/2}$ state due to photon absorption. This last number does not include the ratio of the total time that the ion actually remained in the $D_{5/2}$ dark state waiting for a photon absorption, or, in other words, the population $p_{D_{5/2}}$ of the $D_{5/2}$ state. This population can be easily obtained by measuring the total time t_{dark} that the ion spent in the dark state and comparing it to the total acquisition time $t_{total} = 3000$ s. For the current data set, this amounts to $t_{dark} = 1837.033$ s. Therefore, $p_{D_{5/2}} = 0.6123$. The effective absorption rate is given by $R_{abs}^{eff} = p_{D_{5/2}} \times R_{abs} = 0.337 \pm 0.024\ \mathrm{s}^{-1}$. Finally, the correlation efficiency amounts to $\nu_{corr} = R_{corr}/R_{abs}^{eff} = 6.8 \pm 1.0\%$. This efficiency can be understood in terms of all the losses present in the trigger arm, namely, the fiber coupling efficiency of SPDC photons ($\sim 65\%$), filter transmission efficiency ($\sim 45\%$), optical losses before the filter ($\sim 5\%$), fiber coupling efficiency after the filter ($\sim 85\%$) and detector efficiency ($\sim 30\%$), leading to an overall estimated efficiency of $\sim 7\%$. In section 7.3, we show how these absorption and correlation rates were enhanced by running the experiment using a pulsed scheme.

The measured $g^{(2)}$ correlation function has an average background of 13.66 correlations uniformly distributed over all time. This background arises from the correlation of the absorption of a photon in one pair with the detection of the trigger photon of another pair.

7.2.6. Spectroscopy on the $D_{5/2} \leftrightarrow P_{3/2}$ transition using heralded single photons

As a proof of principle experiment, after detecting the correlated absorption of single photons from the source by a single ion, we measured the dependence of the correlations as a function of the SPDC source central frequency. The source can be easily tuned around the $D_{5/2} \leftrightarrow P_{3/2}$ atomic transition once its wavelength is stabilized close to it. As a reminder, what is actually tuned is the central frequency of the laser to which the filtering cavities are locked to. Since energy must be conserved in SPDC and the pump beam is at exactly twice the frequency of that of the filtering cavities, any detected filtered photon must have a time correlated partner generated with the same spectrum. Therefore, tuning the filter locking frequency is equivalent to tuning the spectrum of the photon going to the ion when it is heralded by the detection of its partner photon going through the filtering cavities.

With this in mind, the correlated absorption rate should then vary strongly with a frequency variation of the order of the atomic transition linewidth, some tens of megahertz. However, since the SPDC photons going to the ion are not filtered and have a large bandwidth of ~ 150 GHz, the absorption rate itself should not have an appreciable dependence on frequency variations of this order. To illustrate this, we measured both the absorption rate and the correlation rate as a function of the source frequency, varying the latter around the atomic transition. The resonance frequency was again obtained by 854 laser spectroscopy in the presence of the 850,

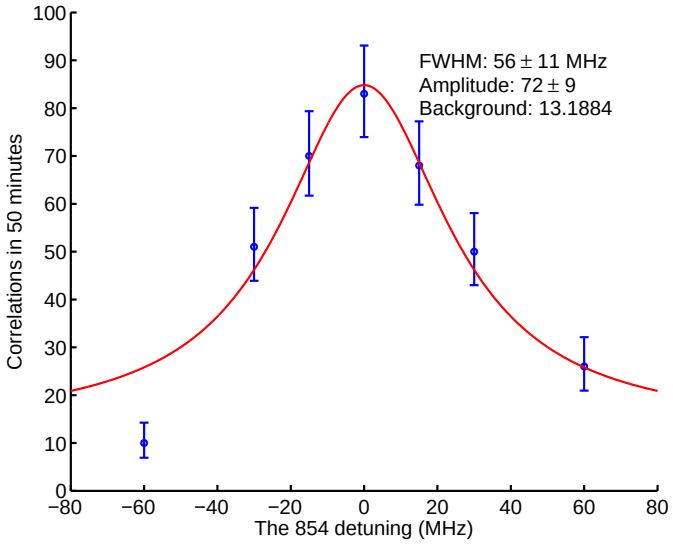

Figure 7.11.: Dependence of the correlation rate with the detuning of the central frequency of the SPDC photons around the $D_{5/2} \leftrightarrow P_{3/2}$ transition. In the x-axis, 0 MHz corresponds to the resonance frequency obtained by laser spectroscopy. The solid line is a lorentzian fit to the data, with the relevant parameters shown in the figure. The constant background value used in the fit was obtained by averaging the background of the $g^{(2)}$ correlation functions of each point.

397 and 866 lasers (see Section 7.2.2).

Figure 7.11 presents the results. The data points are plotted with 64% confidence intervals (corresponding to one standard deviation in gaussian-distributed data) estimated assuming that each point is poissonian distributed. The solid line is a fit consisting of a constant background plus a lorentzian function. The background value was obtained by averaging the background level of the correlation functions of each point. The fit gives a linewidth of

$$\delta\nu = 55 \pm 11 \text{ MHz}. \tag{7.2.3}$$

This value must be compared to a theoretical expectation, which is obtained by convoluting the heralded photon spectrum with the atomic transition spectrum. The former has a lorentzian lineshape with a measured linewidth of $\delta\nu_{photon} = 22.0(5)$ MHz, as was shown in Section 6.1. In order to obtain the atomic spectrum, all possible transitions from $D_{5/2}$ to $P_{3/2}$ which change the magnetic quantum number by $\Delta m = \pm 1$ must be considered. Each of them contributes a lorentzian spectrum of 22 MHz linewidth, displaced by the appropriate Zeeman shift, and weighted by its Clebsch-Gordan coefficient (assuming uniform initial populations in all Zeeman sublevels). This results in a linewidth of $\delta\nu_{ion} = 26.5$ MHz for the magnetic field of 2.5 Gauss used in these measurements. The convolution of two lorentzian

functions of linewidths $\delta\nu_{photon}$ and $\delta\nu_{ion}$ gives a new lorentzian function with a linewidth $\delta\nu_{total} = \delta\nu_{ion} + \delta\nu_{photon}$. The expected correlation spectrum should then be a lorentzian with a total linewidth of 48.5(5) MHz, in very good agreement with the measured value given in Equation 7.2.3.

7.3. Absorption of heralded photons in the $D_{5/2} \leftrightarrow P_{3/2}$ transition: pulsed scheme

In the last section, the simplest scheme to detect the correlated absorption of SPDC photons on the $D_{5/2} \leftrightarrow P_{3/2}$ transition was shown. This scheme allowed to perform proof-of-principle experiments to clearly prove the interaction of heralded single photons with single trapped ions. However, an extra degree of control is required if the systems are meant to be used for quantum information processing purposes. In those experiments, the lasers and the source excited the ion continuously, so the whole process occurred randomly. With the pulsed method described in this section, better control over the process is obtained in several respects:

1. Before, the optical pumping to the $D_{5/2}$, from where the ion can absorb SPDC photons, was quite uncontrolled. It was done by coupling a very week 850 nm laser beam, which induced sudden jumps to the $D_{5/2}$ state in completely random times. The rate at which this happened determines the population of the $D_{5/2}$ state, and therefore the rate of absorption of photons from the source. Now the optical pumping will be controlled much better, allowing to optimize the time the ion spends in the $D_{5/2}$ state ready to absorb SPDC photons.
2. The new optical pumping scheme allows to prepare the ion in specific Zeeman substates. This allows to make use of the polarization properties of the SPDC photons.
3. When the ion remains in the $D_{5/2}$ state it does not scatter 397 nm laser photons and is therefore not laser cooled. The duration of these periods with absence of cooling was also out of control in the continuous scheme. Average dark time durations of 0.5-1 s were observed, in which the motion of the ion can suffer a drastic heating. With the new pulsed scheme, the time the ion spends in these dark periods, and therefore the heating it suffers, is much better controlled.

Overall, the new pulsed scheme will result in an enhancement of the rate of the absorption, as well as a proof of the polarization dependence of the interaction. Furthermore, the techniques used here open the way towards implementing more advanced schemes to use the SPDC photon - ion interaction for useful purposes, such as entanglement transfer between photon pairs and ions.

7.3.1. Getting to control the system: the pulsed sequence

The pulsed sequence used to run the experiment is illustrated in Figure 7.12. It is divided in three phases: 1) cooling, 2) state preparation, and 3) detection. The se-

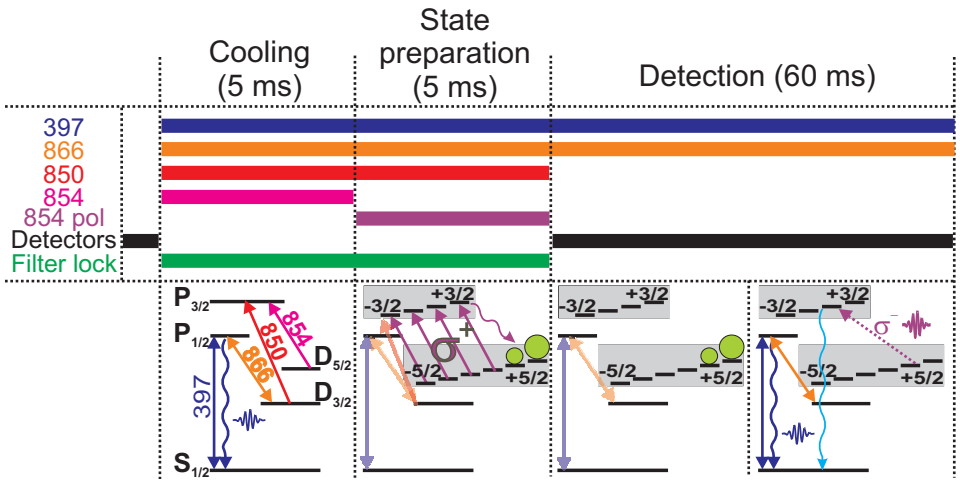

Figure 7.12.: Pulse sequence to run the experiment, with the corresponding effect on the ion. See text for details

quence is synchronized with the chopper in the photon pair source setup, such that during the time the chopper transmits the 854 locking beam to stabilize the filtering cavities, the preparation of the ion is performed (cooling and state preparation). In this way, the source and the ion setups go through their preparation phases at the same time, therefore optimizing the available time for data acquisition. This works by feeding the TTL signal generated with the photo-diode monitoring the locking beam, in the source setup, to a digital input of the Hydra pulse sequencer. This digital signal triggers the beginning of the pulse period, programmed in Hydra.

Two separate 854 nm beams are coupled to the ion. One of them is sent through HALOb, along the quantization axis, and is right or left circularly polarized, inducing σ^+ or σ^- $D_{5/2} \leftrightarrow P_{3/2}$ transitions. We will call this the 854 pumping beam. The second beam is directed perpendicular to the quantization axis with vertical polarizations. It then induces both σ^+ and σ^- transitions together, and it will be called the 854 repumping beam. Both beams are derived from the locking beam going to the filtering cavities, after it passes through the optical chopper, as shown in Figure 7.13. The 854 pumping beam is directly sent to the ion after the chopper. The 854 repumping beam first passes through a stage of two AOMs in single pass, which allows switching it on and off. The two AOMs are aligned such that the mode of diffraction order +1 of the first AOM is coupled to the mode of diffraction order -1 of the second AOM. Both AOMs are fed with the same RF signal. Therefore, the second AOM compensates the frequency shift produced by the first one. In principle, an electro-optic switch could have been used for this purpose instead, but this device was not available at the time of the experiment.

During the cooling phase, which lasts 5 ms, all lasers exciting the ion are switched on, the detectors are gated off, and the source filters are stabilized to the 854 master laser. The ion is laser cooled by the 397 nm laser, which is red detuned, and repumped out of all other states by the 866, 850, and both 854 nm laser beams.

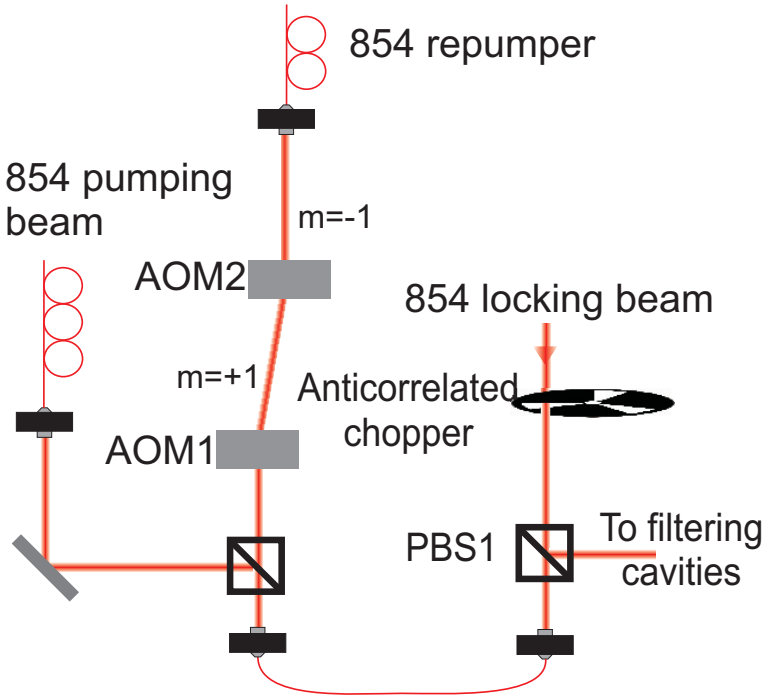

Figure 7.13.: Optical setup to derive the 854 pumping and repumping beams used in the pulsed sequence. The filtering cavities locking beam transmitted through the chopper is split in two. One beam is directly used as the 854 nm (σ polarized) pumping beam. The second one is sent through AOM1. The diffraction order m = +1 is sent through AOM2 such that it transmits diffraction order m = -1. The resulting beam is the 854 repumping beam in the pulsed sequence. Both AOMs are driven with the same RF source, and hence mutually cancel their frequency shifts.

In the state preparation phase, with a duration of 5 ms, the 854 repumping beam is switched off. The combination of the 850 and the 854 pumping beams optically pumps the ion to the outer Zeeman substates of the $D_{5/2}$ level. Note that a mixture of the two outermost Zeeman states is prepared, with $m = +3/2, +5/2$ if the 854 beam is set to σ^+, or $m = -3/2, -5/2$ if it is set to σ^-. The exact weights of the mixture depend on the Clebsch-Gordan coefficients of all the transitions involved in the state preparation. However, from any of those two Zeeman substates, the ion is only sensitive to σ^- 854 nm photons in the positive m states and to σ^+ photons in the negative m states. This is of course only true for photons impinging on the ion along the quantization axis, as in the current case, since π transitions are not induced. During this phase, the filtering cavities in the source are still being stabilized.

In the final detection phase of around 60 ms, the data acquisition is started. The

850 and 854 pumping lasers are switched off and the PMTs are gated on. The locking beam of the filtering cavities in the source is blocked by one side of the chopper, and the transmission of the cavities, coupled to the APD, is opened on its opposite side. Therefore, the APD is exposed to the filtered SPDC photons and the PMTs are exposed to the 397 fluorescence photons. In these experiments, again both HALOs are used to collect fluorescence. Each beam is coupled to a PMT, and the electric pulses from these are combined into a single channel by an OR circuit. The pulses from the PMTs and from the APD are sent to the two channels of PicoHarp, and the same data processing as in section 7.2.5 is performed.

To guarantee a high efficiency of optical pumping, the 850 beam is left on until the 854 repumping is completely blocked by the chopper (note that the chopper blocks this beam gradually). A small security delay of 500 μs is introduced in the sequence, for this purpose.

Another significant advantage of this scheme is that, since the detectors are gated off during the cooling phases where the ion is bright, and only gated on in the detection phase where it is mostly dark, the amount of fluorescence clicks saved in the data files is drastically reduced compared to the continuous case. This makes long measurements feasible and data analysis less demanding in terms of computation time.

7.3.2. Polarization sensitive correlations

With the full polarization pumping sequence, described in Section 7.3.1, the ion becomes sensitive to 854 photons of only one circular polarization. If the ion is pumped to the positive Zeeman substates (using a σ^+ polarized 854 pumping beam), it is sensitive to σ^- polarized photons only, and vice-versa. Note that a σ^+/σ^- transition is produced by increasing/decreasing by 1 the angular momentum of the ion along the direction of the applied magnetic field, $\delta m = \pm 1$. By the definition of helicity, a photon with polarization vector $\mathbf{e_L} = \frac{1}{\sqrt{2}}(\mathbf{e_x} \pm i\mathbf{e_y})$, i.e. left/right circular, has an angular momentum of $\pm\hbar$. Therefore, left/right circularly polarized photons will produce σ^+/σ^- transitions, respectively.

In these experiments, quarter waveplates QWP-a and QWP-b are used to set the polarizations of the 854 pumping beam and the SPDC photon beam, respectively (see Figures 4.2 and 7.3). The two beams emerge from fiber couplers Fc1 and Fc4 with vertical polarization. By rotating the fast axis of the quarter waveplates to $\pm 45°$ with respect to the vertical, the polarization of the two beams can be set to left or right circular. If the quantization axis is pointing from HALO-a to HALO-b, a σ^+ transition is produced by the SPDC photons with right circular polarization and σ^- optical pumping is also given by right circular polarization of the 854 pumping beam (since these beams enter from opposite sides). These polarizations were first set using the polarimeter. Then, they were checked by sending 854 laser light through each side separately, while exciting the ion with 397, 866 and 850 lasers, and setting the angle of each QWP to minimize the fluorescence rate. Finally, both beams were sent together and the fluorescence rate was observed to be maximized, as expected if each beam excites a different σ transition.

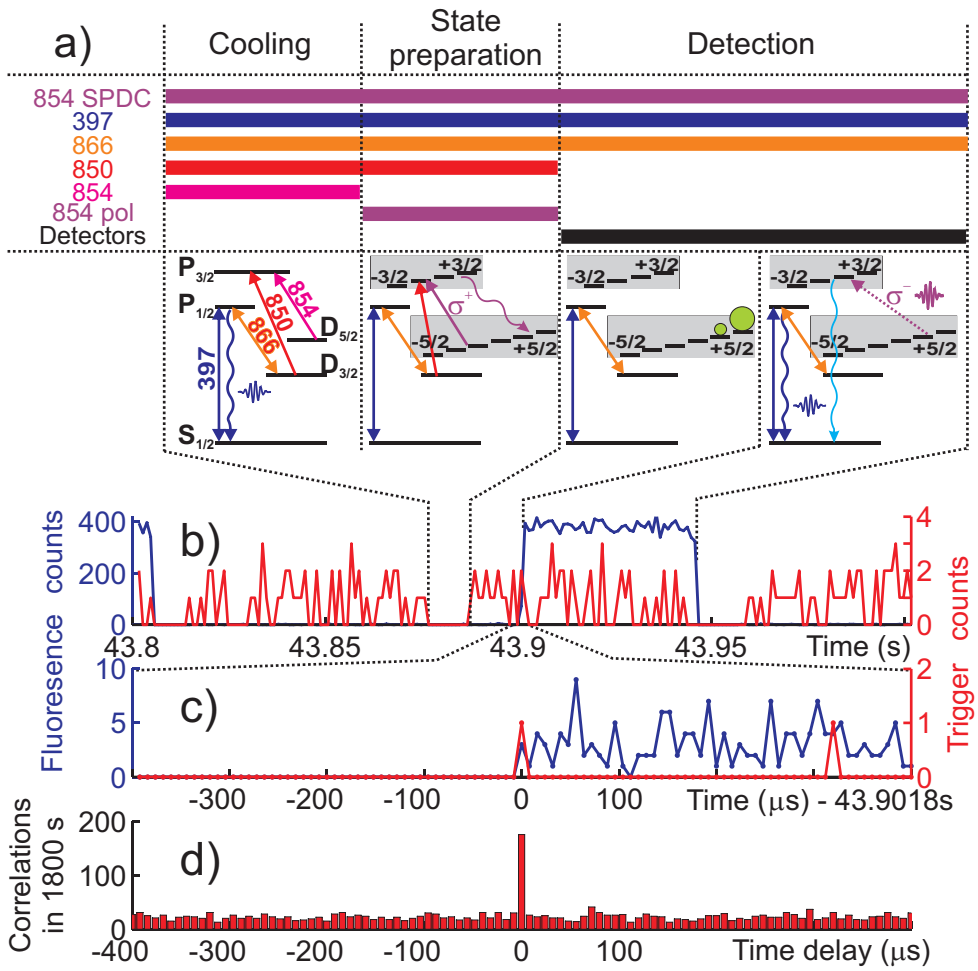

Figure 7.14.: Pulse sequence presented together with the measured experimental data. In a) the pulse sequence is shown again, with the effect on the ion level scheme. b) shows a trace of the APD (red) and PMTs (blue) counts over time, obtained with a binning of 1 ms. c) shows the same trace zoomed in around a quantum jump event and calculated with a finer binning of 8μs. d) shows the $g^{(2)}$ correlation function of the trigger photon detection event and the first detected fluorescence photon in the end of a dark period. This data was obtained after 30 minutes of acquisition time.

Under these conditions, and after aligning and tuning the source to the ion, a correlation measurement was taken using the pulsed sequence described above. The results are illustrated in Figure 7.14.

Panel a) describes the pulsed sequence used to run the experiment, already explained in Section 7.3.1. In each cycle, after the cooling and state preparation phases, the state of the ion is initialized onto the two outer Zeeman substates of

the $D_{5/2}$ level. In this example, σ^+ light was used for the 854 pumping, so the ion is prepared in a mixture of $\left|D_{5/2}; m = \{3/2, 5/2\}\right\rangle$. As the Clebsch-Gordan coefficient of the $m = 3/2 \leftrightarrow 5/2$ transition is stronger than that of the $m = 1/2 \leftrightarrow 3/2$, we can expect that the final state has a greater population in the $m = 5/2$ state. From these levels, the ion is only sensitive to σ^- polarized photons in the $D_{5/2} \leftrightarrow P_{3/2}$ transition if the electric field has no component along the quantization axis (no π transitions are induced). This is the case in this experiment, where the SPDC photons are coupled to the ion along the direction of the applied magnetic field. By setting the SPDC beam to left circular polarization, they can be absorbed by the ion.

Panel b) shows part of the time evolution of the rate of fluorescence (blue) and trigger photons (red) detected on the PMTs and APD, respectively. The plot was obtained by discretizing the time axis in intervals of 1 ms and counting the number of clicks in each bin. In the cooling and state preparation phases, the detectors are gated off, so no clicks are detected. In the detection phase, a stream of APD clicks are detected with a constant rate. The ion stays dark most of the time, since it remains in the initial prepared state. Suddenly, the fluorescence rate increases drastically , showing that the ion entered the cooling cycle $S_{1/2} \leftrightarrow P_{1/2} \leftrightarrow D_{3/2}$. The ion underwent a quantum jump. This could have been due to an SPDC photon absorption or a spontaneous decay event from $D_{5/2}$ to $S_{1/2}$.

A small part of the time evolution is plotted in panel c) with higher time resolution. In this case, a bin size of 8 μs was used, and the time axis extends around the quantum jump event observed in panel b). The bin size is small enough to distinguish single clicks in the APD channel. At the same time, it is high enough to ensure that the first detected fluorescence photon falls inside the first bin after the quantum jump event. A detailed discussion on this was given in Chapter 5.

In the particular quantum jump event plotted in Panel c), a trigger photon is detected within the same time bin as the first fluorescence photon. This means that the photon absorption event is time correlated with the detection of a trigger photon.

The time correlation between the two events is better established by calculating the $g^{(2)}$ correlation function (Figure 7.14d). This is calculated in two steps, as was described in Section 7.2: 1) the first click after each quantum jump event is detected; 2) then, the second order correlation function between these clicks and the trigger photon detections is calculated. The plot displays a peak at zero time delay, with 175 ± 13 correlations, above a flat background of 19.8 correlations on average. Since the the total acquisition time was 30 minutes, this results in a rate of correlations of $5.2(4)$ min$^{-1} = 0.086(7)$ s^{-1}.

As a proof that that the interaction efficiency depends on the polarization of the SPDC photon, we measured the correlation rate as a function of the angle of QWP-b (Figure 7.15). The angle is calibrated such that 0° corresponds to right circular polarization, while 90° to left circular. The $g^{(2)}(\tau)$ function is measured for each angle setting during 10 minutes, and the value $g^{(2)}(0)$ is taken as the number of correlations. The fitted sine function (solid line) reveals that the correlation rate is reduced to the average background level at an angle of 90°, confirming the full

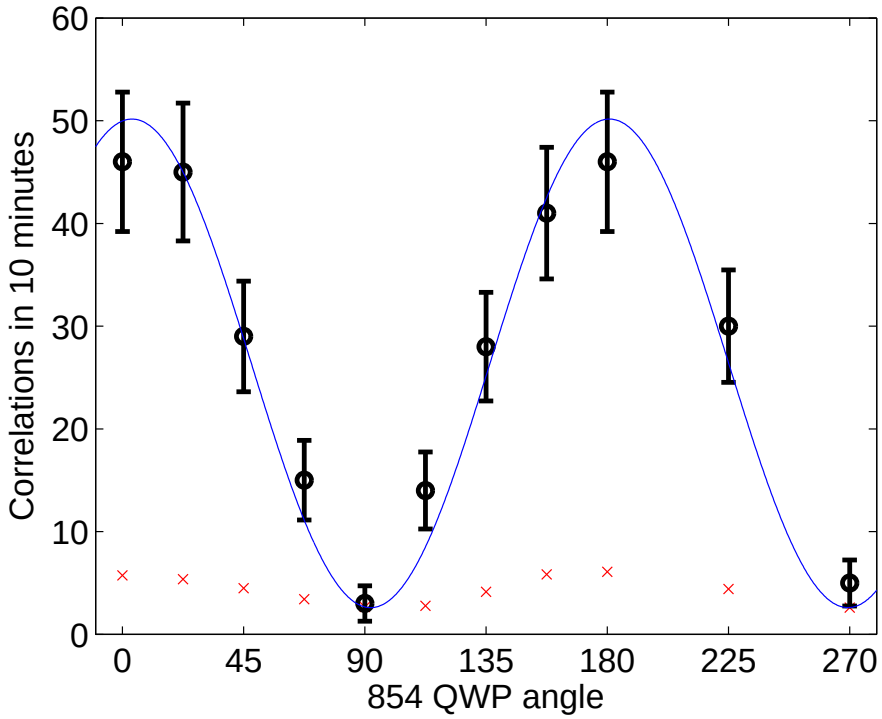

Figure 7.15.: Polarization dependence of the correlation rate. The angle of QWP-b is varied and the number of correlations in 10 minutes is measured. When the angle is 0° (90)°, the polarization of the photon impinging onto the ion is right (left) circular. The solid curve is a fit of a sine function. The average background level of each $g^{(2)}$ function is also shown (×)

suppression of the interaction efficiency at the wrong polarization.

The background of each $g^{(2)}$ is proportional to the rates of events in each channel. Since the absorption rate varies sinusoidally with the polarization, the background level follows the same tendency.

7.3.3. Spectroscopy on a single ion with single photons

In a second proof-of-principle experiment, we performed spectroscopy on a single trapped $^{40}Ca^{+}$ ion using heralded single photons from the source as the probe. We measured the rate of correlated absorption events as a function of the central frequency of the photon pairs around the $D_{5/2} - P_{3/2}$ atomic transition. Figure 7.16 shows the experimental results. The two data sets were obtained with the polarization of the 854 pumping beam set to σ^{+} (red squares) and σ^{-} (blue triangles) and the corresponding opposite polarizations in the single photon beam. The frequency of 0MHz in the horizontal axis corresponds to the central frequency of the $D_{5/2} - P_{3/2}$ transition, obtained by resonance fluorescence spectroscopy with the 854 laser,

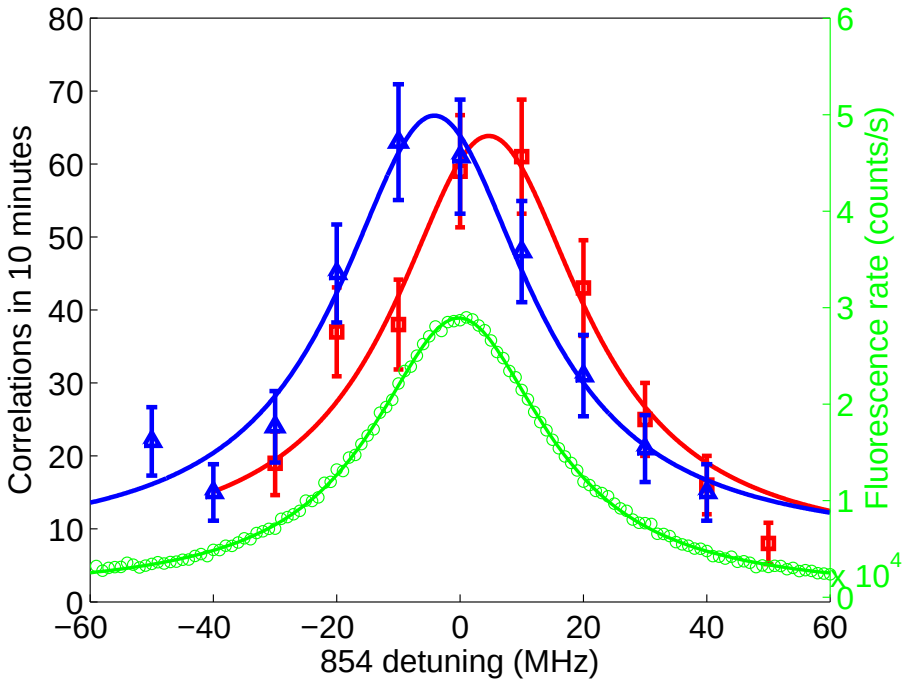

Figure 7.16.: Correlation spectroscopy with single photons. The rate of coincidences between absorption events and trigger photon detection is varied by controlling the central frequency of the filter cavities. Red squares (blue triangles) show data taken with the 854 nm pumping laser σ^+ (σ^-) polarized and the SPDC photons set to σ^- (σ^+). Each data point corresponds to the value of $g^{(2)}(\tau = 0)$ obtained after 10 minutes of acquisition. Poissonian error bars are also displayed. The center frequency of the $D_{5/2}$−$P_{3/2}$ transition is set to 0 MHz and deduced from fluorescence spectroscopy with a vertically polarized 854 nm laser and without optical pumping (green circles). Solid lines show least-squares Lorentzian fits to the data points.

plotted as green circles (see Section 7.2.2). Lorentzian fits on the data (solid lines) reveal that both spectra have a width of 40 MHz (FWHM), which fits well to the expected spectra obtained by convoluting the atomic linewidth (22 MHz) and the photon bandwidth (20 MHz). Furthermore, the two curves are displaced about the central frequency in opposite directions and have a full splitting of 8.8 ± 2.2 MHz. This shift is due to the different Landé g-factors of the $D_{5/2}$ and $P_{3/2}$ levels, which produce different Zeeman splittings of the outermost substates, and therefore a difference in frequency of the $\left|D_{5/2}; m = \{3/2, 5/2\}\right\rangle \leftrightarrow \left|P_{3/2}; \{1/2, 3/2\}\right\rangle$ transitions with respect to $\left|D_{5/2}; \{-3/2, -5/2\}\right\rangle \leftrightarrow \left|P_{3/2}; \{-1/2, -3/2\}\right\rangle$ transition. For a magnetic field of 5 Gauss, used in our experiments, the expected frequency shift is 12 MHz, in satisfying agreement with the experimental value. To calculate it we use the expression $\Delta E = \Delta E_{P_{3/2}, m_{5/2} \pm 1} - \Delta E_{D_{5/2}, m_{5/2}}$, where $\Delta E_{L_J, m} = \mu_B g_J(L_J) B m$

is the Zeeman splitting of level $|L_J, m\rangle$, μ_B is the Bohr magneton, $g_J(L_J)$ is the Landé g-factor of level L_J (see Figure 5.1), B is the applied magnetic field and $m_{5/2}$ is the initial Zeeman substate of the ion in the $D_{5/2}$ level. The plus (minus) sign is taken for a σ^+ (σ^-) transition. For the transitions we are considering ($\Delta m = \pm 1$), $\Delta E = \mu_B B \left[m \left(g_{P_{3/2}} - g_{D_{5/2}} \right) \mp g_{D_{5/2}} \right]$. Obviously, the shift depends on the initial Zeeman substate $m = m_{D_{5/2}}$ of the ion. However, the difference between the shift of levels $m = 3/2$ and $m = 5/2$ is around 10% of the absolute value, so it can be neglected.

To summarize, we have proven the transfer of time correlations present in SPDC photon pairs to the absorption event of one of the photons heralded by the detection of the corresponding partner photon. These experiments were first performed under continuous excitation conditions, and later under more controlled pulsed excitation conditions. The performed measurements of polarization and frequency dependence of the correlation rates showed that these parameters are well controlled in the system.

8. Conclusion and Outlook

This thesis has thoroughly described the construction, operation and characterization of a source of polarization entangled photon pairs suitable for their interaction with single trapped $^{40}Ca^{+}$ ions. It has also shown how it is possible to detect the interaction of single photons generated in this way with a single trapped ion, and has shown results proving this interaction and its quantum character.

The construction of the source took place in parallel to that of the ion traps, which are documented in other PhD theses [39, 46, 61]. It is important to note that the complete project started with two empty laboratories, out of which the combination of two ion traps and an entangled photon pair source were built. In addition, the development took place in a recently-born institute, with its unavoidable teething problems..

The necessary requirements for the source were satisfactorily fulfilled. The photon pairs it generates can be tuned to either of the two allowed transitions in $^{40}Ca^{+}$, namely $D_{5/2} \leftrightarrow P_{3/2}$ and $D_{3/2} \leftrightarrow P_{3/2}$ at 854 and 850 nm, respectively, and their frequencies can be stably kept on these transitions, in many cases for several hours. In addition, the bandwidth of the generated photon pairs was matched to the atomic transition linewidth of 22 MHz, which is a strong requirement for a source of photons based on SPDC. The observed rates of photons produced at this bandwidth was of the order of 5 pairs (coupled into a single-mode fiber) per second per miliwatt of pump power. As the pump laser was chosen to provide a significantly high power of up to 100 mW, which resulted in up to 60 mW of available pump power at the crystal, the rate of pairs resonant with the ion could reach a value of up to 300 pairs/s.

Methods to detect the moment of absorption of a photon by the ion were discussed in Chapter 5. Programming the data analysis software to apply these methods and optimize the parameters implied a significant effort of this project.

The connection of the source to the ion trap system was also a major challenge. To optimally couple the fiber from which the SPDC photons emerged to the single trapped ion and to tune the central frequency of the SPDC photons to the atomic transition required developing adequate alignment and spectroscopy techniques.

The ion trap setup can be improved for experiments with the source. One idea, although somewhat technically difficult, would be to implement a resonant optical cavity around the ion, to enhance the interaction efficiency.

Experiments with the combined setup proved the feasibility of coupling a single ion to an quantum light source. With the current experimental parameters we observed the interaction of single SPDC photons by a single ion, correlating the absorption events with the detections of the corresponding partner photons. We also showed that we can control the polarization of the SPDC photons from the point

where they are produced to the ion location, and observe the full polarization dependence of the absorption event. This is important for the next step, in which the quantum state of the photon, encoded in its polarization, is transferred to the internal state of the ion.

We believe that these results represent more than a substantial technical achievement. Indeed, the interaction of single photons with a single atom is at the heart of quantum optics and has never been realized with this level of control before. Furthermore, these results provide insight for transforming this system into a useful tool for quantum information processing purposes. The crucial necessary next step is to transfer the polarization state of one of the photons to the internal state of one trapped ion. This allows to entangle the internal state of one trapped ion with the polarization state of the remaining photon. By pushing this idea further, the state of the second photon is transferred to a second distant trapped ion, hence providing a new technique to entangle two distant qubits. In this chapter we give a brief survey of some ideas to work towards this direction. We first show a possible scheme to transfer the polarization state of the photon to the internal state of the ion. We then discuss some technical improvements which are probably necessary before this scheme is feasible.

The detection of the interaction was very efficient thanks to a scheme based on the observation of a quantum jump at the moment in which the ion absorbs a photon, which gives almost unity probability to detect the event. This trick allows to observe the rare events of absorption of photons from the source. The best achieved rate was of the order of 1 absorption per second with a source brightness of the order of 4 photons pairs /(s $\times$ mW $\times$ MHz), resulting in a typical rate of 4000 pairs/s in the 22 MHz bandwidth of absorption of the ion. The corresponding rate of absorptions correlated with a detection of a trigger photon was of the order of 0.1 s^{-1}. These will be taken as reference values to assess the feasibility of more advanced schemes.

8.1. Entanglement swapping scheme

Entanglement swapping schemes rely on the possibility of mapping the polarization state of the photon onto the internal state of the ion. In particular, an arbitrary photon state $|\Psi_p\rangle = \alpha|\uparrow\rangle + \beta|\downarrow\rangle$ must be transferred to the state $|\Psi_i\rangle = \alpha|+\rangle + \beta|-\rangle$, where $|\uparrow\rangle$, $|\downarrow\rangle$ are two arbitrary polarization basis vectors, and $|+\rangle$, $|-\rangle$ represent an atomic qubit pair of states. In this scheme, they are chosen to be $|\pm\rangle = \left|S_{1/2}, m = \pm 1/2\right\rangle$.

The proposed state transfer scheme is illustrated in Figure 8.1. The ion is manipulated with a periodic laser pulse sequence consisting of three main phases. It is first laser cooled by means of the 397 and 866 nm lasers as usual. Then, the ion is prepared in a symmetric superposition of the states $\left|D_{5/2}, m = \pm 1/2\right\rangle$ by means of the sequence of three pulses. First, a σ^- polarized 397 beam pumps the ion to the $\left|S_{1/2}, m = -1/2\right\rangle$ state. Then, a bichromatic 729 nm $\pi/2$-pulse converts this state into the desired superposition of $\left|D_{5/2}, m = \pm 3/2\right\rangle$. The pulse must contain a coherent superposition of the two frequencies coupling $m_S = -1/2 \leftrightarrow m_D = 3/2$ and

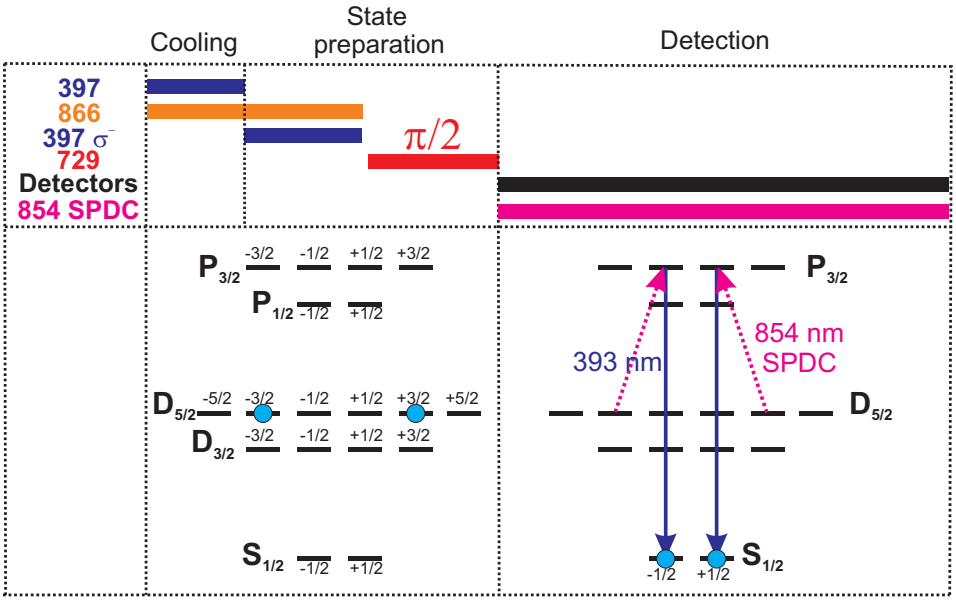

Figure 8.1.: Scheme for transferring the polarization state of an 854 nm SPDC photon to the magnetic levels of the $S_{1/2}$ ground state of a single $^{40}Ca^{+}$ ion.

$m_S = -1/2 \leftrightarrow m_D = -3/2$. Note that for this $|\Delta m| = 2$ transitions are required, which is possible thanks to the quadrupole character of the S-D transitions.

At this point, the PMT detectors monitoring the 393 nm photons are gated on. Upon the absorption of an SPDC photon prepared in an arbitrary state $|\Psi_p\rangle = \alpha|H\rangle + \beta|V\rangle$, the ion undergoes a Raman transition to the ground state emitting a 393 nm photon which can be detected by the PMT, thus heralding the absorption event. The process is essentially coherent as long as it remains impossible to determine which $P_{3/2}$ Zeeman substate the ion decays from. This condition holds if the Zeeman splitting between these two levels is lower than the transition linewidth of 22 MHz, which can be achieved for a low enough value of the biasing magnetic field.

The efficiency of this scheme is substantially reduced with respect to the experiments performed in this thesis, due to the inefficiency of detecting the single 393 nm photon heralding the absorption event, compared to the close-to-unity probability of detecting the absorption event with the quantum jump scheme. As shown in section 7.2.3, the probability of detecting a single 397 nm photon is of around 1%. Therefore, the efficiency of detecting the interaction event in this scheme is 100 times lower than in the quantum jump schemes performed in this thesis. This implies that, for example, the rate of detected correlations between an absorption event and a trigger photon for the two schemes are related by $R_{st} = R_{qj}/100 = 0.001s^{-1}$, being $R_{qj} \sim 0.1s^{-1}$ the rate of correlations for the quantum jump scheme

and R_{st} the rate of correlations for the state transfer scheme.

A second important problem in this scheme arises from the background clicks detected by the PMTs. As seen in all the experiments we performed, it is hard to reduce the background clicks per PMT to a value below 250 counts/s. These counts come from detector dark counts (∼100 c/s) and stray light (150 c/s). Even if stray light is fought against, the residual 200 dark counts per second from both detectors combined are unavoidable. At most, one could try to optically combine the beams from both HALOs into a single detector without appreciable losses and reduce the background to 100 c/s. In any case, these rates are 100-500 times higher than in the quantum jump schemes, in which background arose only from spontaneous decay events from $D_{5/2}$ to $S_{1/2}$ (τ = 1.2 s), which also produce quantum jumps.

However, this scheme does improve the time resolution of the absorption event. In the quantum jump scheme, the absorption event could be determined with a precision of the order of the inverse of the fluorescence rate, which at best could be around $2\mu s$. Now, the resolution is given by the time spread of the single 393 nm fluorescence photon emitted when the ion absorbs an SPDC photon, given by $1/\Delta\omega = 1/(2\pi \times 22\ \mathrm{MHz})$ = 7.2 ns.

Assuming that we set the coincidence window in each scheme to these values, the rate of accidental coincidences for each scheme is $B_{qj} = 1\mathrm{s}^{-1} \times 1000\mathrm{s}^{-1} \times 2\mu\mathrm{s} = 10^{-3}s^{-1}$ and $B_{st} = 500\mathrm{s}^{-1} \times 1000\mathrm{s}^{-1} \times 7\mathrm{ns} = 5 \times 10^{-4}s^{-1}$. As a result, the signal-to-noise ratio (SNR) of each scheme, assuming the same conditions for both experiments, are $SNR_{qj} = R_{qj}T/\sqrt{B_{qj}T} \sim 3\sqrt{T}$ and $SNR_{st} \sim 0.09\sqrt{T}$. To have a SNR of 10 in the state transfer scheme, we need an acquisition time of at least 10^4 s, for which we would obtain 20 real correlations with 4 accidentals. This experiment is still feasible but unpractical for quantum information processing purposes.

In an experiment where the second photon is absorbed by a second ion, the rate of correlations (coincident absorptions of the two photons in a pair by each ion) would be of the order of $R_c = 1 \times 10^{-8}s^{-1}$. This makes these experiments completely unfeasible under the current conditions.

It is then clear that for more advanced experiments the experimental conditions have to be improved. There are two main working directions to improve the rate of successful events: to improve the interaction efficiency of the photon with the ion and to enhance the source brightness.

To improve interaction efficiency of the photon with the ion there are two options. The first is to implement a Fabry-Perot cavity around the ion such that each photon performs multiple passes through the atom. A simple version of this is to place a single mirror behind the back HALO, reflecting only once the photon back into the ion trap. In this way it is easy to obtain a factor of 2 in the absorption efficiency. A factor of 4 enhancement could even be achieved if the distance of this mirror to the ion is actively stabilized such that the incoming photon interferes constructively with itself at the position of the ion, as was shown in Innsbruck experiments [68]. The second option to enhance the interaction efficiency is to increase the numerical aperture of the optics used to focus the photon onto the ion. This could be done either by a lens with a higher numerical aperture [33] or, in the spirit of the work from the Erlangen group [34], by placing a parabolic mirror around

the ion trap such that the ion is located in its focus. Along this line, the Erlangen group is studying the possibility of achieving close to 100% absorption efficiency by mapping the spatio-temporal mode of dipole absorption to the incoming gaussian mode. This requires matching the fields (amplitude, phase and polarization) of the two modes and their spectral distributions.

8.2. Source improvements

The brightness of the single pass down-conversion source can be substantially improved by implementing cavity enhancement. In this section, several design options will be discussed and the expected enhancement factors will be estimated. In the following section we will give more detail on the design parameters.

8.2.1. Cavity enhancement of down-converted photons

Cavity enhanced down-conversion has been implemented by several groups. Two different approaches can be found in the literature: to enhance the pump power by placing the crystal inside a cavity resonant with the pump [69], or to enhance the spectral distribution of the generated photon pairs conveniently, by placing the crystal inside a cavity resonant with the generated infrared photons [70, 71, 72, 73, 74].

In the first stages of the source design, we started considering the first idea. We designed and constructed a cavity resonant with 425 nm. However, our PPKTP crystal turned out to be quite lossy at this wavelength (20% loss per pass), so the finesse of the resulting cavity could not get better than 30. In fact, to achieve good incoupling efficiency into the cavity, the impedance matching condition (Equation A.0.6) had to be satisfied, so the incoupling mirror had a transmission coefficient of around 80%. This limited the resulting maximum cavity finesse to around 15. The resulting circulating intracavity power gain, given by the square of expression A.0.1, was around 5, for a bow-tie cavity, and 2.5 for a linear Fabry-Perot cavity. Hence, the achievable enhancement factor does not pay off the large technical effort required to implement this cavity.

The high losses of the crystal observed at 425 nm were a bit unexpected. KTP crystal manufacturers do not usually report absorption coefficients at this wavelength, and they typically specify their crystals to be transparent in a window from 350 nm to 3.5 μm, being 350 nm the bandgap wavelength of KTP. The losses may be explained by the fact that we are working close to this bandgap wavelength and they can be enhanced by the presence of impurities and imperfections in the crystal structure. In any case, it quickly became clear that the better strategy would be to realize cavity enhancement resonant with the generated photon pairs, for which the cavity losses are much lower.

Cavity enhancement in the infrared consists in placing the crystal inside a cavity resonant with both the down-converted signal and idler modes, at 850 or 854 nm in our case. The pump beam generates photons pairs randomly as in the single-pass

case. However, due to the presence of the cavity the spectral intensity of generated pairs increases at the frequency intervals which are on resonances with the cavity and is suppressed in the off-resonant frequency regions. The total generated power of photon pairs, obtained as the integral of the spectral intensity, must be conserved with respect to the single-pass case. However, the intensity spectrum presents peaks at the resonances which have a total power, obtained as the integral of the intensity spectrum around a peak, which is higher than the corresponding single-pass power in the same frequency bandwidth by a factor given by the cavity finesse.

This type of enhancement mechanism has several advantages with respect to the pump cavity enhancement. First, the crystal losses in the infrared (850 and 854 nm) are much lower than in the blue, so the achievable cavity finesse, and therefore the enhancement factor, is much higher. Second, the photon pair generation is restricted to a single spatial cavity mode, so the photon pairs transmitted by the cavity can be coupled into single-mode fibers with high efficiency.

The technique also has some drawbacks: 1) to achieve a good enhancement, both signal and idler modes have to be resonant at the same cavity length. This is automatic in Type-I down-conversion. However, in Type-II the crystal birefringence produces a phase shift of the signal with respect to the idler which may destroy the double resonance condition. 2) The two photons of one pair can escape the cavity after a different number of round-trips. However, both photons leave the cavity with high probability within twice the cavity decay time and this is displayed in the spectral distribution of photon pairs as an envelope function with a linewidth corresponding to the cavity decay rate. The presence of the enhancement cavity also contributes to the spectrum by adding additional peaks (or modes) displaced from the central peak (at the degenerate frequency) by multiples of the free spectral range. These higher order modes can be removed by means of an additional spectral filter outside of the cavity resonant with the degenerate frequency, such as the system implemented in our setup. 3) The need of this additional filter represents an additional drawback, although in our case the system is already implemented. It would actually be possible to use only one of the cavity filters (the broadband cavity) because the narrow-band filtering is performed by the enhancement cavity itself. 4) The double resonant cavity has to be locked to the frequency of the generated photon pairs. To do this, a laser beam of the same frequency as the photons has to be coupled into the cavity. It is necessary to avoid that this locking beam is mixed with the signal and idler modes, and this can only be done by alternating the locking periods and emission periods using an optical chopper, in the same fashion as the locking system for our filtering cavities. Under the current development of the setup, all these drawbacks are relatively easy to solve.

There are several strategies to recover the double resonance condition. First of all, it is possible to find a crystal temperature such that the signal photon (assuming e.g. it is H polarized) is resonant with one cavity mode and the idler photon (V polarized) is resonant with a different cavity mode. This is always possible thanks to the difference of the thermo-optic coefficients along two different axes of the crystal. However, it might be that the corresponding temperature differs from the

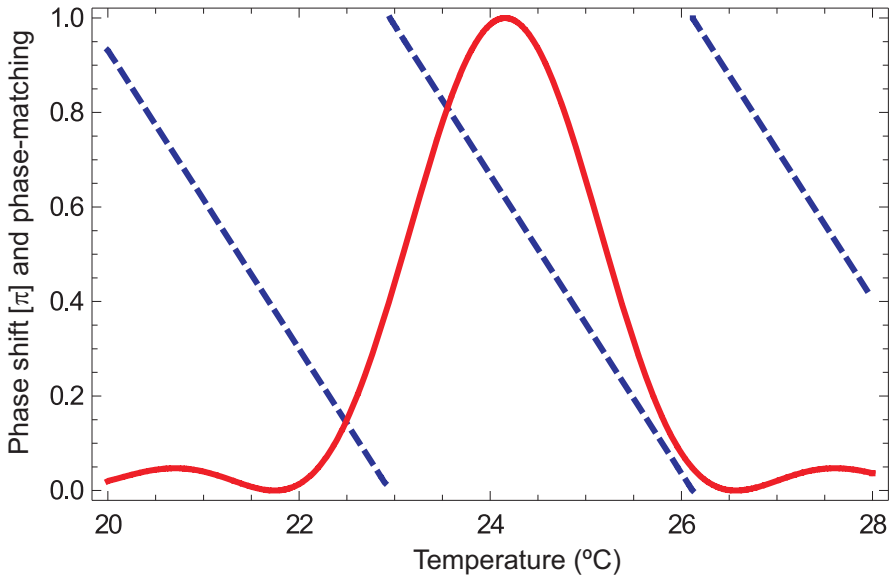

Figure 8.2.: Phase matching condition for degenerate photon pairs (solid red curve) and relative phase shift between the two polarizations (blue dashed curve) as a function of temperature, showing that it is likely to achieve both conditions simultaneously. A 2 cm long PPKTP crystal was considered and the Sellmeier formulas from reference [50] were used (see Appendix C).

crystal phase-matching temperature at the desired wavelength. This is illustrated in Figure 8.2 where the phase matching efficiency for degenerate photon pair generation and the relative phase shift produced by the crystal on the two photons is plotted as a function of temperature. For an interval of $2°C$ variation of the crystal temperature, the phasematching efficiency varies within its FWHM while the phase difference varies by 0.67π. It would then be possible, with a probability of 67%, that both conditions are satisfied simultaneously in our setup. To guarantee that the double resonance condition can be always satisfied, a full phase variation of π should be possible; this could be achieved with a slightly higher sacrifice in phase-matching efficiency.

A further step to accomplish the double resonance condition (in the unfortunate cases that it is not achieved varying the temperature of the crystal within the FWHM of the phasematching curve) would be to insert to the cavity an extra birefringent element, such as a calcite crystal or a piece of KTP, with an independent temperature controller. This would allow to vary the phase shift independently without varying the phase-matching condition.

A second KTP crystal grown together with the PPKTP crystal, thence having exactly the same optical properties, with half the length of the latter and placed inside the cavity rotated by $90°$ about the propagation axis would cancel completely the phase shift produced in the PPKTP crystal. This setup is convenient in applications

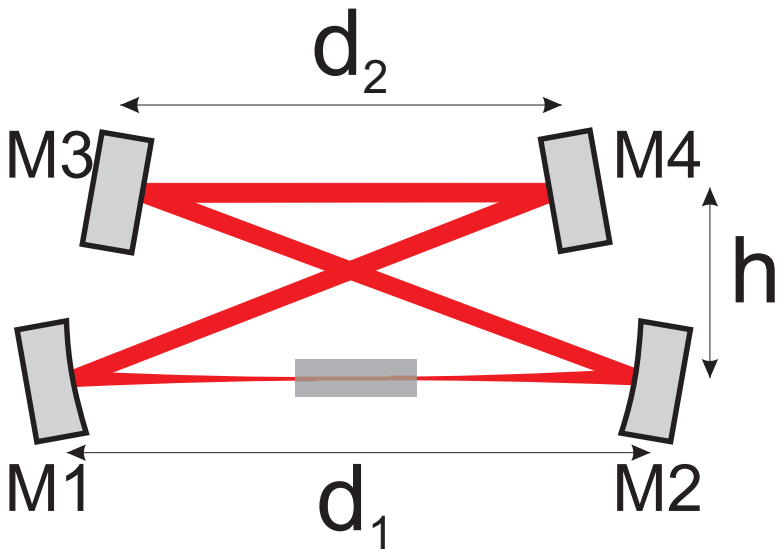

Figure 8.3.: Proposed scheme for setting up the SPDC enhancement cavity. Mirror M2 is the outcoupler, whose reflectivity is a parameter in the calculations that follow.

where the full multimode broadband emission spectrum is used and no additional external frequency filters are used [72, 71, 73]. In such cases, this full phase shift cancelation is the only way to obtain polarization entangled photon pairs, because otherwise the polarization state of each photon could be distinguished by its emission time. However, if additional external filtering is to be used, as in our case, this effect is not a problem and full phase shift cancelation is not necessary.

8.2.2. Design of a down-conversion enhancement cavity

For completeness, in the following we present our design of the enhancement cavity for future reference.

The parameters which constrain our design are the following: 1) the linewidth of a single emission mode of the cavity should be lower than the atomic linewidth of 22 MHz. 2) The finesse should be as high as possible to achieve the maximum enhancement factor. 3) The probability that the photons escape from the cavity, as opposed to being lost inside it, should be as high as possible. This condition contradicts condition 2, so a tradeoff has to be established. 4) The spatial geometry of the cavity should be such that the cavity mode has a waist corresponding to the optimum down-conversion collection mode of the order of 25μm.

The geometry we are considering is shown in Figure 8.3. The bow tie cavity configuration is advantageous with respect to the linear cavity due to the fact that in the former the losses per round trip are essentially 50% lower than in the latter (the beam passes twice through the crystal per round trip in the linear cavity), and thus the finesse is a factor of two higher. The cavity we are considering has concave

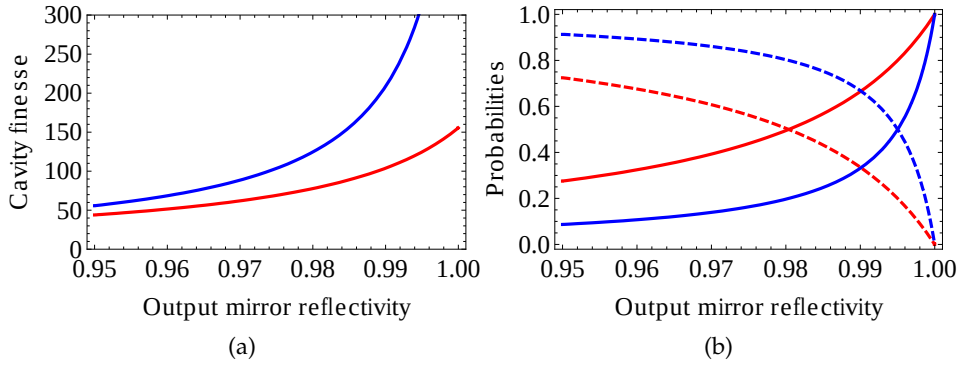

Figure 8.4.: (a) Cavity finesse as a function of the output coupler reflectivity for a crystal with 2% losses (red curve) and a crystal with 0.5% losses (blue curve). (b) Probabilities for a down-converted photon to be lost in the crystal for 2% crystal loss (blue solid curve) and 0.5% loss (red solid curve), and the respective probabilities for the photon to be emitted by the output coupler (dashed curves).

mirrors M1 and M2 with the same radii of curvature R and two plane mirrors M3 and M4 to close the beam path. Mirrors M1 and M2 are made with antireflection coatings for the blue beam, such that it is incoupled through mirror M1 with high efficiency, passes once through the crystal and leaves the cavity through mirror M2.

To obtain the cavity parameters, the crystal losses must be known. We measured them to be 2% per pass. This value, although still surprisingly high for the infrared, is sufficiently small to obtain a decent cavity.

In a first calculation, we estimate the cavity finesse and the photon escape probability, i.e. the probability that the photons leave the cavity through the outcoupling mirror, as opposed to being lost in the crystal or in another mirror of the cavity. The finesse is essentially given by expression A.0.11, or a modification of expression A.0.12 taking into account the losses in the crystal, to give $F = \frac{2\pi}{1-T_c+T_2}$, where T_c is the transmission coefficient of the crystal and T_2 is the outcoupling mirror transmission. We have neglected optical losses in all mirrors and transmission in mirrors other than the outcoupler. The probability that a photon in a pair generated in the crystal escapes the cavity after n roundtrips is $P_e(n) = (R_2T_c)^nT_2$. Similarly, the probability that it is lost in the crystal after n round trips is $P_l(n) = (1-T_2)^nT_c^(n-1)(1-T_c)$. Summing for all number of round trips, we obtain the total escape probability $P_{esc} = (1-R_2)/(1-R_2T_c)$ and the total loss probability respectively $P_{loss} = R_2(1-T_c)/(1-R_2T_c)$. The cavity finesse and the photon escape probability as a function of the output coupler reflectivity (assuming it is lossless) are plotted in figures 8.4a and 8.4b.

A tradeoff between cavity finesse and photon escape probability must be established. For our 2% lossy crystal, an output coupler reflectivity of 98% sets the finesse to 78 and the escape probability to 50%. It would certainly be advantageous to replace the crystal by a less lossy one.

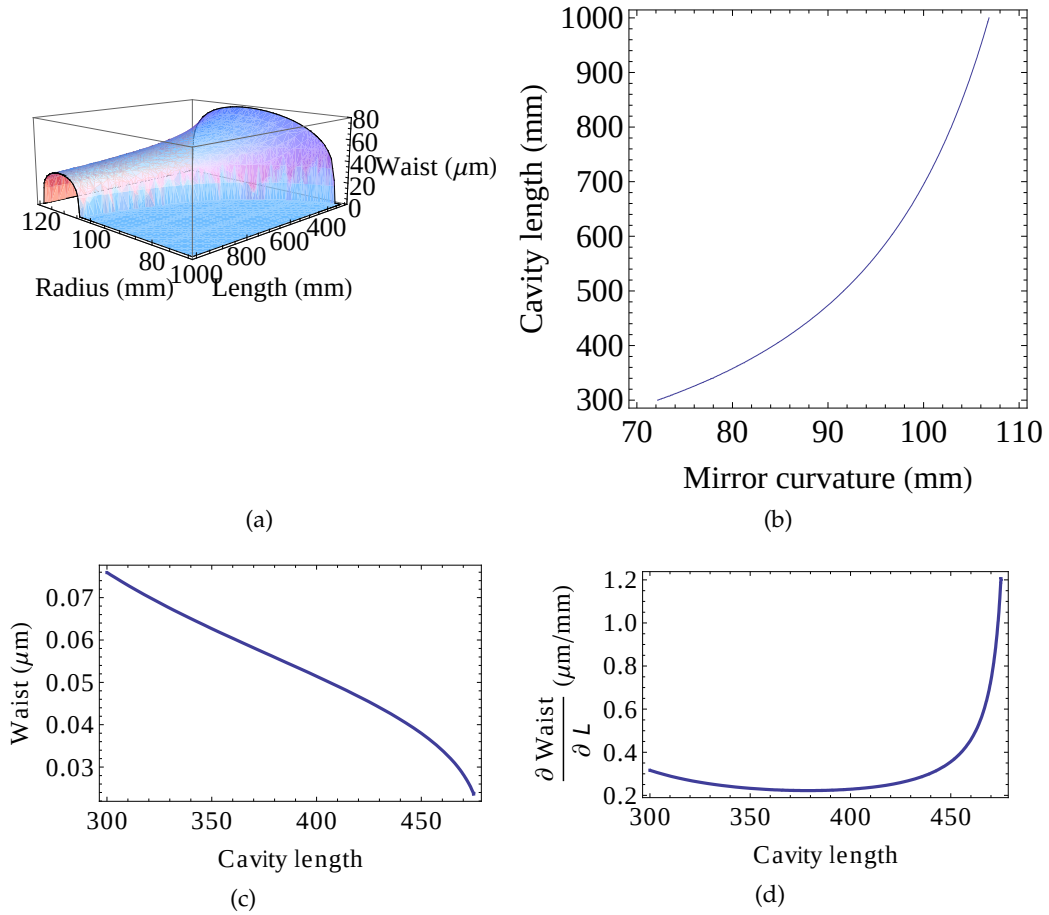

Figure 8.5.: Analysis of the mode geometry for a bow-tie cavity. We consider a cavity with d_1 = 120 mm. (a) Waist diameter as a function of the radius of curvature of the mirrors and the length of the cavity. (b) Graph of the cavity length vs mirror radius of curvature to achieve a waist of 25 μ m. (c) Waist diameter 5 as a function of the cavity length, for mirrors with 90 mm radii. (d) Derivative of the waist diameter with respect to cavity length as a function of the cavity length for the same mirrors as in (c)

The next thing to consider are the spectral properties of the cavity. Given the finesse F of the cavity, and an upper limit for the desired linewidth $\delta\nu < \delta\nu_0 =$ 22 MHz, we obtain a lower limit for the length of the cavity $L > c/(2F\delta\nu_0)$. Taking a value of $F = 78$, we obtain $L > 8.7$ cm, which is easy to fulfill.

The most difficult specification to fulfill is the waist of the resonator mode at the crystal position, which should be close to the optimum range of values used in single-pass down-conversion: 20-30μm. The free available parameters are the mirror curvatures and the lengths d_1, d_2 and h of the cavity. To obtain the eigenmode of the cavity we obtain the gaussian beam parameter q which reproduces itself after one round trip in the cavity, $q = (Aq + B)/(Cq + D)$, where A, B, C and D are the

elements of the matrix representing the optical system. This can be done using the utilities included in the OpticsTools package described in Appendix B. We consider a system with mirrors $R_1 = R_2 = R$, and M3 and M4 plane mirrors.

The results of the analysis are shown in Figure 8.5. In (a), the cavity mode waist diameter is plotted as a function of the radius of curvature of mirrors M1 and M2, and the cavity length. Solving for a waist of 25 μm we obtain the curve in (b) for the corresponding mirror radius as a function of the cavity length.

In panels (c) and (d), the radii of mirrors M1 and M2 are taken to be 90 mm. The cavity waist as a function of the cavity length (c) shows that the latter has to be of around 470 mm. Note that the cavity is close to the limit of stability for this waist size. The cavity is unstable for $L > 480$mm. To assess how robust such a cavity (with L = 470mm) would be, we calculate the variation of the cavity waist per unit of variation of the cavity length (d). At a value of L = 470 mm, we obtain a safe variation of around 1μm/mm. At the cavity stability limit, this variation goes to infinity.

In conclusion, with this design and the aforementioned experimental parameters, we would achieve an enhancement cavity with a finesse of around 80, a free spectral range of around 320 MHz, a linewidth of about 4 MHz, and a photon escape probability of 50%. This value of the finesse would increase the rate by two orders of magnitude, compensating the two orders of magnitude of loss in efficiency of the entanglement transfer scheme with respect to the quantum jump-based single-photon absorption scheme.

A. Cavity filters

In the source, the narrowband filter matching the ion absorption spectrum is achieved using two mirror Fabry-Perot resonators. Here we give a brief analysis of two mirror resonator theory with a gaussian optics approach. A full survey can be found in [67].

Consider a resonator with two mirrors M_1 and M_2 with field reflectivities $r_1 = \sqrt{R_1}$ and $r_2 = \sqrt{R_2}$, and transmittivities $t_1 = i\sqrt{T_1}$ and $t_2 = i\sqrt{T_2}$, respectively. R_1 and R_2 are the power reflection coefficients, while T_1 and T_2 are the power transmission coefficients, which are usually used to specify mirrors. In addition, each mirror has power loss coefficients given by L_1 and L_2. Let E_i be the electric field incident upon mirror M_1, E_c the circulating power inside the cavity right after mirror M_1 and E_t the transmitted field at the output of mirror M_2. In the steady state, these fields obey the condition that $E_c = it_1E_i + g_{rt}(\omega)E_c$, or

$$\frac{E_c}{E_i} = \frac{it_1}{1 - g_{rt}(\omega)}, \tag{A.0.1}$$

where $g_{rt}(\omega)$ is the round trip cavity gain or loss, given by

$$g_{rt}(\omega) = r_1 r_2 \exp\left(-\alpha 2L + i\frac{\omega}{c}2L\right) \tag{A.0.2}$$

for a linear two-mirror passive cavity of length L filled with a medium of absorption coefficient α. The ratio between the transmitted and incident fields is

$$t(\omega) = \frac{E_t}{E_i} = \frac{-t_1 t_2 \exp\left(-\alpha L/ + i\frac{\omega}{c}L\right)}{1 - \exp\left(-\alpha 2L + i\frac{\omega}{c}2L\right)} = -\frac{t_1 t_2}{\sqrt{r_1 r_2}} \frac{\sqrt{g_{rt}(\omega)}}{1 - g_{rt}(\omega)}. \tag{A.0.3}$$

If the cavity is symmetric, with $t_1 = t_2 = t$ and $r_1 = r_2 = r$, and contains a lossless medium with $\alpha = 0$, this can be written as:

$$t(\omega) = \frac{t^2 e^{i\frac{L\omega}{c}}}{1 - r^2 e^{i\frac{2L\omega}{c}}}. \tag{A.0.4}$$

Similarly, the reflected field is

$$\frac{E_r}{E_i} = r_1 - \frac{t_1^2}{r_1} \frac{g_{rt}(\omega)}{1 - g_{rt}(\omega)}. \tag{A.0.5}$$

The intensity ratios I_t/I_i and I_r/I_i are just the square moduli of these expressions. We now assume that the cavity medium loss is negligible compared to the mirror losses. It is then easy to show that the reflected power on resonance reaches a minimum when

$$R_1 = (L_1 - 1)^2 R_2. \tag{A.0.6}$$

This condition is known as impedance matching and it must be fulfilled in the design of any good cavity filter. In addition, the transmitted power ratio on resonance is

$$\frac{I_t}{I_i} = \frac{(-L_1 - R_1 + 1)(-L_2 - R_2 + 1)}{\left(1 - \sqrt{R_1}\sqrt{R_2}\right)^2}. \tag{A.0.7}$$

This expression is maximized when condition A.0.6 holds and additionally when

$$L_1 = L_2 = 0, \tag{A.0.8}$$

that is, for lossless mirrors. Under these conditions the cavity transmission on resonance is 100%. In practice it is very hard to produce completely lossless and equal mirrors, so the transmission efficiencies are typically around 90%.

The transmission spectrum of the cavity, given by A.0.3, is a periodic peak structure with a spacing between peaks, known as the free spectral range (FSR), of

$$FSR = \frac{c}{2L}. \tag{A.0.9}$$

Each peak has a finite width, the so called cavity transmission bandwidth, with a FWHM value given by

$$\delta\nu_{FWHM} = \frac{1 - g_{rt}(0)}{\pi\sqrt{g_{rt}(0)}}\frac{c}{2L}. \tag{A.0.10}$$

The finesse of the cavity is

$$\mathfrak{F} = \frac{\pi\sqrt{g_{rt}(0)}}{1 - g_{rt}(0)} = \frac{FSR}{\Delta\nu_{FWHM}}, \tag{A.0.11}$$

and determines the spectral resolving power of the filter. A more practical expression in terms of mirror transmission and loss coefficients $T_n, L_n \ll 1$ is

$$\mathfrak{F} \approx \frac{2\pi}{T_1 + L_1 + T_2 + L_2}. \tag{A.0.12}$$

Expression A.0.3 for the cavity transmission spectrum can be further simplified by assuming that the frequency is close to one of the cavity resonances, at $\omega_n = \frac{2\pi nc}{2L}$. We then define $\omega = \omega_n + \Omega$ and expand the exponentials in A.0.4 to first order in Ω around ω_n. After some algebra we arrive at the expression

$$t(\omega) = \frac{t^2/(1 - r^2)}{1 - i\frac{2\Omega}{\delta\omega}}, \tag{A.0.13}$$

where $\delta\omega/2\pi = \delta\nu_{FWHM} = FSR/\mathfrak{F}$ is the cavity linewidth, and $\mathfrak{F} = \pi\frac{r}{1-r^2}$ is the cavity finesse. This expression was particularly useful in the derivation of the $G^{(2)}$ correlation function of the filtered down-conversion pairs in section 2.1.3.

We now consider the geometrical properties of an optical cavity composed of two spherical mirrors. The two mirrors M_1 and M_2 have radii of curvatures R_1 and R_2. The curved surface is concave (as seen from inside the cavity) for positive radii. A beam whose wavefront matches the mirror curvature at each mirror will

obviously reproduce itself after each roundtrip, and will therefore be an eigenmode of the resonator. Such property is satisfied by a gaussian beam, which has spherical wavefronts given by

$$R(z) = z + \frac{z_R^2}{z} \tag{A.0.14}$$

whereby z_R is the Rayleigh range of the beam and z is the longitudinal position along the optical axis. The gaussian beam that fits into a cavity with mirror M_1 at position $z = z_1$ and M_2 at $z = z_2$ satisfies $R(z_1) = -R_1$ and $R(z_2) = R_2$. The negative sign comes in because of the convention that a convergent gaussian beam propagating to the right has a negative curvature, whereas the corresponding curvature of mirror M_1 would be positive. A third equation is given by the fixed length of the cavity being $L = z_2 - z_1$. Solving for z_R we obtain

$$z_R^2 = \frac{g_1 g_2 (1 - g_1 g_2)}{(g_1 + g_2 - 2 g_1 g_2)^2} L^2, \tag{A.0.15}$$

where $g_i \equiv 1 - L/R_i$. The Rayleigh range is related to the width of the beam at the focal point, or waist w_0, as

$$w_0 = \sqrt{\frac{\lambda z_R}{\pi}}. \tag{A.0.16}$$

We can also solve for the mirror positions z_1 and z_2:

$$\begin{aligned} z_1 &= \frac{g_2(1 - g_1)}{g_1 + g_2 - 2 g_1 g_2} L \\ z_2 &= \frac{g_1(1 - g_2)}{g_1 + g_2 - 2 g_1 g_2} L. \end{aligned} \tag{A.0.17}$$

The stability criterion for this type of cavity is

$$0 \leq g_1 g_2 \leq 1. \tag{A.0.18}$$

We will consider two cases: a symmetric bi-concave cavity, with $R_1 = R_2 \equiv R > 0$, and a plano-concave cavity, with $R_1 > 0$ and $R_2 \to \infty$. For the first case, the stability condition reads $|1 - L/R| < 1$, or $R \geq L/2$. A cavity at the stability limit $R = L/2$ is said to be concentric. A cavity with $R = L$, which is clearly stable, is termed confocal. In the second case of interest, the plane mirror has $R_2 \to \infty$, and the stability condition simplifies to $1 - L/R_1 \geq 0$, or $R_1 \geq L$. This is equivalent to the first case since the plane mirror generates a specular image of the concave mirror, effectively producing a bi-concave cavity of twice the length.

A set of eigenmodes supported by the cavity are the so called Hermite-Gaussian modes, usually specified as TEM_{mn}. They are solutions to the wave equation in the paraxial approximation with spherical mirror boundary conditions and form a complete set of orthogonal functions with which any paraxial radiation field can be

expanded. They are expressed as

$$\begin{aligned} E_{m,n}(x,y,z) = E_0 \frac{w_0}{w(z)} \\ &\times H_n\left(\sqrt{2}\frac{x}{w(z)}\right)\exp\left(-\frac{x^2}{w(z)^2}\right) \\ &\times H_m\left(\sqrt{2}\frac{y}{w(z)}\right)\exp\left(-\frac{y^2}{w(z)^2}\right) \\ &\times \exp\left\{-i\left[kz-(1+n+m)\arctan\frac{z}{z_R}+\frac{k(x^2+y^2)}{2R(z)}\right]\right\}. \end{aligned} \quad \text{(A.0.19)}$$

H_n are the hermite polynomials of order n, $R(z)$ is the curvature of the wavefronts, given by expression A.0.14, while $w(z)$ is the beam spot size at axial position z, given by

$$w\left(z\right) = w_0\sqrt{1+\left(\frac{z-z_0}{z_R}\right)^2}. \quad \text{(A.0.20)}$$

The lowest order mode, with $mn = 00$, is the usual gaussian beam, given by

$$E(x,y,z) = E_0\frac{w_0}{w(z)}\exp\left(-\frac{r^2}{w(z)^2}\right)\exp\left\{-i\left[kz-\arctan\frac{z}{z_R}+\frac{kr^2}{2R(z)}\right]\right\}. \quad \text{(A.0.21)}$$

In A.0.19, the phase on axis ($x = y = 0$) differs from the usual plane wave phase kz by a term $(m+n+1)\arctan(z/z_R)$, which is the so called Gouy phase shift; it depends on the mode numbers m, n. As a consequence, the resonance frequency for a given cavity length, or the resonant cavity length for a given laser frequency varies with the mode number. The resonance condition requires that the overall phase shift after one round trip should be a multiple of 2π. For the TEM$_{mn}$ mode this implies

$$\frac{\omega}{c}2L-(1+n+m)2\arccos\pm\sqrt{g_1g_2} = 2\pi q. \quad \text{(A.0.22)}$$

Here the plus sign is to be used if $g_1, g_2 > 0$, and the minus sign if $g_1, g_2 < 0$. q is the axial mode number. The mode with axial or longitudinal number q and transverse numbers m, n is usually specified as TEM$_{m,n,q}$. The resonant length for each mode is in general different, unless the cavity is confocal. Expression A.0.22 provides a precise method of measuring the cavity length if the mirror curvature is known, which has been used in 3.5.3.

Since the Hermite-Gaussian modes form a complete basis set, the beam incident into the cavity filter can be expanded as a series of these modes as

$$E_i(x,y) = \sum_{m,n} c_{m,n}E_{m,n}(x,y). \quad \text{(A.0.23)}$$

The coefficients $c_{m,n}$ are obtained by the overlap integrals of the incident beam $E(x,y)$ with the corresponding mode (propagated to the outside through the incoupling mirror). Now if the cavity length is such that it is resonant with the TEM$_{m,n,q}$

mode, then all other transverse modes will in general be off resonant and will be entirely reflected by the cavity. All the components of $E_i(x, y)$ which are not resonant will be lost. This is why it is very important to make $E_i(x, y)$ as similar as possible to a single TEM mode, that is, to mode-match the input beam to a single cavity eigenmode. The easiest mode to achieve is always $TEM_{0,0}$, which is a gaussian beam.

The gaussian beam, whose electric field is given by expression A.0.21, can be described in a simpler way by means of the so-called complex beam parameter $q = z_0 + iz_R$. Here, z_0 is the position of the waist of the beam and z_R is its Rayleigh range, related to the beam waist diameter by expression A.0.16. The usefulness of this parameter lies in the simplicity of the rule describing its transformation by an optical element. Given the ray transfer matrix $\begin{pmatrix} A & B \\ C & D \end{pmatrix}$ of the optical element, the output beam parameter, in terms of the input beam parameter q, is $q_{out} = \frac{Aq_in+B}{Cq_in+D}$. The transfer matrix for different elements can be found elsewhere [67, 75].

B. Gaussian beam calculations toolkit

This appendix presents a brief introduction and user manual to the gaussian beam calculation toolkit developed during this PhD project. The toolkit consists of a Mathematica® library of functions with several features useful to analyze optical systems. The main tasks it allows are to define an optical system, define a beam according to its physical parameters, calculate and plot the propagation of the beam through the system, calculate mode matching configurations between two beams, or between a beam and an optical cavity.

To use the library, it must be copied into a known *folder* and the following line must be included at the beginning of the Mathematica notebook:

```
Needs["OpticsTools`","folder\opticstools2.m"].
```

Any calculation using the toolkit starts by defining the optical system. This is done by defining a Mathematica list of the optical elements, in order of appearance. The possible elements are listed in table B:

For the moment, the `y` coordinate is ignored, so the element position is only determined by `x`. The coordinate of each element is given as an absolute distance from the origin, which is defined to be the position of the input beam. A positive radius of curvature is for a convex surface in the direction of increasing x. An example system is the following:

```
syst = {Lens[d1,0,f],PlaneSurface[d1+d2,0,1,1.55],
        SphericalSurface[d1+ d2+6.35,0,150,1.55,1]};
```

Next, the input beam must be defined. The beam is given in terms of its complex q paramter, as $q = z_0 + iz_R$, being z_0 the position of the waist and z_R the Rayleigh range. The function

```
qparam0[z0,W0,λ]
```

can be used to obtain this parameter in terms of the waist position `z0`, the waist diameter `W0` and the wavelength λ. Typically, to obtain this parameter the best option is to measure its diameter with a CCD camera at different positions along the optical axis and fit the gaussian beam propagation function (Equation A.0.20).

Element	**Arguments**
`Lens[x,y,f]`	(x,y): position, f: focal length
`PlaneSurface[x,y,n1,n2]`	(n1,n2): initial and final refractive indices
`SphericalSurface[x,y,R,n1,n2]`	R: radius of curvature
`FreeSpace[x,y,d]`	d: propagation distance in free space

To define the mode of an optical resonator we use the function

$$q_{res} \texttt{ = ResonatorMode[R1, R2, L]}$$

where R1 and R2 are the radii of curvature of the two mirrors and L is the length of the resonator. For a confocal cavity, the function

```
q = ConfocalResonatorMode[L]
```

is better suited.

To propagate the beam through the optical system, one must use the function

$$q_{out} \texttt{ = PropagateBeam[syst,q]}$$

which returns the output beam parameter q_{out}. Here, `syst` is the optical system and `q` the input beam parameter.

The package allows to match two beams by adjusting any free system parameter, such as position, focal length of a lens, etc. For example, assume we want to match the mode q_{out} propagated through the optical system to the mode of an optical resonator q_{res}. The function

$$\texttt{equs=BeamMatchingEquations[}q_{out}\texttt{,}q_{res}\texttt{]}$$

returns the algebraic equations matching the two modes. It is then enough to use any Mathematica algebraic equation solver to obtain the solution. In this example, we solve for the distances $d1$ and $d2$ between the input beam, the lens and the cavity,

```
sol=FindRoot[equs,{{d1,350},{d2,150}}]
```

To visualize the solution the function $\texttt{PlotSystem[syst,}q_{in}\texttt{,}\lambda\texttt{,x}_i\texttt{,x}_f\texttt{]}$ is used, where $\texttt{x}_i$ and $\texttt{x}_f$ are the initial and final positions to perform the plot. Combining two of these plots, one for the input beam and one for the cavity mode, produces a plot such as the one in Figure 3.14.

A list of available functions with their descriptions is given below.

`ComputeQ[M,q]` computes the new q parameter given the ABCD matrix as first argument and the old q parameter as the second

`Waist[q,lambda,z]` computes the waist of gaussian beam defined by the q parameter as first argument, wavelength as second and position along longitudinal axis as third

`Lens[x,y,f]` defines a lens at position x,y of focal length f

`PlaneSurface[x,y,n1,n2]` defines a plane surface interface between two materials of refraction indices n1 and n2 in this order, at position x,y

`SphericalSurface[x,y,R,n1,n1]` defines a spherical surface interface of radius of curvature R between two materials of refraction indices n1 and n2 in this order. R ¿ 0 for concave from the right

`FreeSpace[x,y,d]` defines a free space propagation of distance d at position (x,y).

`PlotSystem[syst,q0,lambda,z1,z2]` plots the system given by syst, a list of optical elements, for an input beam parameter q0 from position z1 to z2. lambda is the wavelength in the same units as q0.

`PlotSystem2[syst,q0,lambda,z1,z2]` plots the system given by syst, a list of optical elements in logaritmic scale in y axis

`ResonatorMode[R1,R2,L]` gives the q parameter at the front mirror of an optical resonator of length L and mirrors of radii of curvature R1 and R2. For a confocal resonator use ConfocalResonatorMode

`CavityModeWaist[R1,R2,L,lambda]` gives the waist diameter of the mode of a cavity with mirrors of radii R1 and R2 separated by a distance L.

`ConfocalResonatorMode[R]` gives the q parameter at the front mirror of a confocal optical resonator of length R and mirrors of radii of curvature R.

`PropagateBeam[syst,qini]` gives the final q parameter of a beam qini propagated through the system syst

`PropagateABCDMatrix[syst]` gives the total M matrix of a system syst

`BeamMatchingEquations[q1,q2]` writes down algebraic equations for matching beams q1 and q2

`Radius[z,z0]` gives the radius of curvature of a beam at position z with waist position z0.

`WaistZ[z,z0,W0]` gives the beam diameter at a position z of a gaussian beam with waist W0 and waist position z0

`W0[zR,lambda]` gives the waist of a beam given its rayleigh range and its wavelength

`WaistQ[q,lambda]` gives the waist of a beam given its q parameter and the wavelength

`FiberMode[lambda,NA]` gives de q parameter of a fiber with NA numerical aperture for wavelength lambda

Qparam0[w0,z0,lambda] gives the initial q parameter given the waist w0, position of the waist z0 and wavelength lambda

C. Sellmeier and thermo-optic dispersion equations for KTP

The Sellmeier equations we used to calculate the refractive indices of KTP (at a temperature of 25°) were taken from Kato et al. [50]:

$$\begin{aligned} n_x^2 &= 3.29100 + \frac{0.04140}{\lambda^2 - 0.03978} + \frac{9.35522}{\lambda^2 - 31.45571} \\ n_y^2 &= 3.45018 + \frac{0.04341}{\lambda^2 - 0.04597} + \frac{16.98825}{\lambda^2 - 39.43799} \\ n_z^2 &= 4.59423 + \frac{0.06206}{\lambda^2 - 0.04763} + \frac{110.80672}{\lambda^2 - 86.12171} \end{aligned} \tag{C.0.1}$$

To obtain the refractive indices at a different temperature we use the thermo-optic coefficients extracted from the same reference:

$$\frac{dn_x}{dT} = \left(\frac{0.1717}{\lambda^3} - \frac{0.1717}{\lambda^2} + \frac{0.8416}{\lambda} + 0.1627\right) \times 10^{-5}(^\circ C)(0.43 < \lambda < 1.58) \tag{C.0.2}$$

$$\frac{dn_y}{dT} = \left(\frac{0.1997}{\lambda^3} - \frac{0.4063}{\lambda^2} + \frac{0.5154}{\lambda} + 0.5154\right) \times 10^{-5}(^\circ C)(0.43 < \lambda < 1.58)$$

$$\frac{dn_z}{dT} = \left(\frac{0.9221}{\lambda^3} - \frac{2.9220}{\lambda^2} + \frac{3.6677}{\lambda} - 0.1897\right) \times 10^{-5}(^\circ C)(0.53 < \lambda < 1.57) \tag{C.0.3}$$

The wavelength must be given in μm, and the temperature in $^\circ C$. The refractive index at a given temperature is obtained as

$$n_i(T, \lambda) = n_i(\lambda) + \frac{dn_i}{dT}(T - 25^\circ C) \tag{C.0.4}$$

Bibliography

[1] Roy J. Glauber. The quantum theory of optical coherence. *Phys. Rev.*, 130(6):2529–, June 1963.

[2] L. Mandel and E. Wolf. Coherence properties of optical fields. *Reviews of Modern Physics*, 37(2):231–287, 1965.

[3] J.R. Klauder and E.C.G. Sudarshan. *Fundamentals of quantum optics*. Benjamin New York, 1968.

[4] H. J. Kimble, M. Dagenais, and L. Mandel. Photon antibunching in resonance fluorescence. *Phys. Rev. Lett.*, 39(11):691–, September 1977.

[5] D. J. Wineland, R. E. Drullinger, and F. L. Walls. Radiation-pressure cooling of bound resonant absorbers. *Phys. Rev. Lett.*, 40(25):1639–, June 1978.

[6] W. Neuhauser, M. Hohenstatt, P. Toschek, and H. Dehmelt. Optical-sideband cooling of visible atom cloud confined in parabolic well. *Phys. Rev. Lett.*, 41(4):233–236, Jul 1978.

[7] Alain Aspect, Jean Dalibard, and Gérard Roger. Experimental test of bell's inequalities using time- varying analyzers. *Phys. Rev. Lett.*, 49(25):1804–1807, Dec 1982.

[8] P. Grangier, G. Roger, and A. Aspect. Experimental evidence for a photon anticorrelation effect on a beam splitter: a new light on single-photon interferences. *EPL (Europhysics Letters)*, 1:173–179, 1986.

[9] DN Klyshko. Coherent photon decay in a nonlinear medium. *Sov. Phys. JETP Lett*, 6:23, 1967.

[10] S. E. Harris, M. K. Oshman, and R. L. Byer. Observation of tunable optical parametric fluorescence. *Phys. Rev. Lett.*, 18(18):732–734, May 1967.

[11] David C. Burnham and Donald L. Weinberg. Observation of simultaneity in parametric production of optical photon pairs. *Phys. Rev. Lett.*, 25(2):84–87, Jul 1970.

[12] C. K. Hong and L. Mandel. Experimental realization of a localized one-photon state. *Phys. Rev. Lett.*, 56(1):58–60, Jan 1986.

[13] C. K. Hong, Z. Y. Ou, and L. Mandel. Measurement of subpicosecond time intervals between two photons by interference. *Phys. Rev. Lett.*, 59(18):2044–2046, Nov 1987.

[14] Y. H. Shih and C. O. Alley. New type of einstein-podolsky-rosen-bohm experiment using pairs of light quanta produced by optical parametric down conversion. *Phys. Rev. Lett.*, 61(26):2921–2924, Dec 1988.

[15] Z. Y. Ou and L. Mandel. Violation of bell's inequality and classical probability in a two-photon correlation experiment. *Phys. Rev. Lett.*, 61(1):50–, July 1988.

[16] Y. H. Shih, A. V. Sergienko, Morton H. Rubin, T. E. Kiess, and C. O. Alley.

Two-photon entanglement in type-ii parametric down-conversion. *Phys. Rev. A*, 50(1):23–28, Jul 1994.

[17] P.G. Kwiat, K. Mattle, H. Weinfurter, A. Zeilinger, A.V. Sergienko, and Y. Shih. New high-intensity source of polarization-entangled photon pairs. *Physical Review Letters*, 75(24):4337–4341, 1995.

[18] Warren Nagourney, Jon Sandberg, and Hans Dehmelt. Shelved optical electron amplifier: Observation of quantum jumps. *Phys. Rev. Lett.*, 56(26):2797–, June 1986.

[19] Th. Sauter, W. Neuhauser, R. Blatt, and P. E. Toschek. Observation of quantum jumps. *Phys. Rev. Lett.*, 57(14):1696–, October 1986.

[20] J. C. Bergquist, Randall G. Hulet, Wayne M. Itano, and D. J. Wineland. Observation of quantum jumps in a single atom. *Phys. Rev. Lett.*, 57(14):1699–1702, Oct 1986.

[21] Frank Diedrich and Herbert Walther. Nonclassical radiation of a single stored ion. *Phys. Rev. Lett.*, 58(3):203–, January 1987.

[22] F. Diedrich, J. C. Bergquist, Wayne M. Itano, and D. J. Wineland. Laser cooling to the zero-point energy of motion. *Phys. Rev. Lett.*, 62(4):403–406, Jan 1989.

[23] D. Deutsch and R. Jozsa. Rapid solution of problems by quantum computation. *Proceedings: Mathematical and Physical Sciences*, pages 553–558, 1992.

[24] PW Shor. *Algorithms for quantum computation: discrete logarithms and factoring*. ANNUAL SYMPOSIUM ON FOUNDATIONS OF COMPUTER SCIENCE. I E E E, COMPUTER SOC PRESS, 10662 LOS VAQUEROS CIRCLE, LOS ALAMITOS, CA 90720, 1994. 35th Annual Symposium on Foundations of Computer Science, SANTA FE, NM, NOV 20-22, 1994.

[25] RL Rivest, A. Shamir, and L. Adleman. A method for obtaining digital signatures and public-key cryptosystems. *Communications of the ACM*, 21(2):126, 1978.

[26] Lieven M. K. Vandersypen, Matthias Steffen, Gregory Breyta, Costantino S. Yannoni, Mark H. Sherwood, and Isaac L. Chuang. Experimental realization of shor's quantum factoring algorithm using nuclear magnetic resonance. *Nature*, 414(6866):883–887, December 2001.

[27] Isaac L. Chuang, Lieven M. K. Vandersypen, Xinlan Zhou, Debbie W. Leung, and Seth Lloyd. Experimental realization of a quantum algorithm. *Nature*, 393(6681):143–146, May 1998.

[28] Stephan Gulde, Mark Riebe, Gavin P. T. Lancaster, Christoph Becher, Jurgen Eschner, Hartmut Haffner, Ferdinand Schmidt-Kaler, Isaac L. Chuang, and Rainer Blatt. Implementation of the deutsch-jozsa algorithm on an ion-trap quantum computer. *Nature*, 421(6918):48–50, January 2003.

[29] David P. DiVincenzo. The physical implementation of quantum computation. *Fortschritte der Physik*, 48(9-11):771–783, 2000.

[30] Ferdinand Schmidt-Kaler, Hartmut Haffner, Mark Riebe, Stephan Gulde, Gavin P. T. Lancaster, Thomas Deuschle, Christoph Becher, Christian F. Roos, Jurgen Eschner, and Rainer Blatt. Realization of the cirac-zoller controlled-not quantum gate. *Nature*, 422(6930):408–411, March 2003.

[31] H. Haffner, W. Hansel, C. F. Roos, J. Benhelm, D. Chek-al kar, M. Chwalla, T. Korber, U. D. Rapol, M. Riebe, P. O. Schmidt, C. Becher, O. Guhne, W. Dur, and R. Blatt. Scalable multiparticle entanglement of trapped ions. *Nature*, 438(7068):643–646, December 2005.

[32] D. L. Moehring, P. Maunz, S. Olmschenk, K. C. Younge, D. N. Matsukevich, L.-M. Duan, and C. Monroe. Entanglement of single-atom quantum bits at a distance. *Nature*, 449(7158):68–71, September 2007.

[33] Meng Khoon Tey, Zilong Chen, Syed Abdullah Aljunid, Brenda Chng, Florian Huber, Gleb Maslennikov, and Christian Kurtsiefer. Strong interaction between light and a single trapped atom without the need for a cavity. *Nat Phys*, 4(12):924–927, December 2008.

[34] M. Sondermann, R. Maiwald, H. Konermann, N. Lindlein, U. Peschel, and G. Leuchs. Design of a mode converter for efficient light-atom coupling in free space. *Applied Physics B: Lasers and Optics*, 89(4):489–492, December 2007.

[35] M. Stobińska, G. Alber, and G. Leuchs. Perfect excitation of a matter qubit by a single photon in free space. *EPL (Europhysics Letters)*, 86:14007, 2009.

[36] J. I. Cirac, P. Zoller, H. J. Kimble, and H. Mabuchi. Quantum state transfer and entanglement distribution among distant nodes in a quantum network. *Phys. Rev. Lett.*, 78(16):3221–, April 1997.

[37] Christoph Simon and William T. M. Irvine. Robust long-distance entanglement and a loophole-free bell test with ions and photons. *Phys. Rev. Lett.*, 91(11):110405, Sep 2003.

[38] S. Lloyd, M. S. Shahriar, J. H. Shapiro, and P. R. Hemmer. Long distance, unconditional teleportation of atomic states via complete bell state measurements. *Phys. Rev. Lett.*, 87(16):167903, Sep 2001.

[39] Marc Almendros. *Towards Long-Distance Quantum Communication*. PhD thesis, ICFO - The Institute of Photonic Sciences, 2010.

[40] Albrecht Haase, Nicolas Piro, Jrgen Eschner, and Morgan W. Mitchell. Tunable narrowband entangled photon pair source for resonant single-photon single-atom interaction. *Opt. Lett.*, 34(1):55–57, January 2009.

[41] Nicolas Piro, Albrecht Haase, Morgan W. Mitchell, and Jurgen Eschner. An entangled photon source for resonant single-photon–single-atom interaction. *Journal of Physics B: Atomic, Molecular and Optical Physics*, 42(11):114002–, 2009.

[42] C. Schuck, F. Rohde, N. Piro, M. Almendros, J. Huwer, M. W. Mitchell, M. Hennrich, A. Haase, F. Dubin, and J. Eschner. Resonant interaction of a single atom with single photons from a down-conversion source. *Phys. Rev. A*, 81(1):011802, Jan 2010.

[43] Nicolas Piro, Felix Rohde, Carsten Schuck, Jan Huver, Marc Almendros, Joyee Ghosh, Albrecht Haase, Francois Dubin, Markus Hennrich, and Jürgen Eschner. Heralded single photon absorption by a single atom. 2010. To be submitted.

[44] M. Almendros, J. Huwer, N. Piro, F. Rohde, C. Schuck, M. Hennrich, F. Dubin, and J. Eschner. Bandwidth-tunable single-photon source in an ion-trap

quantum network. *Phys. Rev. Lett.*, 103(21):213601, Nov 2009.

[45] F. Rohde, J. Huwer, N. Piro, M. Almendros, C. Schuck, F. Dubin, and J. Eschner. Polarization-correlated photon pairs from a single ion. 2009.

[46] Felix Rohde. *Remote ion traps for quantum networking: Two-photon interference and correlations*. PhD thesis, ICFO - The Institute of Photonic Sciences, 2009.

[47] Robert W. Boyd. *Nonlinear Optics*. Academic Press, 2003.

[48] I. Abram and E. Cohen. Quantum theory for light propagation in a nonlinear effective medium. *Phys. Rev. A*, 44(1):500–, July 1991.

[49] Mark Hillery and Leonard D. Mlodinow. Quantization of electrodynamics in nonlinear dielectric media. *Phys. Rev. A*, 30(4):1860–, October 1984.

[50] Kiyoshi Kato and Eiko Takaoka. Sellmeier and thermo-optic dispersion formulas for ktp. *Appl. Opt.*, 41(24):5040–5044, August 2002.

[51] F. Rohde, M. Almendros, C. Schuck, J. Huwer, M. Hennrich, and J. Eschner. A diode laser stabilization scheme for 40ca single ion spectroscopy. *Submitted to JOSA B*, 2010.

[52] Tso Yee Fan, C. E. Huang, B. Q. Hu, R. C. Eckardt, Y. X. Fan, Robert L. Byer, and R. S. Feigelson. Second harmonic generation and accurate index of refraction measurements in flux-grown ktiopo4. *Appl. Opt.*, 26(12):2390–2394, 1987.

[53] Christian Kurtsiefer, Markus Oberparleiter, and Harald Weinfurter. High-efficiency entangled photon pair collection in type-ii parametric fluorescence. *Phys. Rev. A*, 64(2):023802, Jul 2001.

[54] Fabio Antonio Bovino, Pietro Varisco, Anna Maria Colla, Giuseppe Castagnoli, Giovanni Di Giuseppe, and Alexander V. Sergienko. Effective fiber-coupling of entangled photons for quantum communication. *Optics Communications*, 227(4-6):343 – 348, 2003.

[55] Daniel Ljunggren and Maria Tengner. Optimal focusing for maximal collection of entangled narrow-band photon pairs into single-mode fibers. *Phys. Rev. A*, 72(6):062301, Dec 2005.

[56] Alessandro Fedrizzi, Thomas Herbst, Andreas Poppe, Thomas Jennewein, and Anton Zeilinger. A wavelength-tunable fiber-coupled source of narrow-band entangled photons. *Opt. Express*, 15(23):15377–15386, November 2007.

[57] Morgan W. Mitchell. Parametric down-conversion from a wave-equations approach: geometry and absolute brightness, Jul 2008.

[58] G. D. Boyd and D. A. Kleinman. Parametric interaction of focused gaussian light beams. *J. Appl. Phys.*, 39(8):3597–3639, July 1968.

[59] Carol E. Tanner and Carl Wieman. Precision measurement of the hyperfine structure of the cs133 6p3/2 state. *Phys. Rev. A*, 38(3):1616–, August 1988.

[60] S. Gulde. *Experimental realization of quantum gates and the deutsch-josza algorithm with trapped 40Ca+ ions*. PhD thesis, Universität Innsbruck, 2003.

[61] Carsten Schuck. *Interfacing single ions and single photons for quantum networks*. PhD thesis, ICFO, The Institute Of Photonics Sciences, 2010.

[62] Luc Devroye. *Non-Uniform Random Variate Generation*. New York: Springer-Verlag, 1986.

[63] D.K.T. Chu, J.D. Bierlein, and R.G. Hunsperger. Piezoelectric and acoustic properties of potassium titanyl phosphate (ktp) and its isomorphs. *Ultrasonics, Ferroelectrics and Frequency Control, IEEE Transactions on*, 39(6):683–687, 1992.

[64] Daniel F. V. James, Paul G. Kwiat, William J. Munro, and Andrew G. White. Measurement of qubits. *Phys. Rev. A*, 64(5):052312–, October 2001.

[65] R. Gerritsma, G. Kirchmair, F. Zhringer, J. Benhelm, R. Blatt, and F. Roos, C. Precision measurement of the branching fractions of the $4p^2p_{3/2}$ decay of caii. *Eur. Phys. J. D*, 50(1):13–19, November 2008.

[66] A. Kreuter, C. Becher, G. P. T. Lancaster, A. B. Mundt, C. Russo, H. Häffner, C. Roos, W. Hänsel, F. Schmidt-Kaler, R. Blatt, and M. S. Safronova. Experimental and theoretical study of the $3dd2$ –level lifetimes of $ca + 40$. *Phys. Rev. A*, 71(3):032504, Mar 2005.

[67] A. E. Siegman. *Lasers / Anthony E. Siegman*. University Science Books, Mill Valley, Calif. :, 1986.

[68] J. Eschner, Ch. Raab, F. Schmidt-Kaler, and R. Blatt. Light interference from single atoms and their mirror images. *Nature*, 413(6855):495–498, October 2001.

[69] Markus Oberparleiter and Harald Weinfurter. Cavity-enhanced generation of polarization-entangled photon pairs. *Optics Communications*, 183(1-4):133 – 137, 2000.

[70] Z. Y. Ou and Y. J. Lu. Cavity enhanced spontaneous parametric down-conversion for the prolongation of correlation time between conjugate photons. *Phys. Rev. Lett.*, 83(13):2556–2559, Sep 1999.

[71] Christopher E. Kuklewicz, Franco N. C. Wong, and Jeffrey H. Shapiro. Time-bin-modulated biphotons from cavity-enhanced down-conversion. *Phys. Rev. Lett.*, 97(22):223601–4, December 2006.

[72] Friedrich Konig, Elliott J. Mason, Franco N. C. Wong, and Marius A. Albota. Efficient and spectrally bright source of polarization-entangled photons. *Phys. Rev. A*, 71(3):033805–7, March 2005.

[73] F. Wolfgramm, X. Xing, A. Cerè, A. Predojević, A. M. Steinberg, and M. W. Mitchell. Bright filter-free source of indistinguishable photon pairs. *Opt. Express*, 16(22):18145–18151, 2008.

[74] Matthias Scholz, Lars Koch, and Oliver Benson. Statistics of narrow-band single photons for quantum memories generated by ultrabright cavity-enhanced parametric down-conversion. *Phys. Rev. Lett.*, 102(6):063603, Feb 2009.

[75] Bahaa E A Saleh and Malvin Carl Teich. *Fundamentals of photonics*. Wiley, New York, NY, 1991.